# Dissociation dynamics and ionization processes in slow ion-molecule collisions

A dissertation submitted in partial fulfillment of the requirements for the degree of

DOCTOR OF PHILOSOPHY

By

**Sumit Srivastav**

**Reg. ID- 20153415**


Department Of Physics

INDIAN INSTITUTE OF SCIENCE EDUCATION AND RESEARCH PUNE

March, 2023

*In Memory of My Father*

# Declaration

I, **Sumit Srivastav**, declare that this written submission entitled **'Dissociation dynamics and ionization processes in slow ion-molecule collisions'** represents my idea in my own words and where others' ideas have been included; I have adequately cited and referenced the original sources. I also declare that I have adhered to all principles of academic honesty and integrity and have not misrepresented or fabricated or falsified any idea/data/fact/source in my submission. I understand that violation of the above will be cause for disciplinary action by the Institute and can also evoke penal action from the sources which have thus not been properly cited or from whom proper permission has not been taken when needed. The work reported in this thesis is the original work done by me under the guidance of Prof. Bhas Bapat.

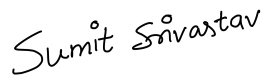

Sumit Srivastav

Reg. Id: 20153415

# Certificate

I certify that the thesis entitled **'Dissociation dynamics and ionization processes in slow ion-molecule collisions'** presented by **Mr Sumit Srivastav** represents his original work which was carried out by him at IISER, Pune under my guidance. The work presented here or any part of it has not been included in any other thesis submitted previously for the award of any degree or diploma from any other University or institutions. I further certify that the above statements made by him in regard to his thesis are correct to the best of my knowledge.

Prof. Bhas Bapat

# Contents

# Acknowledgements

First and foremost, I would like to express my gratitude to my thesis supervisor, Prof. Bhas Bapat, without whom I would not be close to what I am today. Working with him in the lab is a very different level of experience. I learnt every small technique in lab from him. I enjoyed working with him, and would love the opportunity to work with him in the future. Apart from the research work, he has supported me in all possible ways throughout my Ph.D. Things were not the same after the tough time of covid pandemic. I am very grateful to him for showing immense patience with me.

I thank my RAC members, Dr. Sourabh Dube and Dr. Rejish Nath, for their continuous evaluation of my research work.

I am thankful to IISER Pune for the fellowship during my Ph.D. tenure. I thank the Science and Engineering Research Board (India) for generous funding via grant No. 30116294, in 2017, which enabled the setting up of the EBIS/A ion source used for this work. A special thanks to the Physics department, IISER Pune, for partial support of the funds to attend conferences and schools during my Ph.D.

I thank Nilesh Dumbre, Sudhir, Santosh, and Prashant for their technical support at the IISER Pune laboratory. I am thankful to Prabhakar, Dhanashree from the Physics office, and Tushar and Sayali from the academic office for their help during official work at IISER. I must acknowledge all housekeeping staff and gardeners to keep our environment neat and clean. I thank the hostel manager Mr. Ramlal Choudhary.

Friends make life enjoyable and incredible in the hardest times, the best moments, and everything in between. I am thankful to Anweshi, Bani, Imran, Ajith, Gautam, Suddhu, Arnab, Projjwal, Arijeet, Naveen, Abhishek, Bhumika and Alpana for their company and for making this stay at IISER memorable. I thank Deepak, the only

lab member available when I joined this group. I will always cherish the moments spent with him. We have developed a good friendship bonding over time. I thank Ankita, Chinmayee and Yashwant for having nice weekend trips and many more memorable times spent together. I am very grateful to Mayur and Kumar Saurabh. We have developed a good friendship in the last few years and hope it to last forever. It would be incomplete without acknowledging Shatruhan. I was lucky to have him as a senior in the Physics department. I will always remember our evening walks and tea. I want to thank Shipra for her support and for being by my side in the ups and downs.

I want to thank the present lab members Vishnu and Akash. They have been very helpful and hardworking in setting up the post collision charge state analyzer in the lab.

I am grateful to Dr. Seema Sharma. She constantly kept taking updates on my work progress and motivated me throughout my Ph.D. A special thanks for making me your experimental rat whenever you cook something different. Your Rasmalai and Gajar halwa recipes are my all time favourite.

In every stage of life, the family's role is most important. Any adjective is too small to express gratitude for my family members. I can not describe the sacrifice my parents made to educate us. A special thanks to my elder brother Amit (bhaiya). His motivations keep me alive to fight every hurdle in life.

# Abstract

When an isolated molecule interacts with an external perturbation created by energetic charged ions, excitation of the molecule may occur. If the perturbation strength is enough, removal of a number of electrons from the molecule via different ionization processes can occur, resulting in multiple ionization of the molecule. The so-formed multiply ionized molecular ion is generally unstable and subsequently dissociates into its fragment ions. These fragment ions move apart in a continuum with finite kinetic energies and constitute a dynamic many-body coulombically interacting system.

The perturbation strength of the projectile ion interacting with the target is generally characterized by the projectile charge state ($q$) and its velocity ($v$), both are in atomic units (a.u.). For $v < 1$ a.u. and $v > 1$ a.u., the impact of projectile is considered slow and fast, respectively. In the ion-molecule collision, for a given charge state and velocity of the projectile ion, the energy transferred to the molecule depends on the collision impact parameter ($b$). Experimentally, there is no control over the impact parameter of collision, and therefore it limits the information on energy transfer that can be obtained in an experiment. The energy transferred to a molecule under charged particle impact is shared among its electronic and nuclear degrees of freedom, resulting in the excitation of the target molecule. Subsequently, the fate of so-formed excited molecule is decided by the properties of its excited states.

This work investigates the multiply ionized molecular ions which are formed under charged particle impact, and eventually dissociate into their fragment ions. The main focus of this work is to address the question such as how the projectile properties affect the kinematics of dissociating multiply ionized molecular ions created under the impact of slow ($v < 1$ a.u.) projectile ions. To address this, systematic

experiments are performed with projectile ions of various charge states, and with the simplest projectile, the proton ($H^+$), of different velocities. The second part of this work addresses how the underlying ionization process, such as the direct and capture processes influence the dissociation dynamics of formed molecular ions.

Investigations are carried out using ions beams from an electron beam ion source (EBIS) and fragments are analyzed using an ion-momentum spectrometer (IMS). A post collision charge state analyzer is especially designed and implemented. Coupled with the existing IMS, it is used to separate direct and capture ionization processes.

Our investigation shows that in slow impact regime, the projectile charge state, $q$, influences the probability of accessing different excited electronic states of the transient molecular ion. We also demonstrate that despite being a structureless projectile, a slight variation in the impact velocity of the proton affects the kinematics in three-body dissociation of $CO_2^{3+}$ molecular ion in slow impact regime. With the separation of ionization processes, we find that the different order of capture processes significantly influence the branching ratio of various formed fragment ions, while the KER distributions are not significantly affected.

**Keywords:** dissociation dynamics, molecular ion, momentum imaging, kinetic energy release, potential energy curve, charge-exchange process, cylindrical deflector analyzer

# List of publications

1. Post collision analyzer to study charge-exchange processes in ion-molecule collisions

   **Sumit Srivastav** and Bhas Bapat, Rev. Sci. Instrum. 93, 113306 (2022)

2. Electron-impact-like feature in triple fragmentation of $CO_2^{3+}$ under slow proton impact

   **Sumit Srivastav** and Bhas Bapat, Phys. Rev. A 105, 012801, (2022)

3. Fragmentation dynamics of $CO_2^{4+}$ : Contributions of different electronic states

   **Srivastav** *et al*, Phys. Rev. A 103, 032821, (2021)

4. Electron beam ion trap/source for ion-molecule collisions in the non-perturbative regime

   B Bapat, D Sharma and **S Srivastav**, J. Phys.: Conf. Ser.1412 152070 (2020)

# Conference contributions

1. The 32nd International Conference on Photonic, Electronic and Atomic Collisions (ViCPEAC 2021), July 20-23, 2021 (Online mode)

   P1. Fragmentation dynamics of $CO_2^{4+}$ : Contributions of different electronic states

2. 8th Topical Conference (TC-2020) on Atomic and Molecular Collisions for Plasma Applications, March 3-5, 2020, IIT Roorkee, India

   P1. Electron Beam Ion Trap/Source for ion–molecule collisions in the non-perturbative regime

   P2. Dissociation dynamics of multiply charged $CO_2$ under impact of slow and highly charged ions

3. 22nd National Conference on Atomic and Molecular Physics, 25-28 March 2019, IIT Kanpur, India

   P1. An Electrostatic Post-Collision Charge State Analyzer

# List of Figures

# List of Tables

# Chapter 1

# Introduction

Atomic and molecular physics forms the fundamental knowledge base for our understanding in disciplines such as atmospheric, environmental, chemical, biomedical and astrophysical sciences. The understanding of the stationary structure of atoms and molecules have been evolving over many decades. By the end of 19th century, atom was considered as tiny indivisible particle and the building block of matter. The discovery of electron in 1897 by English physicist J.J. Thomson broke the very old idea of the atom as a structureless particle and showed that in fact the atom has a complex structure [1]. Later in 1909, the value of electric charge on the electron was found to be quantized in the famous experiment of Robert Andrews Millikan [2]. The discovery of negatively charged electron had raised theoretical problems for physicists because atoms as a whole are electrically neutral. In 1911, Rutherford with his famous gold foil experiment, the first scattering experiment to understand the structure of atom, demonstrated that the atom has a tiny, massive and positively charged nucleus and the positively charged proton was discovered in 1919 [3]. In 1932, James Chadwick discovered the existence of the neutral particle named neutron in the nucleus [4]. In this manner, the idea that atom is indivisible and structureless started to fade with precise experimental results.

In 1913, Niels Bohr proposed his quantized orbit model of the atom to explain how electrons can have stable orbits around the nucleus [5]. Before Bohr's model, the motion of the electrons in the Rutherford model had to be regarded as unstable because, according to classical mechanics and electromagnetic theory, any charged particle moving on a curved path emits electromagnetic radiation; thus, the electrons

would lose energy and spiral into the nucleus. Bohr atomic model was based on the ideas of Planck and Einstein used in explaining the black-body radiation and photoelectric effect [6, 7]. In spite of the great success with a revolutionary idea of stable orbit of electron, Bohr model had major drawbacks which includes its inability to explain the properties of atoms having more than one electrons and transitions between levels. However, the concept that light and matter have both wave and particle characteristics at the atomic and subatomic levels, had brought revolutionary changes in understanding the whole picture of atom [8, 9, 10]. Within a span of few years, with the help of laws of quantum mechanics scientists developed a consistent theory of the atom that explained its fundamental structure and its emerged interactions. The Schrödinger equation, essentially a mathematical wave equation, established quantum mechanics in a widely more applicable form [8]. The modern view of atoms or molecules is a quantum mechanical one in which the discrete orbit idea is replaced by a probabilistic picture. Schrödinger's wave equation gives the same energies as Bohr's original formula but with a much more precise description of an electron in an atom. However, Schrödinger equation can be solved analytically for hydrogen atom only. In 1929, a Norwegian physicist Egil Hylleraas applied the Schrödinger equation to the helium atom with its two electrons [11, 12]. He obtained only an approximate solution using a modified coordinate system, but his energy calculation was quite accurate. With Hylleraas's explanation of the two-electron atom, it was realized that the Schrödinger equation could be a powerful mathematical tool for describing nature on the atomic level, even if exact solutions could not be obtained. In a molecule, which is formed by the combination of two or more than two atoms, there are many more (compared the atom) interactions such as electron-electron, electron-nucleus and nucleus-nucleus exist and solving the Schrödinger equation is more challenging. Various approximations adopted to incorporate all possible interactions to solve Schrödinger wave equation. Some of these approximations are discussed in further section 1.1.

The static structure and properties of atoms and molecules, such as binding energy, electronic energy levels, dipole moment etc, have been studied over many decades and the rich information about these are available in the literature [13]. However, the study of evolution of the atoms or molecules under the influence of ex-

ternal perturbation is even more challenging both theoretically and experimentally. The constituents of an atom or molecule under external perturbation interact with the source of perturbation which may change the static properties of systems. In the case of ionizing perturbation, the loss of electrons results in change in the number of particles describing the system. The electron-electron and electron-nucleus interactions of perturbed systems change significantly from static system. Further, the presence of different degrees of freedom such as rotation and vibration makes a molecule a complex system to study under external perturbation, compared to an atomic system. These degrees of freedom need to be taken into account to understand molecular dynamical properties.

In collision physics, a molecule can be perturbed by interaction with different projectiles viz photon impact or charge particle such as electron, proton or highly charge ion. The behaviour of a molecule under external perturbation is discussed in section 1.2. The perturbation created by charged particle on molecular target, i.e. ion-molecule collision, plays a vital role in many different fields such as, plasma physics, astrophysics, radiation therapy, and chemical physics. In ion-molecule collisions, the outcome of collisions depend on the properties of projectile ion and the structure of molecule. Dissociation dynamics of a molecule are briefly presented in section 1.3.

This thesis attempts to understand ion-molecule collisions including the dissociation dynamics of multiply ionized molecular ion created by collisions, and understanding the ionization processes responsible for multiple ionization of a molecular target. Dissociation dynamics is a long studied topic of research. A brief about earlier studies is presented in section 1.4 along with an outline of this thesis work.

## 1.1 The molecule

When atoms approach one another closely, the electron clouds of atoms interact with each other and with the nuclei. If this interaction is such that the total energy of the system is lowered, then the atoms bond together to form a molecule. In this section, we will discuss the quantum mechanical description of a molecule. The description of molecular structure is considerably more complicated than that of isolated atom,

but the problem is greatly simplified with the help of a few simple and appropriate approximations. The complete information of molecule can be obtained by knowing the solution of Schrödinger wave equation which is given by

$$\hat{H}\Psi = E\Psi \tag{1.1}$$

where $\hat{H}$ is Hamiltonian operator, $E$ is the total energy of system and $\Psi$ represents the wave function of molecule. The molecular Hamiltonian can be written as,

$$\hat{H} = \underbrace{-\frac{\hbar^2}{2}\sum_{\alpha}\frac{1}{m_\alpha}\nabla_\alpha^2}_{\hat{T}_N} \underbrace{-\frac{\hbar^2}{2m_e}\sum_{i}\nabla_i^2}_{\hat{T}_e} + \underbrace{\sum_{\alpha}\sum_{\beta>\alpha}\frac{Z_\alpha Z_\beta e^2}{r_{\alpha\beta}} - \sum_{\alpha}\sum_{i}\frac{Z_\alpha e^2}{r_{i\alpha}} + \sum_{j}\sum_{i>j}\frac{e^2}{r_{ij}}}_{\hat{V}} \tag{1.2}$$

where $\alpha$, $\beta$ refer to nuclei and $i$, $j$ refer to electrons. $m_\alpha$ and $m_e$ represent mass of nucleus and electron respectively. $r$ denotes distance, $Z$ is atomic number and $e$ is electronic charge. $\hat{T}_N$ and $\hat{T}_e$ represent kinetic energy operators of nuclei and electrons respectively and $\hat{V}$ denotes the potential energy operator of the system.

Schrödinger wave equation even for the simplest molecule $H_2^+$, consisting of three particles, can not be solved analytically. To overcome this difficulty, we adopt the Born-Oppenheimer approximation, which takes note of the great difference in masses of nuclei ($m_\alpha$) and electrons ($m_e$) [14]. Because they are much lighter, the electrons can respond almost instantaneously to displacement of the nuclei. Therefore, instead of trying to solve the Schrödinger equation for all the particles simultaneously, we regard the nuclei as fixed in position and solve the Schrödinger equation for the electrons in the static electric potential arising from the nuclei in that particular arrangement. The Born-Oppenheimer approximation enables us to write the total molecular wave function $\Psi$ as a product of electronic wave function, $\psi_e$ and nuclear wave function, $\psi_N$.

$$\Psi(\vec{R}, \vec{r}_1, \vec{r}_2, ....\vec{r}_p) = \psi_N(\vec{R})\ \psi_e(\vec{R}; \vec{r}_1, \vec{r}_2, ....\vec{r}_p) \tag{1.3}$$

where $\vec{R}$ is the internuclear coordinate and $\vec{r}_1, \vec{r}_2, ....\vec{r}_p$ represent the position vectors of $p$ electrons in the centre of mass frame of system. The notation $\psi_e(\vec{R}; \vec{r}_1, \vec{r}_2, ....\vec{r}_p)$ means that the wavefunction for the electron is a function of its position and depends

parametrically on the coordinates of the nuclei. $\psi_N(\vec{R})$ represents the wavefunction related to motion of nuclei.

### 1.1.1 Potential energy curve and surface

The time-independent Schrödinger wave equation for electrons assuming stationary nuclei can be written as,

$$(\hat{T}_e + \hat{V})\psi_e(\vec{R};\vec{r}_1,\vec{r}_2,....\vec{r}_p) = E_k(\vec{R})\psi_e(\vec{R};\vec{r}_1,\vec{r}_2,....\vec{r}_p) \tag{1.4}$$

The value of operators $\hat{T}_e$ and $\hat{V}$ are shown in Eqn. 1.2 under braces. The eigenvalue $E_k$ is the electronic potential energy contribution to the total energy of the molecule plus the potential energy of internuclear repulsion at the parametrically fixed nuclear locations. Solving Eqn. 1.4 is relatively easier task since electronic wavefunction and energy only has parametric dependence on the nuclear configuration. The solution of Eqn. 1.4 changes with the change in nuclear configuration and thereby yields the different values of $E_k$. The variation of this potential energy as a function of the nuclear degrees of freedom gives the potential energy curve (PEC) for diatomic molecules. In general, for a polyatomic molecule, additional degrees of freedom related to its geometry such as bond-angle and bond lengths exist and variation of potential energy of molecule with its geometrical parameters results in potential energy surface (PES).

The total energy of molecular system can be obtained by solving the nuclear Schrödinger equation,

$$\hat{H}_N\psi_N = E\psi_N \tag{1.5}$$

where the Hamiltonian is, $\hat{H}_N = -\frac{\hbar^2}{2}\sum_\alpha \frac{1}{m_\alpha}\nabla_\alpha^2 + \hat{E}_k$. Here, $E$ is the total energy of molecule since Hamiltonian consists of both nuclear energy and electronic energy operators.

### 1.1.2 Molecular orbitals

Previously, we discussed the general approach to determine the energy of the molecular system. In this section, we will discuss briefly about the determination of the molecular wavefunction itself, particularly the electronic part of the wavefunction

($\psi_e$). Even under the Born-Oppenheimer approximation, there is only one molecular species for which Schrödinger equation can be solved exactly: the hydrogen molecular ion, $H_2^+$. Additionally, two major approximations have been devised to tackle this problem. The first was proposed by Walter Heitler and Fritz London in 1927 [15] and substantially developed by John Slater [16] and Linus Pauling [17] in the 1930s, is valence bond (VB) theory. The other, molecular orbital (MO) theory was introduced about the same time as VB theory in 1930 by Robert S. Mulliken [18, 19] and Friedrich Hund [20, 21]. Somewhat later, Lennard-Jones and Hückel applied MO theory to electronic structures of molecules [22, 23]. In the VB theory, electrons in a molecule are assumed to occupy atomic orbitals rather than the molecular orbitals. Whereas in MO theory, each electron is assumed to be in a molecular orbital and net wavefunction is a product of many one-electron wavefunctions. However, MO theory has undergone much more development than VB theory and gives a good insight and a quantitative description, so we will concentrate on it.

The electronic wave functions for molecular systems containing several electrons can be constructed from the linear combinations of atomic orbitals that have the same symmetry with respect to rotation about the internuclear axis. Since quite accurate atomic orbitals for many-electron atoms are available, it becomes an efficient approach to use them as a starting point for the description of many-electron molecules built from those atoms. This method is particularly known as 'linear combination of atomic orbitals' (LCAO). For better understanding, let us consider the simplest diatomic molecular system $H_2^+$ which is composed of two protons (labeled as $A$ and $B$) and one electron. When the two protons $A$ and $B$ are far apart, the electron must be attached to one of them. So, the spatial part of overall electronic wavefunction can be written as a superposition of the two atomic orbitals,

$$\psi_{\pm}(\vec{R};\vec{r}) = C[\psi_{1s}(A) \pm \psi_{1s}(B)] \tag{1.6}$$

where $C$ is normalization constant and $\psi_{1s}(r) = \pi^{-1/2}\exp(-r)$ is the normalised ground state wavefunction for atomic hydrogen (written in atomic units). Out of these two solutions, $\psi_+$ gives lower energy while $\psi_-$ gives higher energy and corresponding orbitals are called bonding molecular orbital and antibonding molecular orbital, respectively.

Like the atomic orbitals $s, p, d, ...$, molecular orbitals are named as $\sigma, \pi, \delta, ...$ depending on the modulus of the projection of the total angular momentum along the internuclear axis. For homonuclear diatomic molecules, there exists a centre of symmetry at the mid-point of nuclei $A$ and $B$ i.e. the Hamiltonian remains invariant under the inversion of the coordinates of the electrons with respect to this mid point. The molecular orbital wavefunction symmetric with respect to the plane passing through the centre of symmetry is called 'gerade' while the asymmetric molecular orbital wavefunctions are known as 'ungerade' orbitals, and they are denoted by '$g$' and '$u$' subscript respectively (for example: $\sigma_g, \sigma_u$). These molecular orbitals are filled according to the Pauli's exclusion principle to give the electronic configuration of the molecule [24]. For example, $N_2$ molecule has 14 electrons and its ground state electronic configuration can be written as,

$$\underbrace{(1\sigma_g)^2(1\sigma_u)^2}_{core}\ \underbrace{(2\sigma_g)^2(2\sigma_u)^2(1\pi_u)^4(3\sigma_g)^2}_{valence} \tag{1.7}$$

Analogous to the atomic notations, the electronic state of the molecular systems are represented as a term symbol,

$$^{2S+1}\Lambda^{+/-}_{g/u} \tag{1.8}$$

Here, $\Lambda$ is modulus of the projection of total electronic orbital angular momentum along the internuclear axis. For $\Lambda$=0,1,2,..., the term symbol is denoted by $\Sigma, \Pi, \Delta, ...$ etc. $S$ is the total electronic spin quantum number and $2S+1$ denotes the multiplicity. Symbols '$g$' and '$u$' have their usual meaning discussed earlier. For $\Sigma$-state, an additional symmetry property can be introduced by considering the plane containing the internuclear axis . The molecular wavefunction with symmetric reflection with respect to this plane is denoted as '+' and the asymmetric ones is represented as '$-$'. For example, the molecular term symbol for ground state $N_2$ (for which electronic configuration is shown in Eqn. 1.7) is denoted as $^1\Sigma^+_g$.

## 1.2 Molecule under charged particle perturbation

In the absence of any external perturbation, an isolated molecule is stable, and constituent electrons and nuclei move in the Coulombic mean-field of each other. A

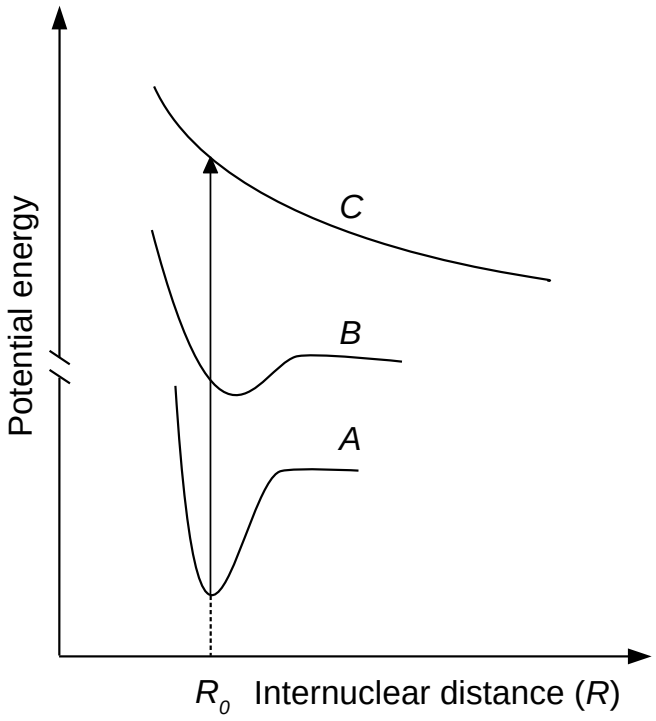


Figure 1.1: A typical potential energy curve diagram for a diatomic molecule AB. Curves $A, B$ and $C$ represent the stable, metastable and unstable states of the molecule, respectively. $R_0$ represents equilibrium internuclear separation. Vertical arrow shows Franck-Condon transition.

molecule intrinsically possesses different internal motions such as vibration, rotation even in its stable ground electronic state. Solving the electronic Schrödinger equation for a range of internuclear separations gives potential energy curves/surfaces. Fig. 1.1 shows a typical PEC for the simplest case of a diatomic molecule, say AB. Generally, the molecules of common occurrence are stable and lie in its ground state (curve $A$). Under external perturbations, however, the molecule can go to in its different excited states. The shape of the potential energy curves (PECs) of excited states determines whether the molecule is stable, unstable or metastable against dissociation. The molecules or ions that have a global minimum in their PEC at finite internuclear separation are stable, i.e. the resultant molecular species do not dissociate spontaneously. The nuclei of such species can vibrate in the potential well formed around the equilibrium position $R_0$ and give rise to discrete 'vibrational energy levels'. The number of supported vibrational energy levels is then determined by the depth and shape of the corresponding PEC. Rotation of such molecules re-

sults in discrete 'rotational energy levels'. The species that have their minimum at infinite separation dissociate as soon as they are formed. Such molecular ions are regarded as unstable (curve $C$). The corresponding PECs are very steep in general, i.e. the state of molecular ion has repulsive nature which results in spontaneous dissociation into its fragments. A state with stability between entirely stable and entirely unstable is termed as metastable molecular state (curve $B$). Although, the corresponding PEC or PES does not have a global minimum but it has a local minimum. Because of the existence of such local minimum, the molecule or ion formed in metastable state can exist for a short period of time before its dissociation through potential barrier by tunneling. Such systems may support discrete vibrational or rotational energy levels depending on their life times against dissociation.

A molecule can be perturbed by interaction with different projectiles viz photon impact or charge particle impact. Charge particle projectile can be of several types such as electron, proton or highly charged ion (HCI). Depending on the interaction or energy deposited to the target molecule by projectile, different excited states of molecule can be observed. If the energy deposited is comparable to the vibrational or rotational energy then molecule is vibrationally or rotationally excited. In this case, molecule remains in the same potential well (curve $A$). With sufficient vibrational excitation, the molecule can dissociate into its neutral fragments. If the energy deposited is large enough and it is taken by the electrons, it may result in removal of one or more electrons and this electronic excitation process is known as ionization. If the molecular ion thus formed is unstable (curve $C$) then it can quickly dissociate into its fragments. Such process is known as dissociative ionization, and this is mainly studied in the present thesis work. Dissociation of a molecule occurs when it is excited into such an electron-nuclei configuration that the minimum of potentially energy is only obtained when the nuclei are far apart i.e. free from any mutual interaction. In the electronic excitation, the nuclear configuration of molecule experiences no significant change since the nuclei are more massive than electrons. This is described as Franck-Condon principle. Hence, excitation is shown as a vertical transition from one electronic state to other in PEC diagram.

In ion-molecule collision, the ionization of target can occur via different ionization processes named as direct ionization, capture ionization or transfer ionization.

Capture and transfer ionization are collectively termed as charge-exchange ionization. In direct ionization, the charge state of projectile remains same after the interaction with the target while in the charge-exchange process, the charge state of the projectile changes. Different ionization channels are shown in the following equations,

$$\mathrm{P}^{q+} + \mathrm{T} \rightarrow \mathrm{P}^{q+} + \mathrm{T}^{n+} + ne^{-} \quad \text{(direct ionization)} \tag{1.9}$$

$$\mathrm{P}^{q+} + \mathrm{T} \rightarrow \mathrm{P}^{(q-c)} + \mathrm{T}^{c+n} + ne^{-} \quad \text{(capture ionization)} \tag{1.10}$$

$$\mathrm{P}^{q+} + \mathrm{T} \rightarrow \mathrm{P}^{(q+t)} + \mathrm{T}^{t-} + ne^{-} \quad \text{(transfer ionization)} \tag{1.11}$$

where P and T represent the projectile and the target, respectively while $c$, $t$ and $n$ represent the number of capture electrons, transfer electrons and free electrons, respectively. Depending on the properties of projectile, different ionization processes may have varying probabilities. The excitations by different charged projectiles are briefly discussed in the following subsections.

### 1.2.1 Electron impact

The electron is the simplest and a structureless charged projectile. The dynamics of an atom or molecule under electron-impact is widely studied in the field of collision physics [25, 26, 27, 28, 29]. In particular, $(e, 2e)$ ionization process has been studied very extensively from a very long time [26, 30, 31] because it is a sensitive test of electron correlations. In $(e, 2e)$ process, the incident projectile electron collides with target and ionizes it by ejecting one electron from any of the shells of the target and the projectile scatters with a certain angle away from the ejected electron. Thus there are two electrons in the continuum and an ionized target in the final state. For the simplest target, the H-atom, $(e, 2e)$ process provides the simplest correlated three-body problem, where two electrons and one proton are moving in the continuum in long range Coulomb interactions of each other. The kinematics about $(e, 2e)$ process are usually obtained by measuring the triple differential section (TDCS) which is proportional to the probability that two outgoing electrons will have certain energies and move in certain directions with respect to the fixed axis. Questions such as how the TDCS changes with impact energy of projectile

electron or with the energy of ejected electron moving in a certain direction have been fundamentally important theoretically and experimentally. The experimentally observed TDCS gives insight into the ionization dynamics and, it provides a sensitive test of different theoretical models. Similarly, $(e, 3e)$ process results in a correlated four-body problem, and also well studied particularly for simple target as He-atom [29].

Electron attachment to the molecule is another widely investigated process. Here, at low energy (order of eV), electron can be captured by the molecule forming the negative molecular ion, and the process is known as resonant attachment. The negative molecular ion will further dissociate into a negative ion and neutral atom, which is termed as dissociative electron attachment (DEA)[32].

Cross section of multiple ionization ($\geq 3+$) of a molecule by electron-impact is very low, order of $\approx 10^{-19}$ cm$^2$. Nonetheles, in recent years, the dynamics of dissociative multiple ionization of polyatomic molecules such as $CO_2$, OCS, etc have been investigated under electron-impact [33, 34, 35]. Besides theoretical interest as one of the basic collision phenomena, electron-impact ionization has many applications in lasers, astrophysics, plasmas, etc. [36, 37].

### 1.2.2 Proton impact

The fundamental importance of the phenomenon of ionization by positive-ion impact has been recognized for a long time [38, 39, 40, 41]. One important tool for understanding the dynamics in many electron system is the study of collisions between bare ions and a noble gas target [42, 43]. Proton ($H^+$) is the simplest bare projectile ion. Proton-impact experiments on atomic system have provided great insight in understanding the multiple ionization processes occurring through different channels such as (i) direct target ionization (ii) charge transfer with or without additional ionization (iii) inner-shell ionization followed by post-collisional electron emission, like Auger or Coster-Kronig processes [44, 45, 46]. The results of these experiments help in theoretical advancement of the collisional dynamics of many electron targets.

Significant progress has been made in theoretical as well as experimental description of ion-atom collision in recent years. However, the situation is different for the

molecular targets. This is due to multicentre nature of molecular target. The interest in accurate calculations and experimental advancement for collisions involving molecular targets has been growing recently because of their relevance in number of fields such as atmospheric science, radiation and ion-beam tumor treatment. From a basic physics point of view, ion-molecule collisions offer a wealth of interesting questions concerning many-body theory [47, 48].

### 1.2.3 Highly-charged ion impact

Highly-charged ion (HCI) impact on molecule constitutes a rather more complex collision system which is more challenging both experimentally and theoretically [49, 50]. However, HCI impact is an efficient way to produce multiply ionized molecular ion. The collision system consists of HCI and molecular target has fundamental importance in a variety of fields such as atmospheric physics, astrophysics and radiation biology [51, 52, 53, 54] . It also constitutes a suitable system to study the fundamental collision physics and many-body physics [55, 56, 57].

In particular, slow HCI ($v < 1$ a.u.), produce a strong perturbation to multiply ionize the molecular target and breaks its bond. Hence, the molecule should respond differently here from what is observed in weaker perturbation. The perturbation strength is generally parametrized by Sommerfeld parameter ($k$) which is defined as the ratio of projectile charge ($q$) to its velocity ($v$), i.e. $k = q/v$, where $q$ and $v$ are in atomic units (a.u.). At small $k \ll 1$, interaction strength of projectile with target is weak and first order perturbation theories are applicable. In this regime, the ionization probabilities and characteristics of dissociation process are found to be well parametrized by Sommerfeld parameter ($k$) [58, 59]. However, in case of strong interaction regime ($k > 1$), the ionization probabilities and characteristics of dissociation process do not show a simple dependence on '$k$', and so the Sommerfeld parameter is no longer a suitable factor in strong perturbation regime [60, 61]. In ion impact, for $v \gg 1$ a.u, the ionization cross section varies with $q^2$, while in case of $v \leq 1$ a.u, ionization cross section deviates from $q^2$ dependency, and this variation is based on the atomic targets [49].

Furthermore, the richness of HCI impact lies in the possibility of different ionization processes, viz direct ionization and charge-exchange ionization, through which

ionization of target can occur. A wide range of excited states of a molecular ion can be accessed via these processes. For a given charge state of HCI, the probability of these processes depends on the impact velocity with the target. In collisions with swift HCI projectiles ($v \gg 1$ a.u.), direct ionization is the dominant process of electron removal [62, 63]. For slow impact ($v < 1$ a.u.), charge-transfer is the dominant process. In fact, for slow HCI, the capture ionization is more probable type of charge-exchange process than transfer ionization [64, 65]. In particular, capture ionization by slow HCI has greater importance in the astrophysical environment. Capture induced ionization processes are considered one of the prominent mechanisms responsible for soft x-ray emissions from comets as they transit our solar system [66, 67].

## 1.3 Dissociation dynamics of molecular ion

Dissociation of multiply ionized molecular ions into multiple fragments has been a subject of fundamental study, theoretically and experimentally, from decades. Experimental efforts are generally focused on obtaining information on the energetics involved in the formation and dissociation of multiply ionized molecular ion, and the interaction of the outgoing fragments with each other. Theoretical studies primarily address the question of the stability, metastability or instability of multiply ionized molecular ions, and focus attention on calculations of molecular ion's potential energy curves/surfaces. One of the pioneering works to investigate the many-body dissociation process of polyatomic molecular ion was reported by Eland *et al.* [68] in 1987, via triple coincidence PEPIPICO (photoelectron-photoion-photoion coincidence) measurement using time-of-flight mass spectrometry. It was one of the first attempts to distinguish whether the molecular ion breaks into fragments instantaneously (concerted or Coulomb explosion) or sequentially (step-wise). Following this work, in 1989, Hagan *et al.* [69] reported the formation of triply ionized molecular ion and its three-body dissociation under high energy (0.5 to 1.5 keV) electrons impact. Compared to the photon, however, electron impact studies have a challenge with the small cross section of producing multiply ionized molecular ions.

Dissociation process of a molecular ion is governed by the properties of its po-

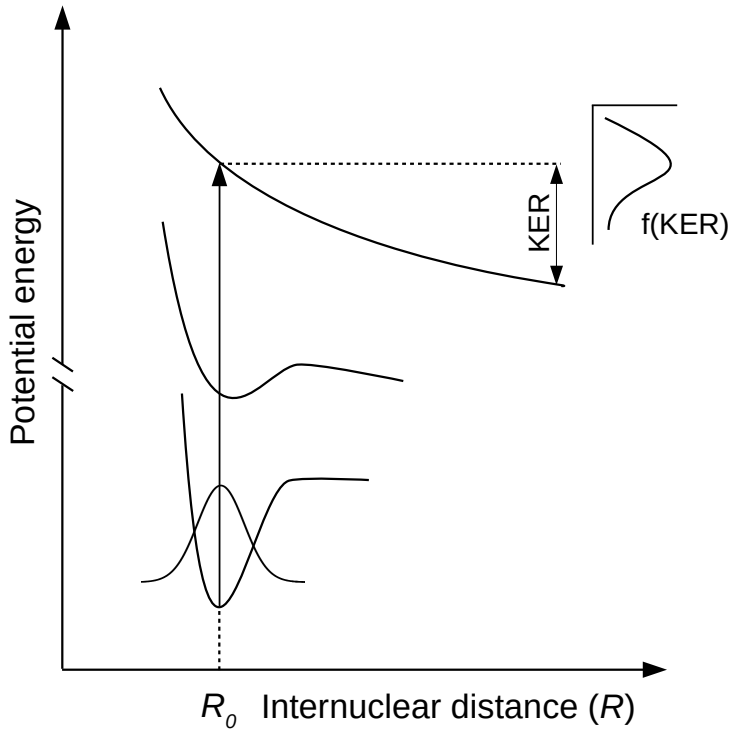


Figure 1.2: A schematic diagram showing molecular excitation from its ground state to a dissociating state. A Gaussian probability density of the ground vibrational state is shown projected to dissociative state of molecule. Depending on the properties of dissociative excited state, kinetic energy release (KER) distribution of fragments is observed.

tential energy curves (PEC). A schematic, shown in Fig. 1.2, depicts the excitation of a molecule from its ground state to a dissociative state. During dissociation, the potential energy possessed by the excited molecule transforms into the kinetic energy of fragments. For a given dissociation event, the sum of the kinetic energies of all fragments is known as kinetic energy release (KER), and its distribution can lead to a wealth of information about the participating PEC. In 1992, employing coincidence time-of-flight mass spectrometry, Mathur *et al.* [70] studied photo-induced two-body dissociation of a diatomic molecular ion, and they experimentally derived KER spectra of fragments. With the help of KER spectra and available PEC calculation by Krishnamurthi *et al.* [71], they could identify the participating electronic states of the molecular ion $CO^+$. It is found that the determination of the KER distribution of the fragment ions makes it possible to provide a stringent experimental test for the reliability of quantum chemically calculated shapes of PEC of various

electronic states of the molecular ion. Over time, several experiments were also focused on exciting the atomic core-shell in the molecules under photon impact with controlled energy deposition to the target [72, 73]. Core excitation generally results in the formation of multiply ionized molecular ions via Auger electron decay. Energy selected Auger electrons spectroscopy unravels the complex dissociation processes of multiply ionized molecular ion formed due to core-shell ionization [74].

Another efficient way to create multiply ionized molecular ions is with highly charged ion (HCI) impact. Unlike photon impact, there is no control over the energy deposition on the target under ion impact. A number of excitation channels of molecular ions are opened up in HCI impact. With the development of ion momentum spectrometry, where all three momentum components of fragments can be mapped, the study of collision-induced dissociation process of polyatomic molecular ions became more feasible. In the last couple of decades [58, 62, 75] a number of experiments attempted to study the dissociation process of polyatomic molecular ions under swift ($v \approx$ tens of a.u.) HCI impacts. Theoretically, a simple Coulomb explosion (CE) model was adopted to describe the angular and energy distributions of observed fragment ions. In this model, dynamical parameters are determined by calculating the Coulomb forces among fragment ions treating them as point charges. In their experiments, Siegmann *et al.* [62] found that the mean KER value observed in dissociation of higher charged molecular ion $CO_2^{6+}$ is comparatively closer to that predicted by the CE model. However, for lower charged molecular ions, the deviation between them is significantly large. It indicates that the shape of the corresponding PECs is not strictly Coulombic, and the simple assumption of point charges for a many-electron system is not sufficient.

Later on, dissociation of multiply ionized molecular ions created under slow ($v < 1$ a.u.) HCI impact on polyatomic molecules caught attention because of its fundamental importance in the interstellar and planetary atmosphere. In slow HCI impact, multiply ionized molecular ions are generally formed via multiple capture of electrons from the molecule. In recent times, in 2010, Neumann *et al.* reported pioneering results on three-body dissociation dynamics of $CO_2^{3+}$ by slow ($v \approx 0.3$ a.u.) HCI $Ar^{8+}$ impact [76]. Apart from the angular distribution of fragments and KER distribution, they could efficiently separate sequential and concerted bond

breaking mechanisms of $CO_2^{3+}$ with the help of the Dalitz plot and Newton diagram. KER distributions observed in slow HCI impact are found to show even more deviation from the CE model. Following Neumann's work, in the last decade, different groups investigated the dissociation dynamics of molecular ions under perturbation of slow HCI impact [77, 78, 79, 80]. Many of these investigations revolve around the question of how the dissociation dynamics of multiply ionized molecular ions are influenced by specific projectiles. Some of these investigations by Chen *et al.* [79] in 2019 and Wang *et al.* [80] in 2021 are also focused on understanding the influence of capture processes on dissociation dynamics of molecular ions upto a certain extent.

Theoretically, ionization processes, i.e. direct and capture processes are comparatively well explored in ion-atom collisions. Most of the quantum-theory calculations of ionization have been in various versions of the Born approximation [38, 81, 82, 83]. It was realized that perturbation theories such as lower order Born approximations are not appropriate where strong interactions are involved, such as in the case of an HCI colliding with a target. Olson *et al.* applied the classical trajectory Monte Carlo (CTMC) approach successfully for HCIs in the intermediate velocity range ($v = 1$ a.u. to $\leq 3$ a.u.) [84]. These results have clearly shown the deviation of ionization cross section from simple $q^2$ dependency as encountered in the case of high energy ($v \gg 1$ a.u.) theories where the probability for the capture process becomes very small. In slow ($v < 1$ a.u.) regime, where the capture process is dominant, the classical over barrier (COB) model has been successfully applied in atomic targets and has also been approximated to simple diatomic molecular target [60, 85, 86]. According to the COB model, an electron transfer from the target to the ionic projectile takes place when the potential barrier between the ionic attractive wells is so low that the Stark-shifted binding energy of the electron equals the top of the barrier.

The complex electronic structure of polyatomic molecules and the involvement of various ionization processes in ion-molecule collision make it challenging to understand the outcome of such collision induced dissociation dynamics of created molecular ions theoretically and experimentally. This work is an experimental attempt in that direction.

## 1.4 Focus of this thesis

This thesis deals with the experimental investigation of dissociation dynamics of multiply charged molecular ions formed under strong perturbation created by the slow ($v < 1$ a.u.) projectile ions. As discussed in the previous section, several groups have focused on the dissociation dynamics of molecular ions under various individual charged projectiles; however, there is no systematic study to address the question of how projectile properties, i.e. its charge ($q$) and velocity ($v$) affect the kinematics of many-body dissociation process. Moreover, the effects of underlying ionization processes, through which intermediate transient molecular ions are formed, on the dissociation of molecular ions are less explored.

In our study, taking $CO_2$ as a convenient model molecule, we have investigated the three-body breakup of $CO_2^{n+}$ (where $n = 3, 4$) molecular ions created by various HCIs, $Ar^{q+}$ and the simplest projectile ion, the proton ($H^+$), in a slow impact ($v < 1$ a.u.) regime. Our systematic study shows that in slow impact regime, the projectile charge state, $q$, influences the probability of accessing different excited electronic states of the transient molecular ion. Furthermore, we have explored the three-body dissociation dynamics of $CO_2^{3+}$ molecular ion under a simplest projectile ion, the proton. Despite being a structureless projectile, a slight variation in the impact velocity $v$ of the proton affects the kinematics in three-body breakup of $CO_2^{3+}$ molecular ion in slow impact regime.

Furthermore, to study different ionization processes, such as direct ionization and capture ionization, in ion-molecule collisions, we have designed a post collision charge state analyzer which is augmented with the existing ion-momentum spectrometer (IMS). We show that the branching ratio of various observed fragments ions are significantly influenced by the different order of capture processes. Moreover, capture processes influence the relative probabilities of accessing different electronic states of molecular ions.

The thesis is organized in the following manner. After this introductory chapter 1, chapter 2 describes the collision setup used to perform this work, the data acquisition and calibration method. Chapters 3 and 4 describe the results for dissociation dynamics of $CO_2$ molecular ions formed under slow HCI and proton impact, respectively. Chapter 5 contains the description of a post collision charge state ana-

lyzer, its design, calibration and experimental implementation. Chapter 6 presents some results of dissociation dynamics of $CO_2$ molecular ions for different ionization processes employing the charge state analyzer. Finally, chapter 7 summarizes all results presented in this thesis. A future outlook in the continuation of this work is also discussed.

# Chapter 2

# Ion source and collision setup

The investigation of dynamics involved in the dissociation process of molecular ions requires a set of different experimental tools. All the experiments presented in this thesis are performed at the electron beam ion source (EBIS) facility at IISER Pune, India [87]. This chapter describes the various components of the experimental setup used in this thesis work and the data acquisition methodology.

Fig. 2.1 displays a schematic diagram of a collision system comprising an incident projectile ion interacting with a randomly oriented triatomic molecular target. Such interaction can be an elastic scattering or inelastic scattering. An inelastic scattering may result in the molecule's rotational, vibrational or electronic excitation. Here, we are interested in electronic excitation, which leads to multiple ionization of the target. The dissociation of so-formed multiply ionized molecular ion constitutes a dynamic many-body coulombically interacting system. This thesis is focused on studying the kinematics of such dissociation processes of molecular ions under charged particle impact. In order to perform such experiments, one requires an ion source, molecular target and a collision setup, equipped with detector to perform multi-hit measurements. Apart from these basic requirements, a data acquisition system to store multi-parameters and a data analyzing platform for offline analysis are needed. In the coming sections, these various elements of the experimental setup are discussed in detail.

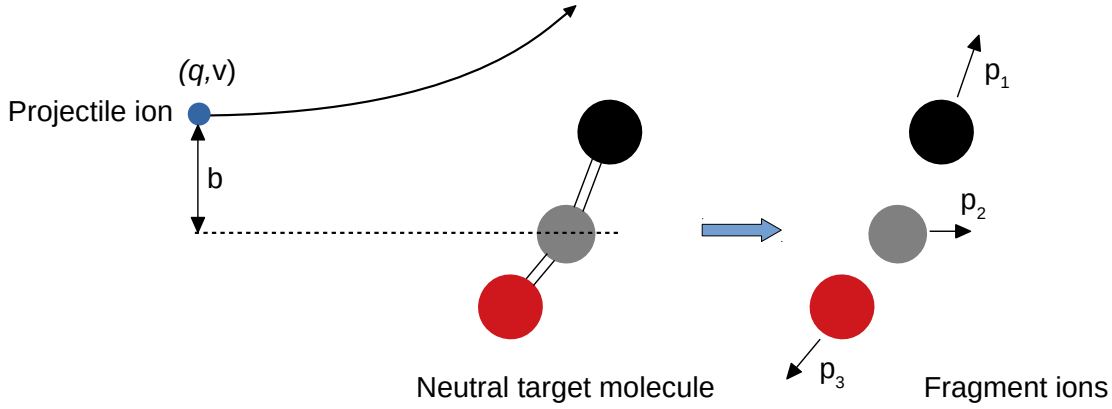


Figure 2.1: A schematic diagram of a ion-molecule collision system. $q$ and $v$ represent the charge and velocity of a projectile ion, respectively. After collision, the fragment ions move apart in a continuum with momentum vectors $\vec{p_1}$, $\vec{p_2}$ and $\vec{p_3}$.

## 2.1 Electron beam ion source (EBIS)

Electron beam ion source (EBIS), installed at IISER Pune, is a compact room temperature operated ion source for producing highly charged ions (HCIs) in the keV energy range. The source is manufactured by Dreebit GmbH, Germany [88]. Its principle of operation is based on successive electron impact ionization of initially neutral atoms in a high density electron beam in the presence of confining magnetic and electric fields. Fig. 2.2 shows a layout of different components of EBIS along with a scheme of potentials. The high current cathode ($\approx$ 3–4 amp) emits an electron beam of high current density ($\approx$ several hundreds of amp/cm$^2$) which is guided through three drift tubes forming the ion trap. After the drift tubes, the electron beam is dumped onto a water-cooled collector. The electron beam is compressed by an axially symmetric magnetic field created by a permanent magnet of strength 1 tesla. The drift tube region is filled with the appropriate gas. Successive collision of electrons with neutral atoms results in a charge distribution of atomic ions. The approximate impact energy $E_e$ of an electron with neutral atoms is determined by the sum of cathode potential $U_{cath}$ and $(U_0 - U_A)$.

$$E_e = e\,[U_{cath} + |U_0 - U_A|] \tag{2.1}$$

The negative space charge of the electron beam forms a radial trapping potential for produced ions. Axial trapping of ions occurs due to potential difference between

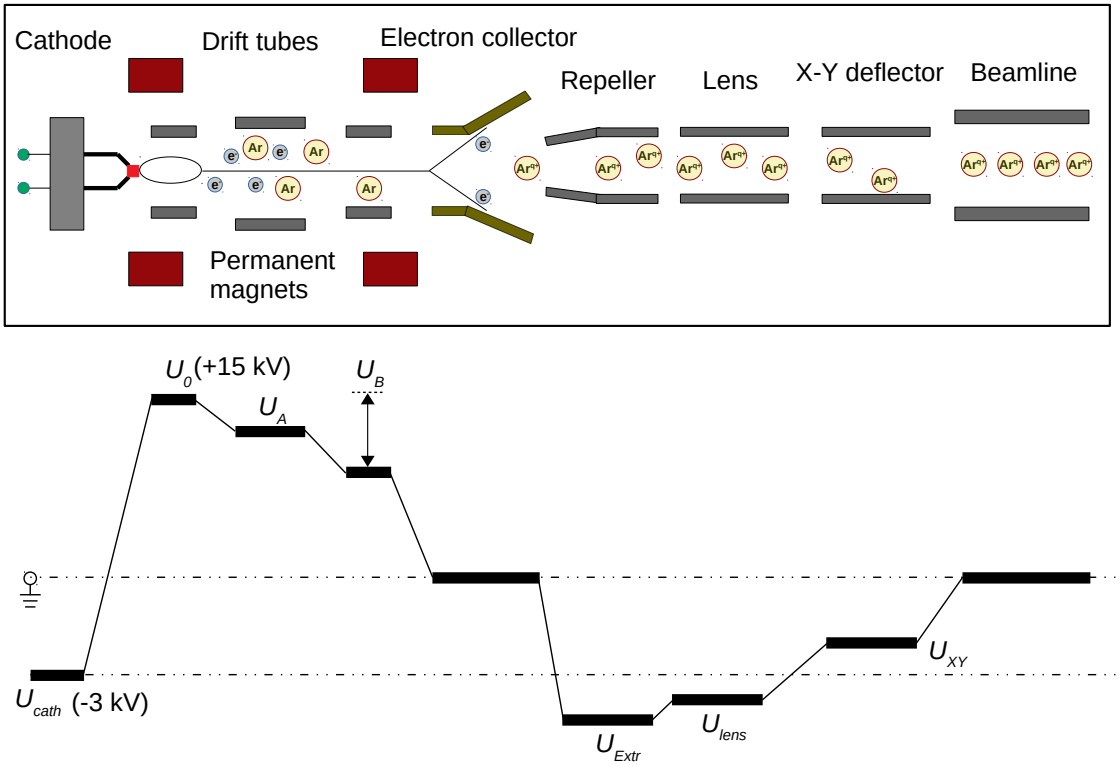


Figure 2.2: A schematic layout of EBIS and its components are shown (top). A typical scheme of the potentials applied on different elements are drawn (bottom). Typical values of potentials applied on cathode ( $U_{cath}$) and drift tube ( $U_0$) are shown. Potential differences are not to scale. The ground plane shown in the schematic can be floated to a high positive potential to provide the required acceleration.

the centre and the third drift tube section. The drift region is maintained at a high vacuum condition ($\approx 2{\times}10^{-10}$ mbar) to minimize the charge exchange process with residual gas.

The ions are selected by pulsing the voltage $U_B$ on third drift tube downstream from the cathode to a lower value than the voltage $U_A$ applied on the central drift tube. Ion source can also be operated in a leaky mode. For this, the potential $U_B$ on third drift tube is set at slightly higher (shown by the dashed line), which allows a fraction of ions to escape the trap for extraction. The energy of extracted ion of charge $q$ depends on the drift tube voltage $U_0$ and is given by

$$E_{ion} = qU_0 \tag{2.2}$$

The whole EBIS platform can also be floated with respect to the ground at a high voltage $U_{float}$ up to 10 kV to achieve even higher energies ions. In the present

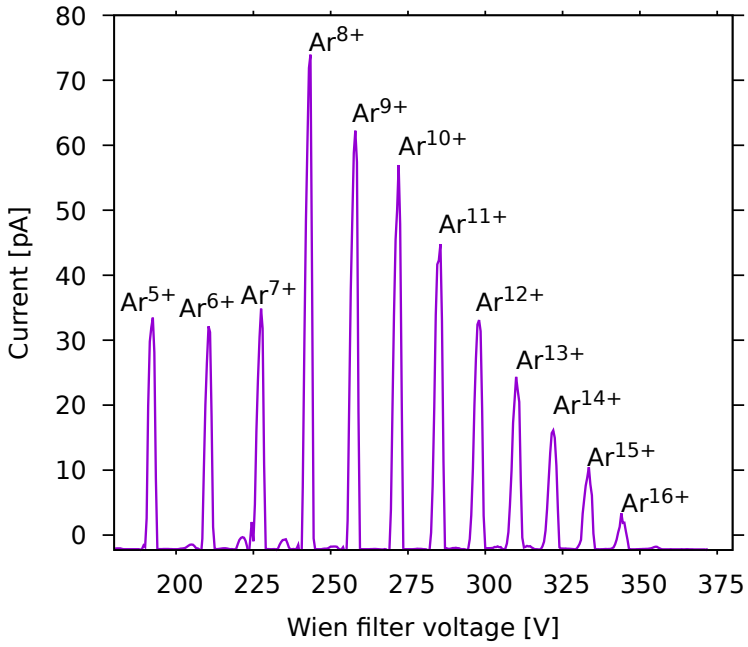


Figure 2.3: The charge state distribution of extracted ions. It is output of Wien filter scan. The energy of each ion is 8 keV/$q$.

setup, the upper voltage limits of $U_0$ and $U_{float}$ are 15 kV and 10 kV, respectively. Therefore, the ions can be obtained at energies up to 25 keV/$q$. The extraction element incorporates an electron repeller, Einzel lens and quadrupole deflectors for efficient transmission and good shape of the ion beam.

Ions of various charge states are selected with the help of a Wien filter. The Wien filter is basically a crossed configuration of a mutually perpendicular electric field and magnetic field. An ion of a particular velocity, satisfying $v = E/B$ condition, will pass through the Wien filter in a straight path without deflection. All other ions with different velocities will deflect and hit between the Wien filter apertures. Since the potentials in the ion source are the same for all charge states, the velocities of species with different $m/q$ will be different. Thus, the Wien filter serves as a species selector. Here, a permanent magnet of strength 0.5 T is used, and Wien filter voltage is varied to pass the ions of different charge states of a given ion specie. During the Wien filter scan, a Faraday cup is inserted at the exit of aperture to measure the ion beam current. The aperture of the Wien filter is 1 mm. Fig. 2.3 displays a typical charge state distribution of extracted Ar-ions, each with 8 keV/$q$ energy. A wide range of ions of various elements (in principle, most of the elements in the periodic table) can be obtained at energies up to 25 keV/$q$. The mean charge state of extracted

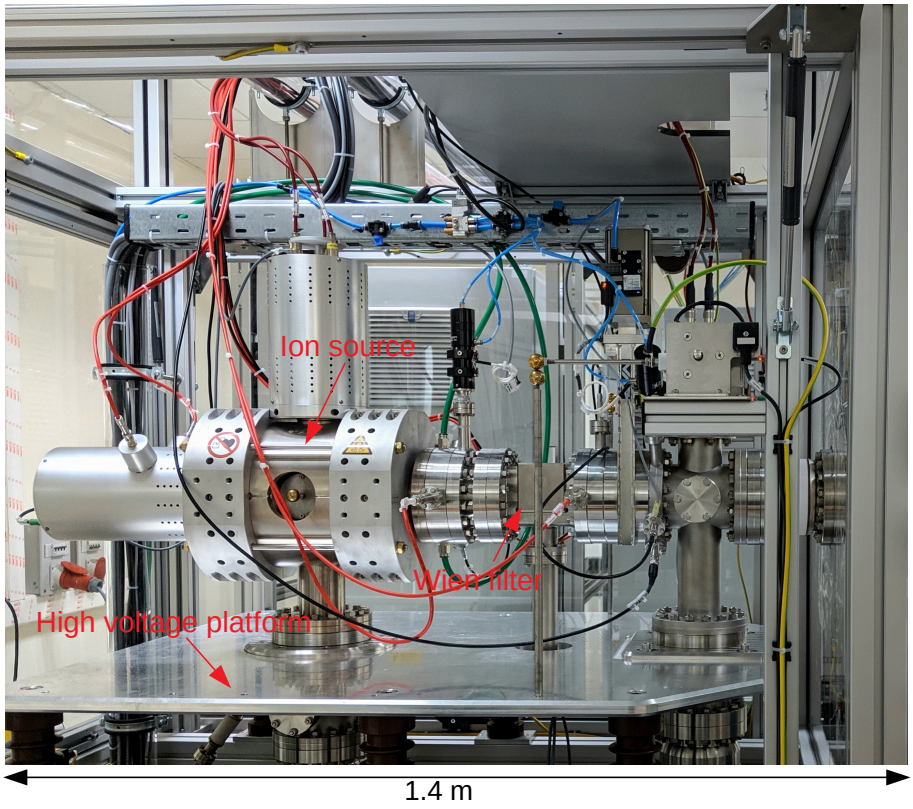


Figure 2.4: A Photograph image of EBIS assembly installed at IISER Pune.

ion distribution can be varied by adjusting the confinement time, the time for which the axial trap is closed. The other important parameters influencing the charge distribution are input gas pressure and the cathode's electron emission current. The choice of these parameters becomes more crucial particularly for producing highly charged ions. The distribution of the ions in the trap very sensitively depends on the trapping parameters when high charge states are being produced. A particular Ar-ion can be selected to transmit it for further application by applying suitable Wien filter voltage. Fig. 2.4 shows a photograph of the complete EBIS assembly. The voltage on each component of EBIS is remotely controlled using LabView software.

## 2.2 The collision setup

The energetic ion beam delivered from EBIS is transported to the collision chamber, where the ion beam overlaps with the target molecule of interest. Such collisional events create various multiply ionized molecular ions of the target molecule. In order to study the dissociation dynamics of a so-formed molecular ion, the observed

fragment ions need to be identified, and their momentum components need to be determined event by event in coincidence. The setup is based on a time-of-flight (ToF) mass spectrometer with position sensitive detection, which is discussed in the next section.

### 2.2.1 Time of flight mass spectrometry

By definition, a mass spectrometer is a device capable of analyzing ions according to their mass-to-charge ratio. The ToF mass spectrometer is based on the temporal dispersion of ions subjected to an electrostatic field. In the simplest general form, there is a pulsed source of ions and one charge particle detector fixed at the end of an evacuated tube. In the ion-molecule collision, the source of ions could be fragment ions formed upon the collision. The fragment ions are guided toward the detector through a constant uniform or pulsed electrostatic field. The time taken ($t_0$) to reach the detector under a given electrostatic field, of ions having mass ($m$) and charge ($q$) and zero initial momentum is given by

$$t_0 = \mathrm{A}\sqrt{m/q} + \mathrm{B} \tag{2.3}$$

where constant A depends on the geometrical properties of the spectrometer. In order to measure the time information experimentally, it requires start signal. In basic ToF spectrometer, the time start is obtained from the source pulse. In some cases, the time start signal is also obtained by the ejected electron observed upon the ionization of target in collision experiments. Constant B represents an offset between the recorded start time and the actual start time. Both A and B can be determined by knowing the $t_0$ values of at least two given ions.

In real case, there is a spread around the mean value $t_0$ due to non-zero spatial extent of projectile and target overlap and internal energy spread of ions. These conditions limit the mass resolving power ($m/\Delta m$) of spectrometer. The time taken by ion having non-zero initial momentum is denoted by $t$. Apart from the geometry of the spectrometer, the ToF ($t$) of an ion depends on the configuration of the electric field down through the spectrometer. Two widely adopted electric field configurations exist, single field and double field ToF mass spectrometers. In first

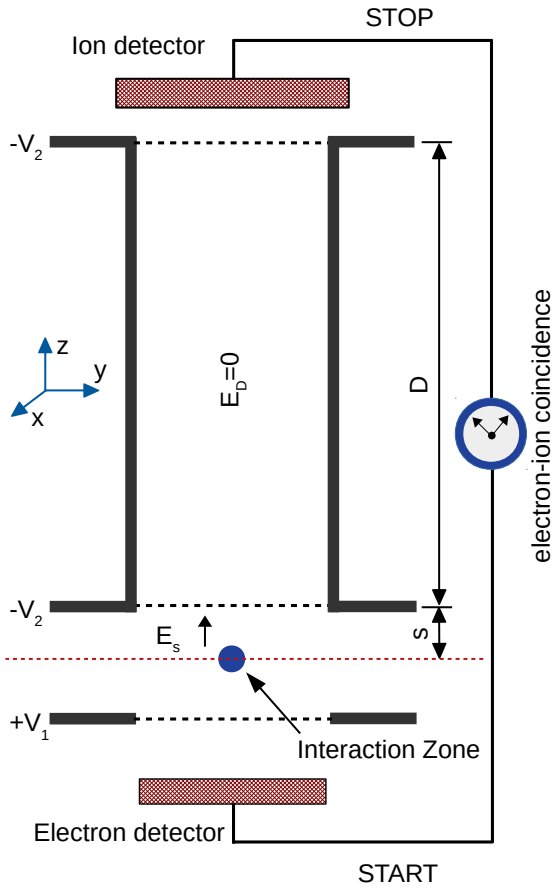


Figure 2.5: Schematic of a typical single field time-of-flight (ToF) mass spectrometer. Meshes (black dashed line) on which suitable voltages are applied to produce an uniform electric field $E_s$ for ion extraction. The red colour dashed line represents the collision plane where projectile and target interacts, shown by blue dot. The length of extraction and field free drift region are written as $s$ and $D$, respectively.

case, the spectrometer has one region having a linear electric field, with an optional field free region. In the latter case, ions are accelerated by a secondary electrostatic field after extraction before entering a field-free drift region. In principle, many such acceleration fields can be employed to improve mass resolution. Here, we will focus on single field with drift region configuration which has been employed in our experiments. The full details and principle of the ToF mass spectrometer are well described in articles [89, 90].

Fig. 2.5 shows a schematic diagram of a single field ToF mass spectrometer. The interaction zone represents the overlap of the projectile ion and target molecule. After the collision, the formed ions and electrons are guided, under extraction field $E_s$, towards two respective detectors positioned in opposite directions. Ions then enter a field-free ($E_D = 0$) drift region. The direction convention used throughout

the chapter is as follows: the electric field extraction $E_s$ points along the longitudinal direction ($z$-axis), and the direction perpendicular to $E_s$ presents the transverse direction ($xy$-plane). The lengths of ion extraction and drift regions are mentioned as $s$ and $D$, respectively. Experimentally, the measurement of time information requires a start signal, and here, ToF is measured by taking the START signal from the ejected electron signal. The STOP is marked by ion detection itself. Such a detection scheme is known as electron-ion coincidence measurement. In a collision event, if there are more than one fragment ions from the same event, it is termed as a multi-hit coincidence measurement.

A good analytical description of the ToF mass spectrometer requires no more than Newtonian physics, i.e. classical equation of motions will suffice to determine the ToF ($t$) of ions originating at the interaction zone. Let us consider that an ion of mass $m$ and charge $q$ is created in the interaction zone with initial longitudinal momentum $p_z$ along the extraction axis (ToF spectrometer axis). The time $t_s$ taken by ion to reach at drift region is given by

$$s = \left(\frac{p_z}{m}\right) t_s + \frac{1}{2}\left(\frac{qE_s}{m}\right) t_s^2 \tag{2.4}$$

By solving above equation, $t_s$ can be written as

$$t_s = \frac{-p_z/m + \sqrt{(p_z/m)^2 + 2(qE_s/m)s}}{qE_s/m} \tag{2.5}$$

The time $t_D$ taken by ion in drift region is given by

$$t_D = \frac{D}{\sqrt{(p_z/m)^2 + 2(qE_s/m)s}} \tag{2.6}$$

Hence, the total time ion takes to reach the detector is

$$t = t_s + t_D = \frac{-p_z/m + \sqrt{(p_z/m)^2 + 2(qE_s/m)s}}{qE_s/m} + \frac{D}{\sqrt{(p_z/m)^2 + 2(qE_s/m)s}} \tag{2.7}$$

Since the interaction zone has a finite spatial spread, two ions of the same mass and charge originating from two different locations will gain different energies upon passing through the extraction region. It will result in a spread in ToF around its

mean value. The spread can be reduced by employing first order space focusing Wiley-McLaren condition for single field configuration, which is $D = 2s$ [89]. The following equation can be obtained by setting $D = 2s$ condition and rearranging terms in Eqn. 2.7,

$$t = \frac{-p_z/m + \sqrt{2/m(p_z^2/2m + qsE_s)}}{qE_s/m} + \frac{2s}{\sqrt{2/m(p_z^2/2m + qsE_s)}} \tag{2.8}$$

The terms $p_z^2/2m$ and $qsE_s$ in the square root of both expressions represent the initial kinetic energy of ion corresponding to initial longitudinal momentum $p_z$ and kinetic energy gain of ion while traversing across the extraction region, respectively. There are mainly two causes for ions to have initial kinetic energy. One is the thermal spread of parent gas ensemble, and the other is energy gain of ions coming from some dissociation process. The thermal spread is the order of $\approx 0.02$ eV, and energy gain in dissociation process is of the order of $\approx 10$ eV. However, the energy ion gains from the extraction field is the order of a few hundred eV, much greater than the energy corresponding to the thermal spread and dissociation process. So, the approximation $p_z^2/2m << qsE_s$ holds good and Eqn. 2.8 can be rewritten as

$$t = -\frac{p_z}{qE_s} + 2\sqrt{\frac{m}{q}\frac{2s}{E_s}} \tag{2.9}$$

In the case of ion with zero initial momentum $p_z$, Eqn. 2.9 becomes

$$t_0 = 2\sqrt{\frac{m}{q}\frac{2s}{E_s}} \tag{2.10}$$

$t_0$ is the mean value of ToF distribution and $t_0 \propto \sqrt{m/q}$, where the proportionality constant depends on the spectrometer parameters, $s$ and $E_s$. Hence, ions of different mass-to-charge ratios $(m/q)$ will have different characteristics ToF values and, thereby, can be identified. Since the mean ToF value is proportional to the square root of mass, the mass resolving power of the spectrometer is given by,

$$\frac{m}{\Delta m} = \frac{1}{2}\frac{t_0}{\Delta t} \tag{2.11}$$

where $\Delta t$ is the full width half maximum value of the ToF distribution and the term

$t_0/\Delta t$ represents the ToF resolving power of the spectrometer. The ToF resolution strongly depends on the uniformity of the extraction field and the spatial spread ($\delta s$) of projectile and target gas overlap. Wiley-McLaren space focusing condition $D = 2s$ nullifies the $\delta s$ dependence to first order, thereby reducing the effect of spatial spread on ToF resolution.

### 2.2.2 Ion momentum spectrometer (IMS)

Let us go back to the Eqns. 2.9 and 2.10. Using these two equations, the initial longitudinal momentum component $p_z$ of ion can also be calculated by the following expression

$$p_z = qE_s(t_0 - t) \tag{2.12}$$

But how do you determine ion's transverse momentum components $(p_x, p_y)$? It requires position information $(x, y)$ of ion in the detector plane along with ToF $(t)$ information. Here, it is achieved by employing ion-momentum spectrometer (IMS) based on a single field ToF mass spectrometer capable of multi-hit coincidence measurements. The details of IMS used in this thesis work are well described in [91]. Fig. 2.6 shows a schematic diagram of IMS. It has a single uniform extraction field $E_s$ to guide fragment ions towards a microchannel plate (MCP) ($+z$ direction), of 80 mm diameter, with a two-dimensional position sensitive anode. Another MCP of 40 mm diameter is mounted in the opposite direction ($-z$ direction) to detect ejected electrons. Here, the output signal of electron MCP provides start signal to measure the time information of ions. The details and working principle of detectors will be discussed in the next section. The uniform electric field $E_s$ is generated by coaxial stacking of 12 thin aluminium rings, equally spaced in a potential divider arrangement. A horizontal red dashed line represents the collision plane, and the blue dot in this plane shows the projectile and target interaction zone. The top rings and bottom rings above the collision plane are labeled as $t_1....t_6$ and $b_1....b_6$, respectively. The inner and outer diameters of rings are 100 mm and 200, respectively. Just above the $t_6$ ring, which has a high transmission mesh, the field-free drift region for ions starts. In the present setup, the rings $b_3....b_6$ are grounded and redundant. The length $s$ of ion extraction and length $D$ of the drift region is 110 mm and 220 mm,

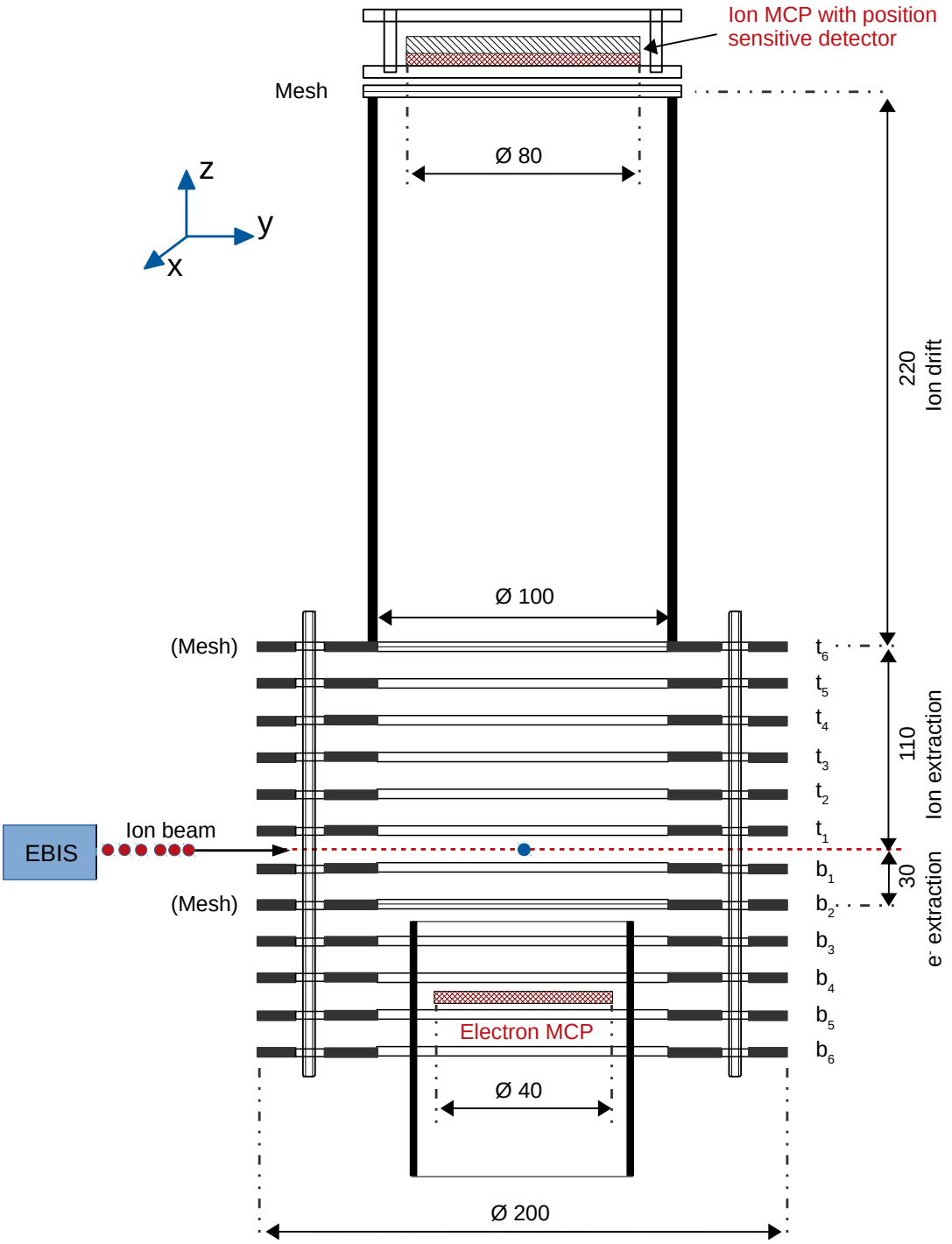


Figure 2.6: A schematic diagram of the 'ion-momentum spectrometer' (IMS), installed in our lab, is shown. The horizontal red dashed line between $t_1$ and $b_1$ is collision plane, in which projectile ion and target interact (blue dot). The rings $t_6$-$b_6$ are arranged to generate an uniform electric field to extract ions and electrons towards respective detectors. The dimensions of different regions are mentioned in mm.

respectively, following the Wiley-McLaren $D = 2s$ space focusing condition.

Fragment ions emanating in a collision between projectile and molecule can go

in any direction. The unidirectional uniform electric field $E_s$ projects all fragment ions onto a position sensitive detector, which enables us a $4\pi$ detection of fragments. By recording ToF ($t$) and position information $(x, y)$ of fragments in the detector plane, the momentum information of the ion can be retrieved using the following equations,

$$p_z = qE_s(t_0 - t) \quad , \quad p_x = \frac{m(x - x_0)}{t} \quad , \quad p_y = \frac{m(y - y_0)}{t} \tag{2.13}$$

where $q$ and $m$ are the charge and mass of ion, respectively. $t_0$ is the ToF of the same ion having zero initial momentum $p_z$. $(x_0, y_0)$ is the centroid of the interaction zone projected on the detector plane. Once the momentum components are known, various dynamical parameters can be derived.

### 2.2.3 Ion and electron detectors

In order to detect electrons and ions, a detector MCP is employed with an add-on position encoder, delay line anode (DLD) in the present setup. The ion detector is a combination of MCP and DLD, giving time and position informations of fragment ions. The electron detector consists of an MCP to give the START signal for ToF measurement.

#### Microchannel plate

A microchannel plate is extensively used for detecting single charged particles or photons. Its properties like high gain, high detection rate with multi-hit capability, and high spatial and temporal resolutions make it a suitable choice for ToF mass spectrometry. Fig. 2.7 displays the basic structure of MCP and its working principle. MCP is an array of a large number, of the order of $10^4 - 10^7$, single channel electron multipliers. Channels are fabricated with a special glass of a typical channel diameter of 25 $\mu$m and have a length to diameter ratio of 60:1. Each channel's interior is coated with a high resistance semiconductor that works as a secondary electron multiplier. Thus each channel can be considered as a continuous dynode. The glass microchannels in the array are oriented parallel to one other and parallel electrical

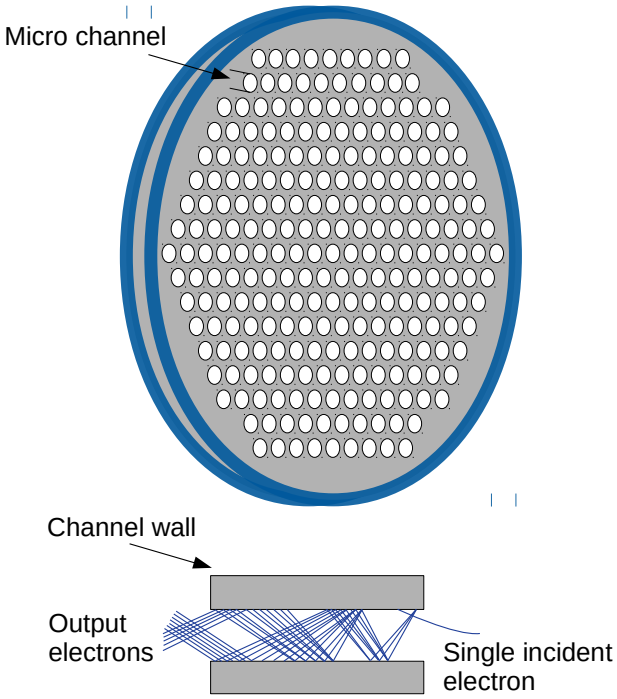


Figure 2.7: Schematic image of MCP (top) and a micro channel are shown (bottom). MCP consists of a large number of micro channels ($10^4 - 10^7$), and each channel acts as an electron multiplier which is shown in the bottom side.

contact to each channel is arranged by a metallic coating. Usually, a coating of Nichrome or Inconel is applied on the front and rear surfaces of the MCP, which serve as input and output electrodes, respectively. The total resistance between electrodes is of the order of $10^9$ Ω. A single incident ion enters a channel and emits a few electrons from the channel wall. These electrons are further accelerated down the channel by a positive bias and produce more secondary electrons; thus, a shower of electrons is generated at the end of MCP. The signal from the primary electron shower of the MCP is used to determine the arrival time of ion. Electrons shower at the end of MCP is further used to determine the incident ion position information, which is discussed in the next section. Stacking two MCP (called Chevron configuration) is useful for better performance due to increased gain. In the Chevron configuration, MCP allows electron multiplication factors of $10^6$, fast detection rate (1 MHz), high time resolution ($< 0.2$ ns) and high spatial resolution ($< 0.1$ mm) limited only by the channel dimensions and spacings. Our experimental

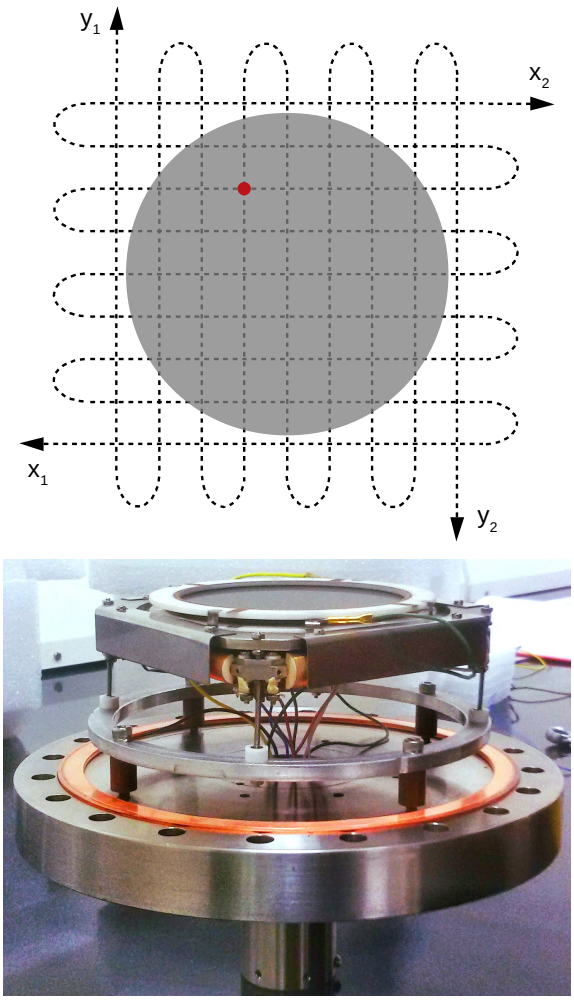


Figure 2.8: (Top) A schematic diagram of delay line detector coupled with MCP. A red dot shows the position of ion hit on the MCP front surface. The collection of four $x, y$ signals, that propagate from ion hit position, at the end of delay lines is also shown. (Bottom) A photograph image of MCP coupled with delay line detector taken at IISER Pune.

setup consists of two MCPs of 80 mm and 40 mm diameter for ions and electrons detection, respectively. The ion detector has a special anode for position encoding, which is described next. Both are purchased from Roentdek GmbH, Germany.

### Delay line anode

The combination of MCP and DLD provides a unique technique to extract position information of incident fragment ions on the MCP front surface. The details of DLD can be found in [92, 93]. The schematic diagram of DLD is shown in Fig. 2.8. It consists of two sets of parallel wire wounded around a rectangular support in many loops with wire spacing of $\approx$ 0.5 mm. The electron shower from the back of the

MCP is drawn to the delay line anode by a positive potential difference between the anode and back side of the MCP stack. In Fig. 2.8, red dot shows an electron shower hitting the DLD grid. Each ion hit creates electric signals that travel to the four corners named $x_1, x_2, y_1, y_2$ of the delay line. The position of ion is determined by the difference in the arrival times of signals at both ends of each parallel-pair delay line for each layer independently. The signal arrival time difference is proportional to the distance of electron shower from the midpoint of delay line. So the $(x, y)$ coordinate of ion in the detector plane can be obtained by

$$x = (t_{x1} - t_{x2})v_{sig} \tag{2.14}$$

$$y = (t_{y1} - t_{y2})v_{sig} \tag{2.15}$$

where $v_{sig}$ is signal propagation velocity along the delay line, which is almost equal to the velocity of light.

For instance, if the electron shower hits the centre $(0, 0)$, the time difference between the pair of signals reaching the corner of the delay line will be zero. For a given DLD, the length of delay line is fixed; therefore, the time sum $(t_{x1} + t_{x2})$ and $(t_{y1} + t_{y2})$ are constant. These sum conditions can be used as a consistency test for genuine signals. Thus, with the help of MCP and DLD, the ToF and position informations $(x, y)$ of ions can be found, which are essential for the momentum evaluation shown earlier in Eqns. 2.13. In our experimental setup, the active diameter of MCP+DLD is 76 mm with 250 $\mu$m position resolution and 1 ns time resolution.

## 2.3 Experimental setup

Experimental setup consists of an ion source (EBIS) and ion-momentum spectrometer (IMS) equipped with detectors (MCP, DLD) (see Fig. 2.6). All these components are individually discussed earlier. The interaction zone is an overlap region of projectile ion and target gas, at room temperature, crossing perpendicular to each other. Here, the target gas jet is prepared using an effusive beam produced by a capillary of an inner diameter of 0.15 mm and a length of 12 mm. At the exit of the capillary, the target gas number density is about $10^{13}$ cm$^{-3}$. Small target number density and small projectile ion beam current (few pico-amp) are essential to satisfy single

collision condition. In a single collision condition, an ion interacts with only one target molecule at a time. The momentum spectrometer is housed inside a stainless steel vacuum chamber height of 570 mm and a diameter 300 mm. The chamber is continuously pumped by a 520 lit/s turbo molecular pump backed by a scroll pump. The ultimate pressure of the chamber without target gas injection is $1.5\times10^{-9}$ mbar.

The projectile ions of different charge states ($q$), at energy up to 25 keV/$q$, can be delivered from the EBIS (Fig. 2.3). In this thesis work, Ar-ions and proton ($H^+$) are mainly used as projectiles, and $CO_2$ is taken as a neutral molecular target. The typical volume of the ionization zone is about 3 $mm^3$. Upon the projectile and target interaction, the formed fragment ions and ejected electrons are guided by an electric field of strength 60 V/cm towards the ion detector and electron detector, respectively. As we have discussed earlier, to determine the momentum of fragment ions, their ToF ($t$) and position information $(x, y)$ can be obtained by combining MCP and DLD. However, to store this information simultaneously in each collisional event, we need an efficient and fast data acquisition system also that enables us to analyze data offline after the completion of experiments.

## 2.4 Data acquisition

The data acquisition of the IMS comprises six timing signals. One from electron MCP, one from ion MCP and four signals from the delay lines. The electron MCP signal provides a master START in every event for all other five channels. The STOP signal of ion ToF is served by the ion detection pulse (output of ion MCP) itself. For each ion STOP, the delay line generates four output signals which are processed to know the position of ion hit. All six signals are separately amplified by a preamplifier and then fed to a constant fraction discriminator (CFD) to create NIM logic pulses from the preamplifier output. These NIM outputs are then fed to a multi-channel time-to-digital converter (TDC, LeCroy 133MTD) to digitize all time signals. Multi- channel preamplifier (FAMP6) and CFD (CFD4c) are procured from Roentdek GmbH, Germany. The digitized outputs are processed event by event and stored as a list-mode file (lmf) in a computer hard disk, and analysis software is called “Computer Based Online-offine Listmode Data Analyzer” (COBOLD in

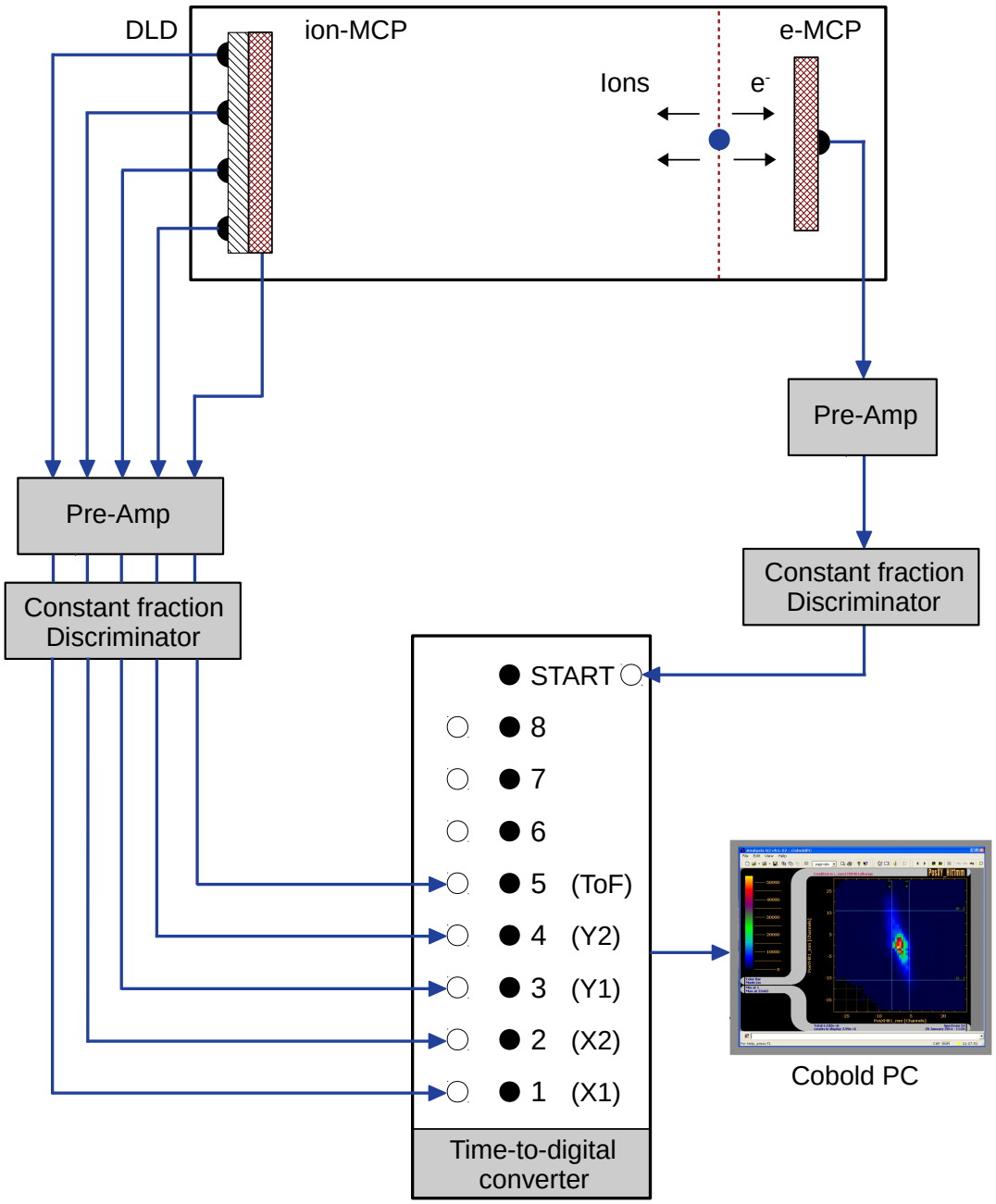


Figure 2.9: A schematic diagram of data acquisition of IMS setup is shown.

short). Fig. 2.9 shows the complete sequence of data acquisition.

In our TDC, for every electron trigger, the time window of TDC remains open for 32 $\mu$s with 500 ps resolution and after that clock automatically resets. In this time window, the detection of an electron (which starts the clock) and at least one ion is defined as an event. One ion detection is called a single coincidence measurement,

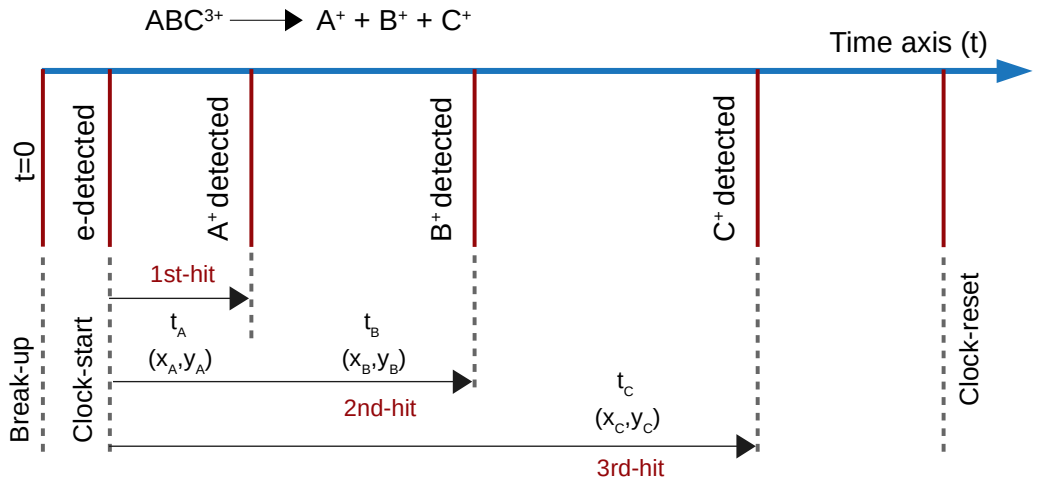


Figure 2.10: A schematic representation of multi-hit coincidence measurement of a molecular ion $ABC^{3+}$ dissociation. The typical time difference between two successive collision events is kept very large (about 100 times) in comparison to the time window used for multi-hit coincidence.

and if more than one ion is observed, it is called a multi-ion or multi-hit coincidence measurement. The dead time of detectors is 20 ns which defines the smallest time difference between the two consecutive ion hits to be recorded. In the current setup, we can have multi-ion detection up to quadruple-coincidence, which enables us to record complete correlated kinematics of the dissociation process involving up to four fragment ions. More details about the detection scheme, signal processing and data acquisition system can be found in [94]. A scheme of the multi-ion coincidence measurement is shown in Fig. 2.10. For example, a molecular ion $ABC^{3+}$ is formed in the event of an ion-molecule collision, and it subsequently dissociates into $A^+$, $B^+$ and $C^+$ fragment ions. The detection of the ejected electron is almost instantaneous ($\approx$ 25 ns) after the breakup, and it starts the clock for coincidence measurement. The fragment ion with the smallest $m/q$ ratio (here $A^+$) will have a smaller ToF and be registered as a first hit, and ion with the largest $m/q$ ratio (here $C^+$) will hit the detector at last. For example, in the real situation $H^+$ has the smallest ToF of around 1.2 $\mu$s. The TDC clock will reset after every 32 $\mu$s and start again in the subsequent collision event. In this way, event by event, the ToF ($t$) and position information $(x, y)$ of each fragment ion are saved as a list-mode file (lmf) in the computer for offline analysis after completion of the experiment. A schematic of the

| Event number | Ion1 | Ion2 | Ion3 |
|---|---|---|---|
| ... | ... | ... | ... |
| 101 | $(t, x, y)_{101,1}$ | – | – |
| 102 | $(t, x, y)_{102,1}$ | $(t, x, y)_{102,2}$ | $(t, x, y)_{102,3}$ |
| 103 | $(t, x, y)_{103,1}$ | $(t, x, y)_{103,2}$ | – |
| 104 | $(t, x, y)_{104,1}$ | $(t, x, y)_{104,2}$ | $(t, x, y)_{104,3}$ |
| 105 | $(t, x, y)_{105,1}$ | – | – |
| 106 | $(t, x, y)_{106,1}$ | $(t, x, y)_{106,2}$ | – |
| ... | ... | ... | ... |

Table 2.1: A typical schematic of the list mode data file for collision events. $t$ represents ToF and $(x, y)$ represents ion hit position.

event list is shown in Table 2.1. Inferences about specific outgoing channels in a collision experiment are based on the statistical distribution of events recorded in the experimental run. Some events may have a single collision product, i.e. molecular ion and some may have two, three or multiple fragment ions. The advantage of storing data event by event is that a particular event of interest can be chosen and analyzed independently. Moreover, as mentioned in Section 2.2.3 only those events carry complete time and position information which satisfy the delay-line time sum condition; therefore, other events can be filtered out during offline analysis.

## 2.5 Data analysis methodology

The raw data is further analyzed to construct various kinematical aspects of correlated observed fragment ions. This section discusses the calibration procedure, identification of various dissociation channels and different kinematic parameters in detail. The entire data has been analyzed using the ROOT platform [95]. Both Cobold and ROOT can be used for acquisition as well as analysis. Cobold is chosen for acquisition since it has pre-compiled modules for the hardware being used, and doing this via ROOT would require writing codes. On the other hand, the enor-

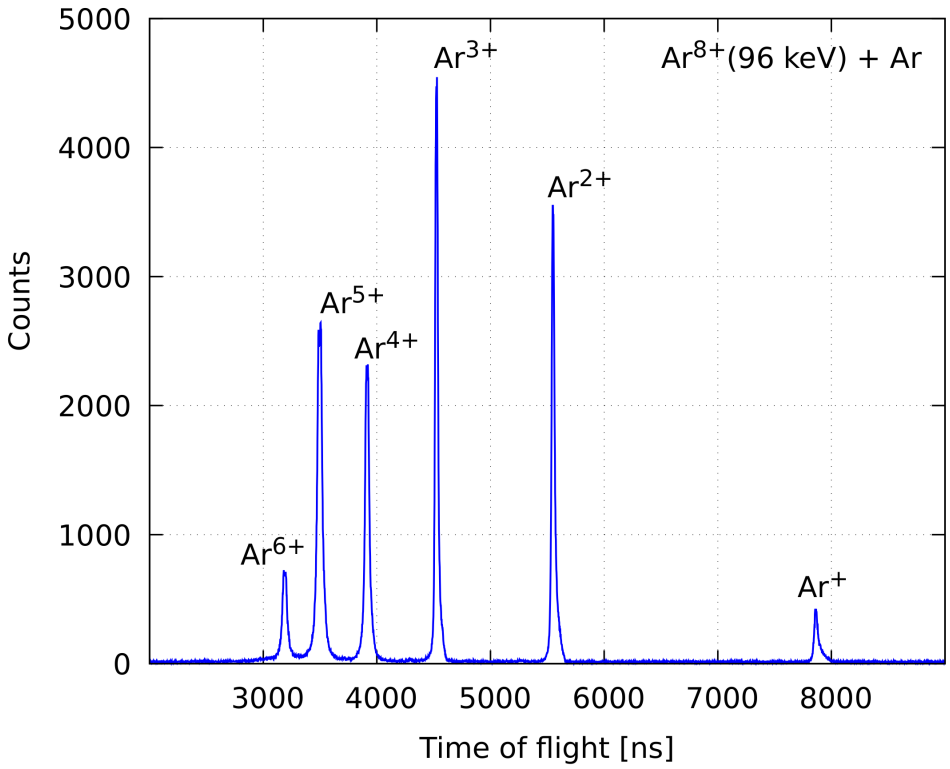


Figure 2.11: Experimentally observed Time-of-flight (ToF) spectrum under the impact of $Ar^{8+}$ ion at 96 keV on Ar target atom.

mous flexibility of ROOT makes it more suitable for offline analysis. A simple code is written to inter-convert the file formats of Cobold and ROOT.

### 2.5.1 Calibration of ion ToF spectrum

Before stepping into the detailed experimental analysis, the first step is to calibrate the ToF spectrometer with an atomic target of known mass. The calibration curve will give the relation between the ToF and $m/q$ of ions that helps in the identification of observed fragment ions in various experiments. For calibration, molecular gases are less suited because they produce fragments with high kinetic energy and few multiply ionized parent molecular ion. Instead, for calibration Ar is used. Fig. 2.11 shows the experimental ToF spectrum obtained by the ionization of argon (Ar) target gas under the impact of $Ar^{8+}$ projectile ion at 96 keV energy. The ion beam is delivered from EBIS. By simulation of IMS or by simple calculation of Eqn. 2.10, one can estimate the mean values of ToF ($t_0$) beforehand for various Ar-ions. Fig. 2.11 shows the ToF distribution of different recoil argon ions up to $Ar^{6+}$. The centroid of each distribution provides $t_0$ value of corresponding Ar-ion, and by fitting these

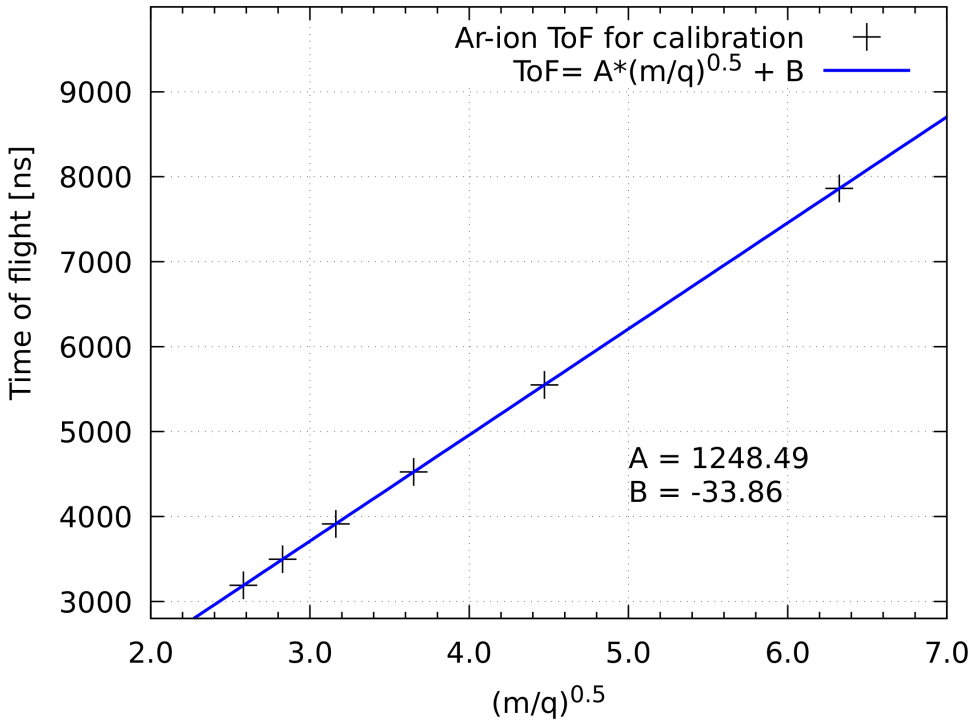


Figure 2.12: ToF Calibration curve for IMS obtained with Ar target is displayed. The ToF values on its $y$-axis are the centroid values of various Ar-ions ToF distribution shown in Fig. 2.11. The values of fitted slopes and intercepts are also labeled in the figure. The uncertainty in ToF, based on the width of ToF distribution, smaller than the symbol size. Fitting $R^2$ value is nearly one.

$t_0$ values gives the calibrated equation of the spectrometer.

Fig. 2.12 displays the calibration curve of spectrometer. The applied extraction field $E_s$ in spectrometer is 60 V/cm. The calibrated equation is given by

$$t_0(\text{ns}) = 1248.49 \times \sqrt{m/q} - 33.86 \tag{2.16}$$

The obtained value of slope A depends on the geometry of the spectrometer and field $E_s$ (Eqn. 2.10). The value of intercept B should ideally be zero. However, in real practice, the situation deviates from the ideal condition due to uncertainties in the applied extraction field and length of various IMS regions, and signals processing delays. Having calibrated equation, any unknown ion mass peak in the ToF spectrum can be identified. Moreover, having ToF spectrum, the mass resolving power of the spectrometer can be determined (see Eqn. 2.11). So far, the best value of $m/\Delta m$ has been observed to be 436. It means that nearby masses 435 amu (atomic mass unit) and 437 amu can be separated from mass 436 amu. The mass resolving

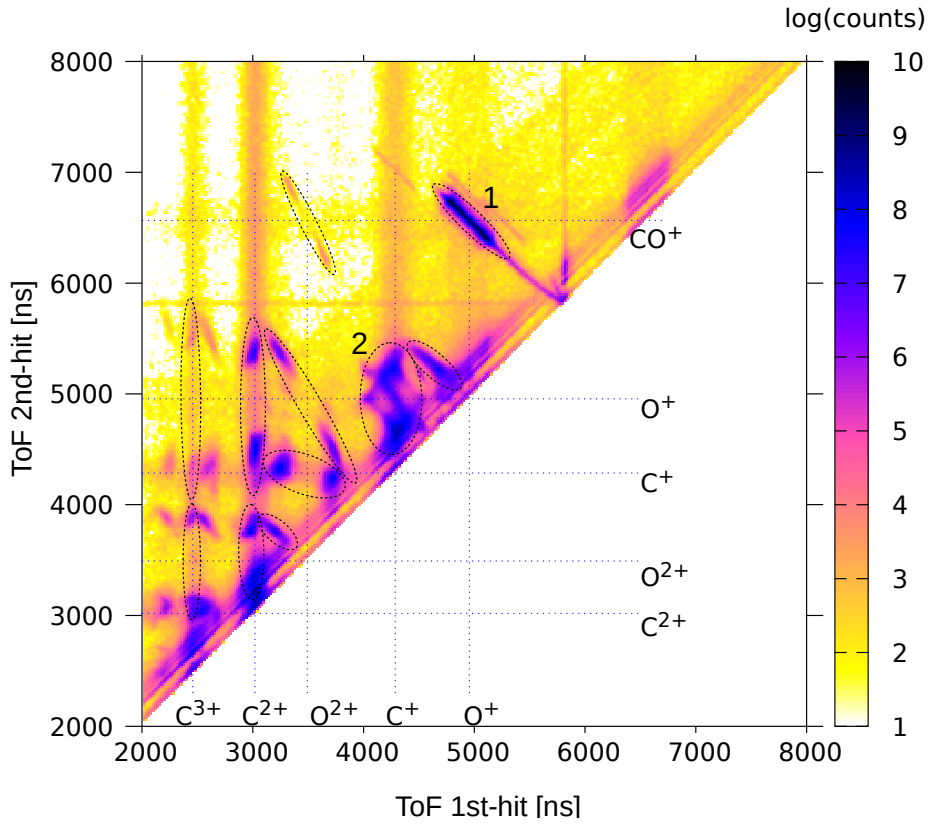


Figure 2.13: Experimentally obtained Time-of-flight coincidence map between 1st-hit and 2nd-hit observed upon the dissociation of various molecular ions of $CO_2$ formed under the impact of $Ar^{8+}$ ion at 96 keV energy on $CO_2$ molecule. Various characteristics islands are shown by ovals resulting from different dissociation channels. (See the text for more details)

power depends on many parameters. It strongly depends on the spatial spread of projectile and target overlap. It also depends on the initial kinetic energy width of formed ions and initial thermal spread of target ensemble. Suppressing the effect of initial energy spread on the ToF is not relevant to the present spectrometer as its primary aim is to measure initial kinetic energy.

### 2.5.2 Time of flight coincidence map

Previously, we looked at the calibration of the spectrometer and derived a calibration equation to identify unknown ion mass peaks observed in the ion-molecule collisions. But how to ascertain the dissociation channel from where the ions are emanating? For example, different molecular ions $CO_2^{n+}$ can dissociate via various dissociation

channels,

$$CO_2^{2+} \rightarrow O^+ + CO^+ \tag{2.17}$$

$$CO_2^{3+} \rightarrow O^+ + C^+ + O^+ \tag{2.18}$$

$$CO_2^{4+} \rightarrow O^{2+} + C^+ + O^+ \tag{2.19}$$

It can be seen that $O^+$ originates from the dissociation of $CO_2^{2+}$, $CO_2^{3+}$, $CO_2^{4+}$, and many other such possibilities can exist. However, the various fragment ions arising from a given channel will be recorded as 1st-hit, 2nd-hit, 3rd-hit and so on, according to their $m/q$ ratio (see Fig. 2.10). If two fragments arise from the same dissociation channel, their time of arrival on the detector, i.e. ToF, would be correlated because of momentum conservation. Therefore, such correlation would reflect as distinct islands in the ToF coincidence map, shown in Fig. 2.13. A ToF coincidence map is a two-dimensional graphical representation of ToF of two different hits. In Fig. 2.13, the ToF of the 1st-hit and 2nd-hit are plotted along the $x$-axis and $y$-axis, respectively. Since the ToF of 2nd-hit is always larger than that of 1st-hit, the lower half of the map is empty. Several characteristic islands corresponding to different dissociation channels can be seen. For instance: island-1 ($O^+$:$CO^+$) arises from two-body breakup channel Eqn. 2.17, and island-2 ($C^+$:$O^+$) could be either from channels Eqn. 2.18, Eqn. 2.19 or from some other channels of different transient molecular ions. Identifying a dissociation channel comprising three fragments requires a similar coincidence map between the 2nd-hit and 3rd-hit as well.

It can also be observed that the shape and slope of the various islands are not same. This is a manifestation of different underlying dissociation processes. There are mainly two types of dissociation processes: concerted and sequential process. In a concerted process (Eqn. 2.20), all bonds of the molecular ion break simultaneously, and the fragment ions move apart due to their Coulomb repulsion. In the other extreme process of sequential or stepwise dissociation (Eqn. 2.21), the molecular ion first separates into two ionic fragments (at least one fragment should be a molecular ion) and, after some time (tens of femtosecond) when they hardly interact with each

other, the second step of dissociation occurs.

$$CO_2^{3+} \rightarrow O^+ + C^+ + O^+ \tag{2.20}$$

$$CO_2^{3+} \rightarrow O^+ + CO^{2+} \rightarrow O^+ + C^+ + O^+ \tag{2.21}$$

In case of a two-body break up (island-1), both fragments fly back to back in centre of mass frame of the parent ion, and their ToF would be anti-correlated. The corresponding island will appear as a bar with the slope of $-q_2/q_1$. In a sequential process, the intermediate molecular ion can rotate before the second step of dissociation. For such a breakup ToF of ions is not exactly anti-correlated, and the shape of islands can be very different from a simple narrow bar as observed for the two-body breakup. More details about the different shapes of islands are well described in [96].

### 2.5.3 Momentum calculation

The dissociation channels of interest are selected by picking up events from the corresponding islands in a coincidence map. The events from a specific island can be separated by making a polygon cut over it. Having $(t, x, y)$ information, the momentum components of fragment ions arising from a particular dissociation channel are determined using Eqn. 2.13. Knowing the momentum information, various kinematic properties of molecular ion dissociation can be investigated.

#### Newton Diagram

A Newton diagram represents correlated momenta of fragment ions in the molecular frame of reference. Generally, in this diagram, the momentum vector of one fragment is fixed along the $x$-axis, and the relative momenta of other fragments, coming from the same dissociation channel, are plotted along the $y$-axis. It can be understood that for a two-body breakup, both fragments will go back to back in their centre of mass (CM) frame and therefore, they will appear along the same $x$-axis but on the opposite quadrant of the plot. In the case of a three-body breakup, the momentum distributions are best illustrated in a Newton diagram, providing rich information at a glance. Fig. 2.14 shows a Newton diagram in the three-body breakup of $CO_2^{3+}$ via

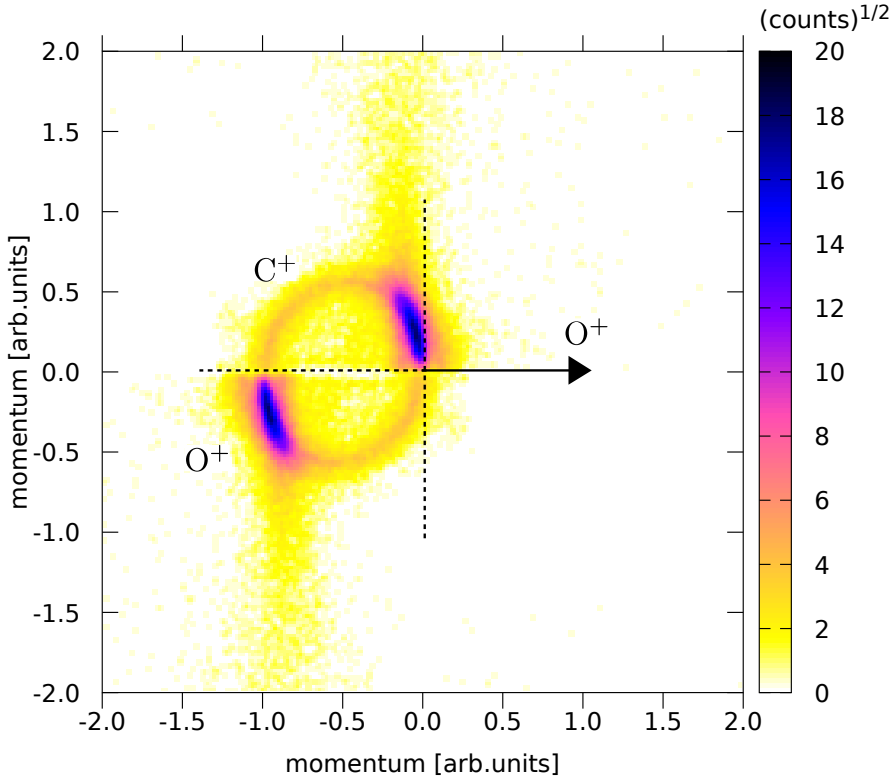


Figure 2.14: Experimentally obtained Newton diagram of $CO_2^{3+}$, under $Ar^{8+}$ impact at 96 keV energy, dissociating into $O^+$:$C^+$:$O^+$ channel. The momentum vector of one of the $O^+$ ions is fixed along the $x$-axis at 1 arbitrary unit shown by an arrow, and relative momentum vectors of $C^+$ and other $O^+$ ion are mapped in the upper and the lower half of the plot, respectively.

$O^+$:$C^+$:$O^+$ (1,1,1) channel. The momentum vector of one of the $O^+$ ions is shown by an arrow, scaled arbitrarily to unity event by event of $CO_2^{3+}$ dissociation into (1,1,1) channel. The relative momentum vectors of $C^+$ ion and the second $O^+$ ion are mapped in the upper and the lower half of the plot, respectively.

The Newton diagram can describe the geometry of transient molecular ion at the time of breakup [97], and also illustrate the underlying dissociation mechanisms [76]. In Fig. 2.14, two types of structures can be observed: one is left shifted circular structure and the other is an intense crescent like structure, which partially overlaps with some portions of the circle. The intense crescent like structure is attributed to the concerted process in which both bonds C=O of $CO_2^{3+}$ breaks simultaneously. In this case, most of the momentum is shared equally between both terminal $O^+$ ions, and $C^+$ ion carries away a very small part of the total momentum in the CM frame. The fragmenting $O^+$ ions depart at an angle less than 180°. These set of

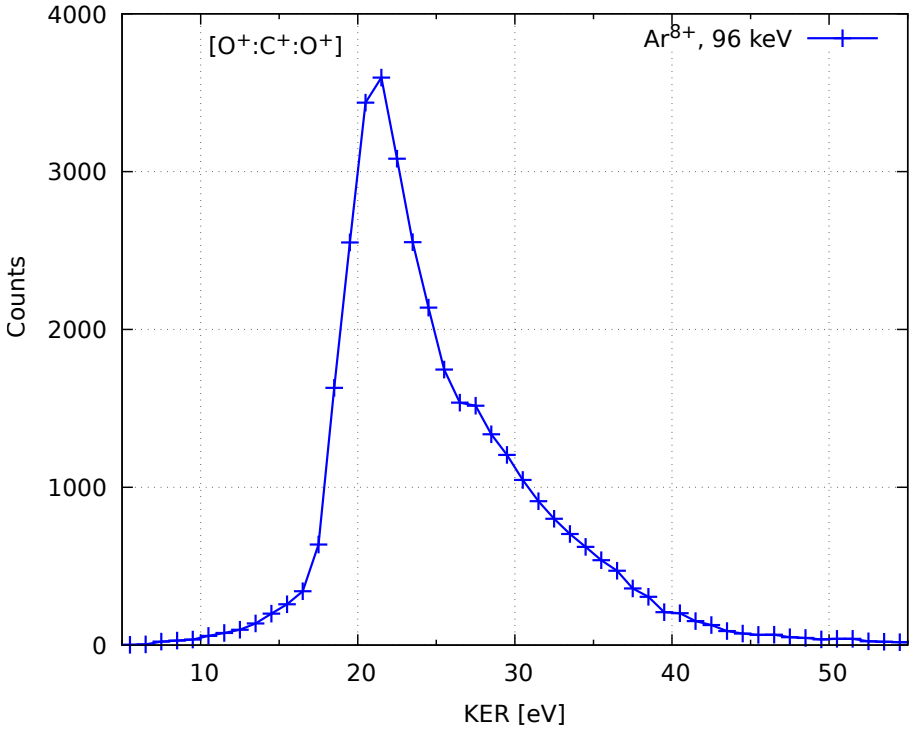


Figure 2.15: An experimentally observed kinetic energy release (KER) distribution upon the dissociation of $CO_2^{3+}$ into $O^+$:$C^+$:$O^+$ channel.

events, with the $C^+$ vector lying close to the origin correspond to the most probable geometry of $CO_2$ molecule with bond angle of 172° [98]. The spread in the $C^+$ ion momentum near the intense centre region represents the bending configuration of $CO_2$ in which $C^+$ ion gains some momentum. The other shifted circular structure corresponds to sequential dissociation. In this process, the intermediate molecular ion $CO^{2+}$ rotates before dissociation in the second step of the sequential process (Eqn. 2.21). The breakup of rotating $CO^{2+}$ ion results in a circular structure in the Newton diagram.

### Kinetic energy release

The kinetic energy release (KER) is one of the most important parameters required to understand the dynamics of the molecular dissociation process. When an external perturbation excites the molecule to an unstable state, it dissociates into two or more fragments. The fragments gain kinetic energy depending on the nature of potential energy curve or surface of the excited molecule. The sum of the ki-

netic energies of all fragments in a given dissociation channel is defined as kinetic energy release (KER). We evaluate the kinetic energy (KE) of fragment ions from the experimentally determined momentum components $(p_x, p_y, p_z)$ of the ion, where $\mathrm{KE} = (p_x^2 + p_y^2 + p_z^2)/2m$. The correlated momenta of all fragments observed in the dissociation process give the correlated kinetic energy information of the fragment ions.

It is important to realize that the KER value is decided by the nature of participating PEC or PES of dissociating molecular ions. Suppose the interaction time of the projectile with the target molecule is much shorter than the molecule's typical vibrational and rotational time scales. In that case, the excitation is represented by a vertical transition known as the Franck-Condon transition. In such excitations, the KER of the fragments directly reflects the properties of the dissociative state of the multiply ionized molecular ion (see Fig. 1.2). The KER value is equal to the difference of internal energies of the molecular ion at equilibrium position $R_0$ and asymptotic limit. Generally, the asymptotic limit is taken as five to eight times of molecule bond size in PEC calculation. It can be understood that the PEC with a steeper slope will tend to yield a higher value of KER. In case of perturbation created by the ionic projectile, for which the energy deposited is not a definite value for all collisions, a set of electronic states in the PEC diagram gets populated. The dissociation of molecular ion via these states gives a distribution of KER values instead of a single value. Fig. 2.15 shows an experimental KER distribution of $CO_2^{3+}$ ion dissociating into (1,1,1) channel. It ranges from 10 to 45 eV with a dominant feature peaked at 21 eV. The range of KER depends on the nature and the number of PECs contributing to dissociation. At the same time, the intensities of different features are governed by the probability of populating specific PECs owing to external perturbation.

Thus, the KER distribution proves to be an important parameter to investigate the dissociation dynamics of multiply ionized molecular ions. More precise inferences can be made with the help of KER distribution if theoretical PECs are known.

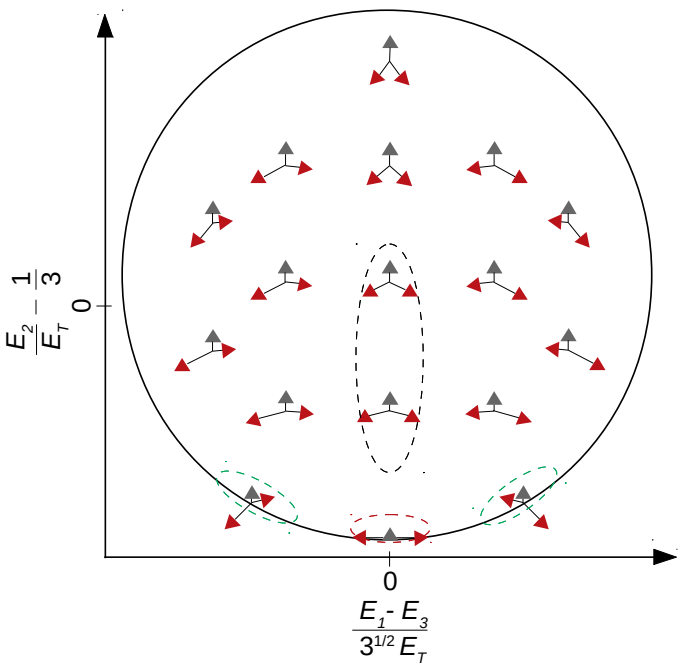


Figure 2.16: Schematic diagram of Dalitz plot for a triatomic molecule. (See the texts for more details)

### Dalitz plot

A Dalitz plot is a representation of correlated momenta of fragments in terms of their reduced kinetic energies [99]. It permits us to visualize the conformation of transient molecular ions in great detail. The $x$ and $y$ coordinates of the Dalitz plot for a triatomic molecule are given by,

$$x = \frac{E_3 - E_1}{3^{1/2} E_T}, \qquad y = \frac{E_2}{E_1} - \frac{1}{3} \tag{2.22}$$

where $E_i$ ($i = 1, 2, 3$) are the kinetic energies of the three fragments, and $E_T$ is the total kinetic energy release (KER), $E_1 + E_2 + E_3$ upon dissociation. Essentially, in a three-body Dalitz plot, the kinetic energies of two of the three fragments are chosen as coordinates, and the third is fixed by the energy sum normalization. A random breakup will lead to a uniform event density in the kinematically allowed region of this plot. The two dimensionless generalized coordinates $x$, $y$ basically describe the sharing of total energy $E_T$ among the fragments. The detailed calculation to obtain the appropriate coordinates (Eqn. 2.22) can be found in [100]. Each region of this 2D plot refers to a certain geometry of the momentum vectors at the time of breakup; a schematic for few points is shown in Fig. 2.16. For example, the

red, black and green ovals represent the molecule's linear, bending and asymmetric stretch geometry at the time of the breakup, respectively. With the help of a Dalitz plot, the bond breaking mechanisms like concerted and sequential processes can be separated efficiently [76].

In summary, we have a combination of a multi-particle momentum spectrometer and data extraction and mapping techniques, which will serve as tools for studying the dissociation dynamics of multiply ionized molecular ions. The results of our studies are presented in chapters 3 and 4. It is important to note that in the description so far, we have not concerned ourselves with the process of ionization itself. The molecular ion may be formed by a variety of processes with the same projectile. For separating the processes, we need additional experimental capabilities, which will be presented in chapter 5. The results from this added feature will be presented in chapter 6.

# Chapter 3

# Dissociation dynamics of molecular ion created under slow highly charged ions impact

## 3.1 Introduction

In HCI impact, the multiple ionization of the molecule can occur via different ionization processes like direct ionization, capture ionization, and capture followed by autoionization of the target. However, in a slow ($v < 1$ a.u.) impact regime, HCI ionizes the target via pure capture or capture followed by autoionization of the target more dominantly, and the cross section of these processes mainly depends on the projectile charge state [60, 101]. In their calculation, Simics *et al.* have reported that the cross section of single, double and triple capture processes increases with the projectile charge [101]. In interactions between the projectile ion and molecule, the molecular ion can be formed in any of its excited states, and the nature of the excited states governs the fate of the so-formed molecular ion. If the excited state is unstable, the molecular ion dissociates into its fragments. The formation of a given dissociative molecular ion under the impact of a projectile of different charge states can involve the population of its different excited states, which may result in the different dissociation dynamics of the molecular ion.

This chapter aims to address the question of how the projectile charge $q$ affects the kinematics of dissociating multiply ionized molecular ions. To investigate this,

a series of experiments, under the impact of $Ar^{q+}$ ions (where $8 \leq q \leq 14$) at 96 keV energy ($v$ = 0.3 a.u.) on a simple triatomic molecule $CO_2$, are performed. The investigation of $CO_2^{4+}$ molecular ion into three ionic fragments via two dissociation channels $O^+$+$C^{2+}$+$O^+$ and $O^{2+}$+$C^+$+$O^+$ is presented.

## 3.2 Experimental details

The experimental setup used in this work is already discussed in the previous chapter in detail (Fig. 2.6). The ion beam of $Ar^{q+}$ (where $8 \leq q \leq 14$, 96 keV energy) overlaps with the effusive jet of target molecule $CO_2$ in collision chamber the IMS. The low ion beam current, of the order of 10−15 pA, and low gas pressure (2–5×$10^{-7}$ mbar) are maintained to keep accidental coincidences at a lower rate. The fragment ions are guided towards the detector by a uniform electric field of strength 60 V/cm. The ion time-of-flight measurement is triggered by coincidence with the ejected electrons. The time-of-flight ($t$) and arrival positions $(x, y)$ information is mapped one to one to the momentum components $p_z$ and $p_x, p_y$ of the fragments. From this information, the kinetic energy of all ionic fragments is derived. In this experiment, an extraction field of 60 V/cm has been applied and the achieved resolution of the total kinetic energy release is ≈ 1.0 eV.

## 3.3 Results and discussion

### 3.3.1 Observed molecular ions

In the present collision experiment, various molecular ions are formed, which can be identified with the help of ToF coincidence map. Fig. 3.1 shows the ToF coincidence maps observed under the impact of projectile $Ar^{12+}$ at the energy of 96 keV. In this map, ovals are drawn which identify various islands formed through the dissociation of $CO_2^{3+}$ and $CO_2^{4+}$ molecular ions, as follows

$$CO_2{}^{3+} \rightarrow O^+ + C^+ + O^+ \qquad (1,1,1) \tag{3.1}$$

$$CO_2{}^{4+} \rightarrow O^+ + C^{2+} + O^+ \qquad (1,2,1) \tag{3.2}$$

$$CO_2{}^{4+} \rightarrow O^{2+} + C^+ + O^+ \qquad (2,1,1) \tag{3.3}$$

The abbreviation in parenthesis represents the order of charge state of fragments keeping carbon ion at centre. The continuous black ovals are observed due to dissociation of $CO_2^{3+}$ into $O^+$+$C^+$+$O^+$ [(1,1,1) channel]. The dotted black and red ovals correspond to $O^+$+$C^{2+}$+$O^+$ [(1,2,1) channel] and $O^{2+}$+$C^+$+$O^+$ [(2,1,1) channel] dissociation channels of $CO_2^{4+}$, respectively. Similarly, dissociation channels of other precursor molecular ions up to $CO_2^{6+}$ can be identified in the present coincidence map. However, their statistics are comparatively low.

In the past, $CO_2^{3+}$ dissociating into (1,1,1) channel has been the most extensively studied molecular ion under impact of a variety of projectiles viz electron, HCIs, laser and synchrotron radiation. For the present investigation of the effect of the projectile charge on the dissociation dynamics of multiply ionized molecular ion, we have chosen comparatively lesser studied molecular ion $CO_2^{4+}$. Moreover, $CO_2^{4+}$ is suitable for our investigation because it provides two three-body dissociation channels to study. Other observed molecular ions $CO_2^{5+}$ and $CO_2^{6+}$ can also lead to the various three-body dissociation channels. However, as the degree of ionization of transient molecular ions increases, their potential energy curves (PEC) become more steeper. Dissociation of such molecular ion follows almost purely Coulomb explosion, showing negligible dependence on the type of projectiles.

### 3.3.2 Kinetic energy release distributions

The experimental KER distributions of the (1,2,1) and (2,1,1) dissociation channels under the action of different $Ar^{q+}$ ($8 \leq q \leq 14$) projectile ions at same energy of 96 keV are shown in Fig. 3.2. It can be observed that the KER distribution of the (1,2,1) channel ranges from 30 to 80 eV and that of the (2,1,1) channel ranges from 25 to 90 eV. There are significant differences in the KER distributions of the two channels. The two dominant features in both channels are around 39 eV and around 52 eV. Our KER distributions are quite different from the previous results on dissociation, reported by Siegmann *et al* using swift HCI [62]. For both channels they have reported broad KER distributions extending from 25 eV to 100 eV with peak values around 57 eV (for channel (1,2,1)) and around 62 eV (for channel (2,1,1)) and lacking a finer structure. They also observed that experimental KER spectra of these two channels are quite similar to each other, which is contrary to our findings.

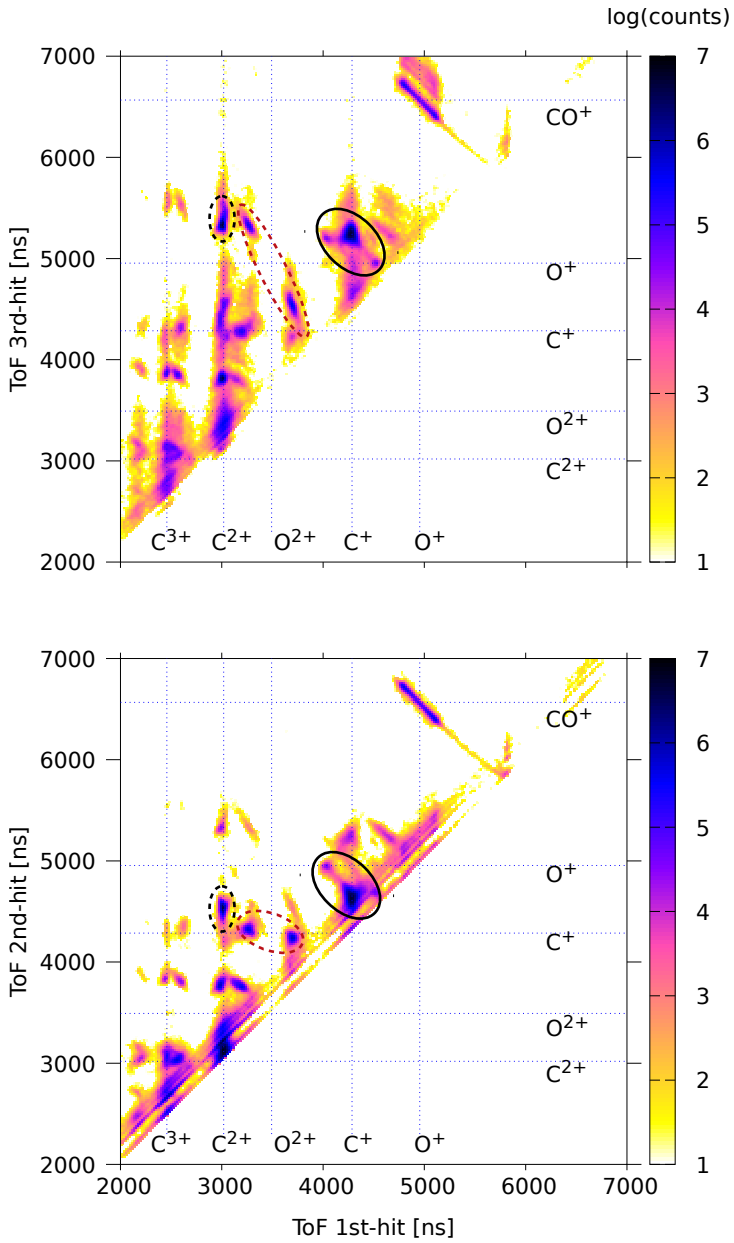


Figure 3.1: Time-of-flight coincidence map observed under the impact of $Ar^{12+}$ ion on $CO_2$ at an energy of 96 keV. Islands corresponding to dissociation channels $O^+$+$C^+$+$O^+$ (continuous black ovals), $O^+$+$C^{2+}$+$O^+$ (dotted black ovals) and $O^{2+}$+$C^+$+$O^+$ (dotted red ovals) are marked. Other islands appear in the lower side of ToF arise from dissociation of molecular ions of higher degree of ionization.

Wang *et al.* under electron impact reported some structures in KER distributions of both channels [33]. They observed a sharp peak at ≈ 42.5 eV with a wide lobe at ≈ 54 eV in (1,2,1) channel and a weak peak at ≈ 43 eV with a lobe at ≈ 51 eV in (2,1,1) channel. However, statistics were very low in these channels because of the low cross section for the formation of $CO_2^{4+}$ in electron impact.

In Fig. 3.2, interestingly, it can be seen that the relative intensities of two domi-

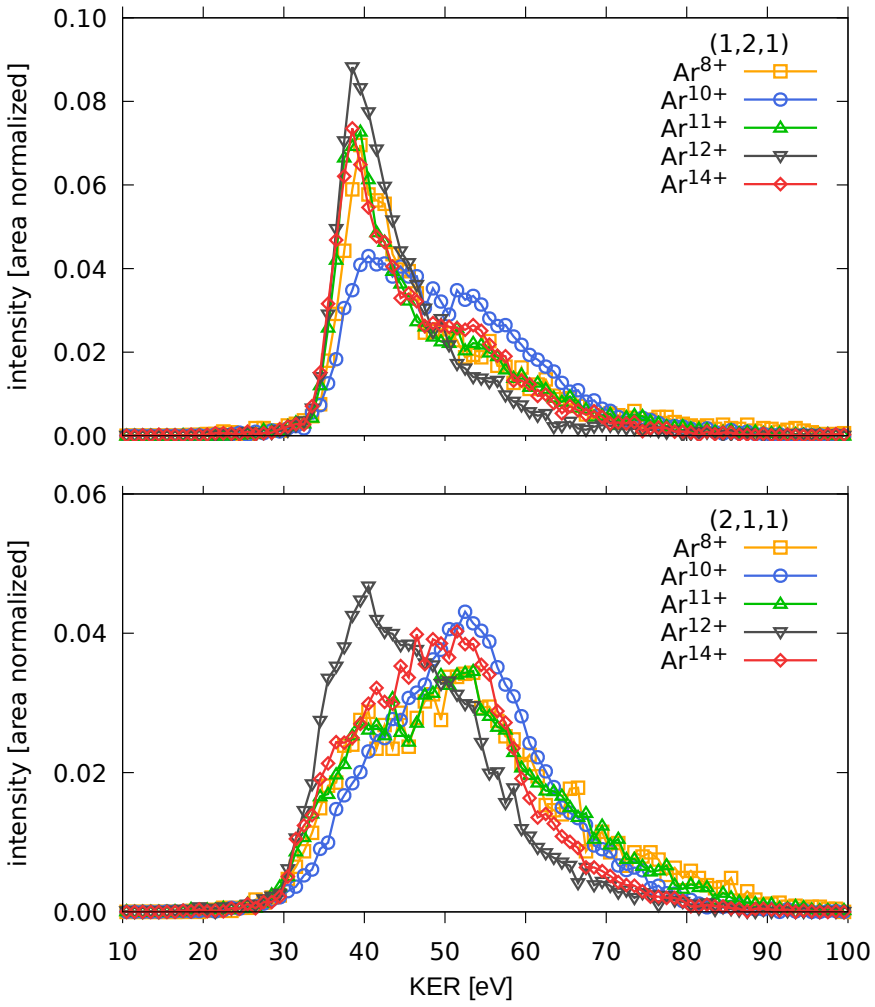


Figure 3.2: Total kinetic energy release (KER) distributions resulting from collisions with different $Ar^{q+}$ ions at an energy of 96 keV. [Top] $O^+$:$C^{2+}$:$O^+$ (1,2,1) dissociation and [Bottom] $O^{2+}$:$C^+$:$O^+$ (2,1,1) dissociation. Areas under the curves are normalized to unity.

nant structures at 39 eV and around 52 eV are strongly influenced by the projectile charge in both channels. For example, for the (1,2,1) channel, the structure around 52 eV is enhanced in the case of $Ar^{10+}$ impact (blue curve), while in the case $Ar^{12+}$ impact (black curve) the same feature is suppressed. For the (2,1,1) channel, $Ar^{12+}$ impact (black curve) results in an enhanced relative intensity of the structure appearing around 39 eV in the KER distribution. Apart from these two readily observed peaks, there are also some other structures in KER distributions. To identify these and participating electronic states of $CO_2^{4+}$, the potential energy curves (PEC) of $CO_2^{4+}$ are calculated.

### 3.3.3 Identification of different electronic states of $CO_2^{4+}$

#### Calculation of PEC

In order to identify the participating states in dissociation of $CO_2^{4+}$ into the (1,2,1) and (2,1,1) channels, PEC of the several excited states of $CO_2^{4+}$ leading to $O^+ + C^{2+} + O^+$ and $O^{2+} + C^+ + O^+$ dissociation has been calculated through *ab initio* calculations using GAMESS [102] suite of programs[1]. Fig. 3.3 shows the obtained PEC. The Multi-Configuration (MC) Self-Consistent Field (SCF) method [103] along with Configuration Interaction (CI) has been used to obtain the PECs of the excited states. The electronic configuration of the neutral $CO_2$ ($\Sigma^{1+}$) is $(1\sigma_u)^2(1\sigma_g)^2(2\sigma_g)^2(3\sigma_g)^2(2\sigma_u)^2(4\sigma_g)^2(3\sigma_u)^2(1\pi_u)^4(1\pi_g)^4$. In the MCSCF-CI calculation, the inner five MOs are considered as a core orbital and the rest of the orbitals

[1]Calculation is done by Arnab Sen, IISER Pune.

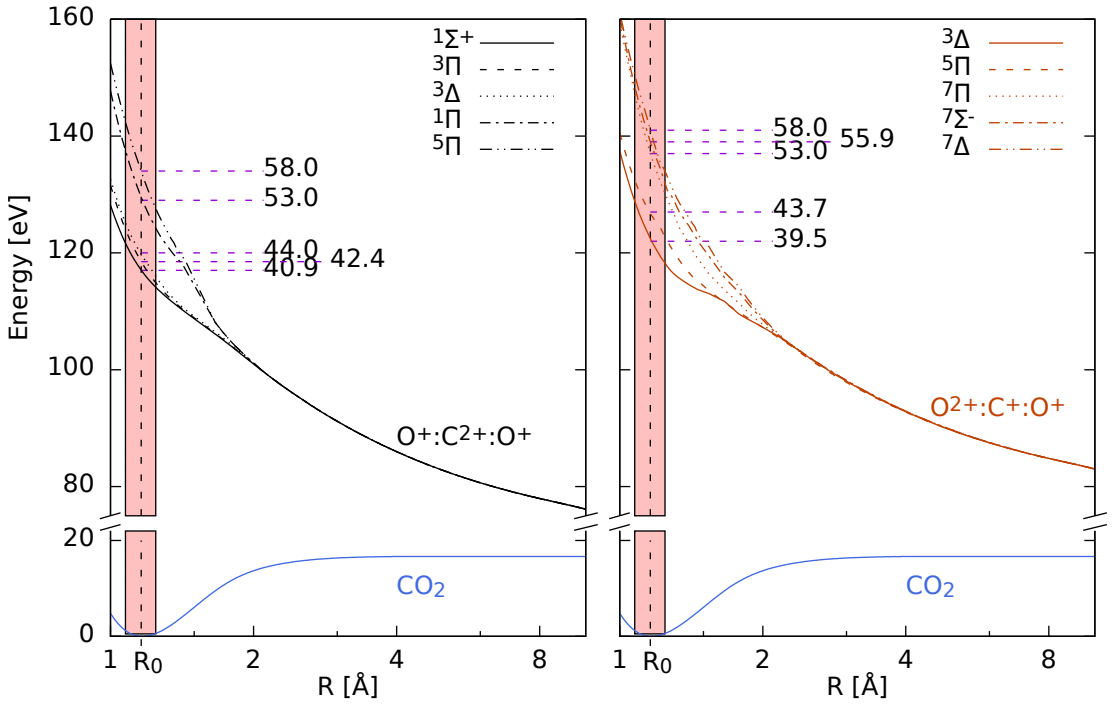


Figure 3.3: Potential energy curves of $CO_2^{4+}$ calculated using the 6311-G type basis set. Curves contributing to the (1,2,1) and (2,1,1) dissociation channels are shown in the left and right panels, respectively. The separated atoms limits are $O^+(^4S), C^{2+}(^1S), O^+(^4S)$ and $O^{2+}(^3P), C^+(^2P), O^+(^4S)$, respectively. The vertical strip represents the Franck–Condon region. Numbers shown adjacent to the upper curves are the expected values of the kinetic energy release, in eV, resulting from excitation to the respective curves.

along with four virtual orbitals are taken as active orbitals with eight active electrons for $CO_2^{4+}$ ion. The density convergence criterion for this calculation has been set at $10^{-6}$ to obtain well converged virtual orbitals. For the (2,1,1) dissociation limit the MCSCF calculation is carried out with point group symmetry $C_1$, where the two oxygen atoms are no more equivalent to each other. However, for the (1,2,1) channel the point group symmetry is taken to be $D_{2h}$, as it enforces the two oxygen atoms to be identical. We have assumed symmetric stretch of the O–C–O bond from its equilibrium bond length of $\approx$ 1.16 Å up to $\approx$ 10 Å with a step size of 0.02 Å and the energy of the excited states at each step are noted to get the entire PEC. In this case, three different basis sets (*i*) split valence double zeta basis, (*ii*) Pople's "triple split" 6311-G basis set and (*iii*) Dunning type correlation consistent basis sets augmented with a set of diffuse function: aug-cc-pVTZ are used to make sure that the calculated PECs are independent of basis set.

**Fitting of KER distributions**

With the help of PEC, KER distributions of both channels corresponding to different $Ar^{q+}$ ions have been fitted to the sum of multiple Gaussian functions. To obtain the initial parameters for the fit, we take the Franck–Condon region to be $\pm 2\sigma$ of the probability density of the ground vibrational state of $CO_2$ and project this width on to the PEC of upper electronic states (shown in Fig. 3.3). The projected width is taken to be equal to $\pm 1.5\sigma$ for the KER distribution. The width of the Gaussian function corresponding to each upper state is fixed in this manner, and is not a fitting parameter, while the amplitudes and centroids of the Gaussians are determined by a least squares fit of the sum of multiple Gaussians to the experimental KER distributions. Fig. 3.4 shows the experimental KER distribution and the multiple Gaussian fit for both dissociation channels in the case of $Ar^{10+}$ impact. Consistency of the fit has been checked by varying the standard deviation values by ± 10%.

The values of the centroids obtained by fitting are listed in Table 3.1 for the two dissociation channels for all projectiles. These values are compared with the KER values estimated from the PEC for different states, which are also mentioned in the table. A fair agreement is seen between the fitted values of KER and those estimated from the PECs, and this permits us to match the features in the experimental KER

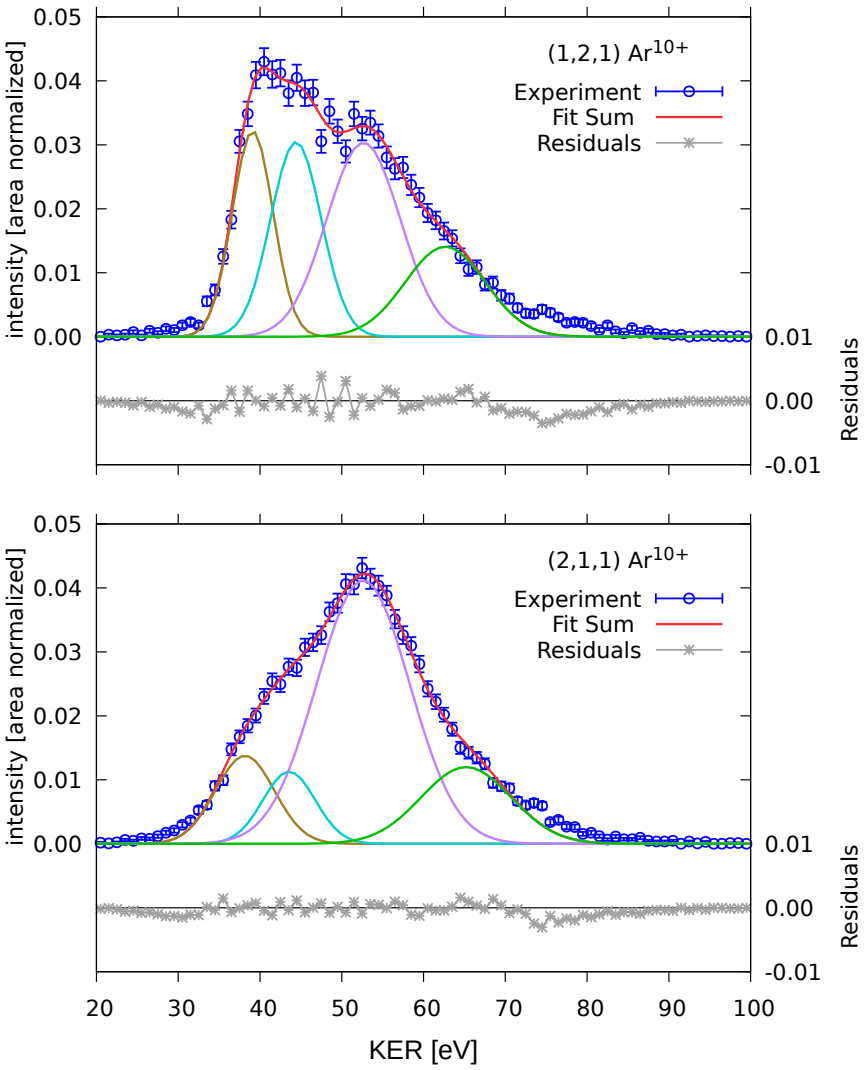


Figure 3.4: Fitting of multiple Gaussian curves (normalized to total counts) to experimental KER distributions for $Ar^{10+}$ ion impact at 96 keV for the (1,2,1) and (2,1,1) dissociation channels. Error bars on the experimental data show statistical errors. Fit residuals are shown at the bottom of each graph.

distributions with the participating excited states. We observe, in Table 3.1, that the values of the centroids do not vary much with the projectile charge, except in two instances in channel (1,2,1). For the $^1\Pi$ excitation, the PEC-based estimate matches the fitted centroids for all projectiles, except $Ar^{12+}$, for which the fitted value is lower. On the other hand, for the $^5\Pi$ excitation, the PEC-based estimate matches the fitted centroid for $Ar^{12+}$, but the centroids for all other projectiles are higher. As seen from Fig. 3.2, in the KER distribution beyond approximately 50 eV ($^1\Pi$ excitation), the tail is longer for projectiles other than $Ar^{12+}$. Since the fit to the KER distribution is a multipeak fit with peak widths fixed by the Franck-Condon

| Predicted | | Centroids of peaks fitted to experimental data | | | | |
|---|---|---|---|---|---|---|
| State and KER | | $Ar^{8+}$ | $Ar^{10+}$ | $Ar^{11+}$ | $Ar^{12+}$ | $Ar^{14+}$ |
| $O^+ + C^{2+} + O^+$ ((1,2,1) channel) | | | | | | |
| $^1\Sigma^+$ | $40.9 \pm 2.5$ | $39.3 \pm 0.1$ | $39.1 \pm 0.1$ | $38.7 \pm 0.1$ | $38.8 \pm 0.1$ | $38.4 \pm 0.1$ |
| $^3\Delta$ | $44.0 \pm 3.1$ | $44.5 \pm 0.4$ | $44.4 \pm 0.2$ | $44.5 \pm 0.3$ | $44.2 \pm 0.4$ | $44.3 \pm 0.2$ |
| $^1\Pi$ | $53.0 \pm 4.5$ | $52.9 \pm 0.8$ | $52.7 \pm 0.3$ | $53.3 \pm 0.5$ | $50.5 \pm 2.2$ | $53.0 \pm 0.4$ |
| $^5\Pi$ (or higher) | $58.0 \pm 4.9$ | $63.7 \pm 1.5$ | $62.7 \pm 0.5$ | $64.6 \pm 1.4$ | $59.2 \pm 4.5$ | $64.7 \pm 1.6$ |
| $O^{2+} + C^+ + O^+$ ((2,1,1) channel) | | | | | | |
| $^3\Delta$ | $39.5 \pm 3.6$ | $38.2 \pm 0.4$ | $38.2 \pm 0.4$ | $35.3 \pm 0.6$ | $36.8 \pm 0.3$ | $36.7 \pm 0.2$ |
| $^5\Pi$ | $43.7 \pm 3.2$ | $44.5 \pm 0.8$ | $43.6 \pm 0.4$ | $41.2 \pm 0.4$ | $41.6 \pm 0.5$ | $43.7 \pm 0.3$ |
| $^7\Pi$ | $53.0 \pm 5.7$ | $52.7 \pm 0.4$ | $52.6 \pm 0.1$ | $51.5 \pm 0.2$ | $49.1 \pm 0.4$ | $51.9 \pm 0.2$ |
| higher | | $67.2 \pm 0.6$ | $65.2 \pm 0.3$ | $65.9 \pm 0.4$ | $61.8 \pm 1.1$ | $65.7 \pm 1.0$ |

Table 3.1: *First two columns:* Excited states of $CO_2^{4+}$ contributing to the two observed dissociation channels and the KER values predicted from the computed PE curves and their range based on the Franck–Condon overlap. *Later five columns:* Centroids (with fitting error) of the Gaussian functions fitted to experimental KER distributions for the two break up channels for different projectiles. All values are in eV.

overlap, the dominant structure corresponding to $^1\Sigma^+$ and $^3\Delta$ excitations causes a shift of the centroids of the neighboring fit functions toward a lower value. For similar reasons, the prominent tail at higher KER for projectiles other than $Ar^{12+}$ causes the fitted peaks corresponding to the $^5\Pi$ excitation for those projectiles to emerge at a higher value.

Referring to Figs. 3.2 and 3.3, thus, we see that for channel (1,2,1), the sharp peak around 39.5 eV can be attributed to dissociation of $CO_2^{4+}$ via its $^1\Sigma^+$ state. The second prominent feature at around 52.5 eV arises by dissociation via the $^1\Pi$ state, while the features at even higher KER values are due to the dissociation via $^5\Pi$ or other higher lying states. For channel (2,1,1), $CO_2^{4+}$ dissociates via $^3\Delta$ and $^7\Pi$ states, which give rise to two dominant features in the KER distribution at around 39.5 eV and around 52.0 eV, respectively. Features at higher energy, once again, could be due to higher-lying electronic states, which do not appear in our calculation.

### 3.3.4 Probability to access different electronic states

The normalized areas of the fitted Gaussian distributions (normalized to the area under the experimental KER distributions for each projectile and each dissociation

channel separately) give us the relative probabilities of the contribution of each state toward the yield of that dissociation channel. The relative probabilities are shown in Fig. 3.5. For channel (1,2,1), $^1\Sigma^+$, $^3\Delta$ and $^1\Pi$ are the main participating electronic states. Of these states, the $^3\Delta$ state is almost equally probable for all projectiles. However, the probability of accessing the $^1\Sigma^+$, $^1\Pi$ and $^5\Pi$ states is different for different $Ar^{q+}$ ions. The low-lying $^1\Sigma^+$ state is dominantly accessed in the case of $Ar^{12+}$ impact and the least in the case of $Ar^{10+}$ impact. On the other hand, higher-lying states $^1\Pi$ and $^5\Pi$ have a smaller probability in the case of $Ar^{12+}$ impact and a greater probability for $Ar^{10+}$ impact. $Ar^{11+}$ and $Ar^{14+}$ show nearly equal probability of accessing the $^1\Sigma^+$ state, which is the highest contributing state. For channel (2,1,1), Fig. 3.5 shows that $^3\Delta$ and $^7\Pi$ are the two main states that are accessed. The $^3\Delta$ state is most likely to be accessed in the case of $Ar^{12+}$ impact. On the other hand, $^7\Pi$ state is more likely to be accessed in case of $Ar^{10+}$. Furthermore, the dominant $^7\Pi$ state is almost equally probable for $Ar^{8+}$, $Ar^{11+}$, and $Ar^{12+}$ projectiles. Thus, the probability of accessing different electronic states of $CO_2^{4+}$ dissociating into (1,2,1) and (2,1,1) channels depends on the projectile charge. $Ar^{10+}$ and $Ar^{12+}$ are found to show stark differences in the probability of accessing different states, compared to other projectiles, as is also seen clearly in Fig. 3.2 (blue and black curves). For the (1,2,1) channel, the low-lying $^1\Sigma^+$ has the highest probability of being accessed for all projectiles except $Ar^{10+}$, while the $^1\Pi$ has the highest contribution in case of $Ar^{10+}$ impact. For the (2,1,1) channel, the $^7\Pi$ state has the dominant contribution for all projectiles, and especially so for $Ar^{10+}$ impact. For both dissociation channels, the average KER is lower in the case of $Ar^{12+}$ impact compared to all other projectiles.

### 3.3.5 Bond-breaking mechanisms of $CO_2^{4+}$

Previously, we have seen that how the projectile charge influences the KER distributions, and the probability to access different electronic states in dissociation of $CO_2^{4+}$ molecular ion. We also found that $Ar^{10+}$ and $Ar^{12+}$ show stark differences in the probability of accessing different states. In this section, we will focus on the dissociation mechanisms i.e. bond-breaking mechanisms of $CO_2^{4+}$, which has been visualized with the help of Newton diagram and Dalitz plot. The effects of projectile

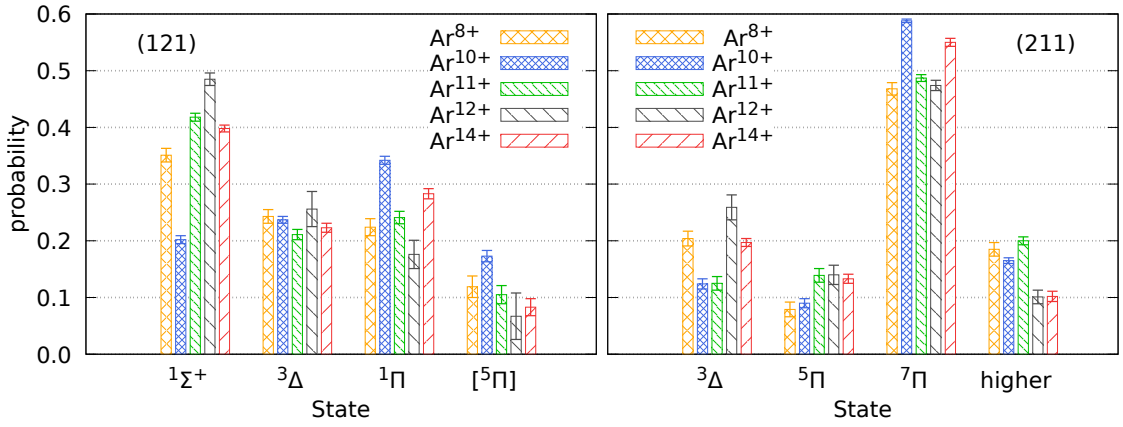


Figure 3.5: Probability of excitation to different $CO_2^{4+}$ states under the impact of different projectiles, based on the normalized area under each Gaussian function fitted to the experimental KER distribution for the two dissociation channels, (1,2,1) and (2,1,1). For the (1,2,1) channel, the state shown as $[^5\Pi]$ is to be understood as $^5\Pi$, or higher, consistent with Table 3.1.

charge, particularly of $Ar^{10+}$ and $Ar^{12+}$, on these mechanisms are also discussed.

### (I) $O^+ + C^{2+} + O^+$ dissociation channel

Fig. 3.6 shows the Newton diagrams (top), Dalitz plots (mid) and kinetic energy (KE) distribution (bottom) of all fragments for (1,2,1) channel, observed in $Ar^{10+}$ and $Ar^{12+}$ ions impact. A Newton diagram displays a clear picture of breakup process of a molecular ion. In Newton diagram, the momentum vector of one of the $O^+$ ion is defined along the $x$-axis and normalized to unit momentum. The relative momentum vectors of $C^{2+}$ ion and other $O^+$ ion are shown in the upper and lower quadrant of plot, respectively. For both Ar-ion impact, Newton diagram has dark crescent like islands, which exhibit the concerted bond-breakup of $CO_2^{4+}$ into the (1,2,1) channel. The momentum spread of $C^{2+}$ and $O(2)^+$ ions near $(0, 0)$ and $(-1, 0)$, respectively, reveals the concerted breakup of $CO_2^{4+}$ in its bending bond configuration. However, it can be noticed that for $Ar^{10+}$, the island is slightly wider than as that of $Ar^{12+}$ ion.

The $x$ and $y$ coordinates in a Dalitz plot are given by

$$x = \frac{E_1 - E_3}{3^{1/2}E_T} \qquad y = \frac{E_2}{E_T} - \frac{1}{3} \tag{3.4}$$

where $E_i (i = 1, 2, 3)$ are the kinetic energies of the three fragments and $E_T$ is total kinetic energy release, $E_T = E_1 + E_2 + E_3$. For the (1,2,1) channel, $i \equiv O^+_{(1)}, C^{2+}, O^+_{(2)}$

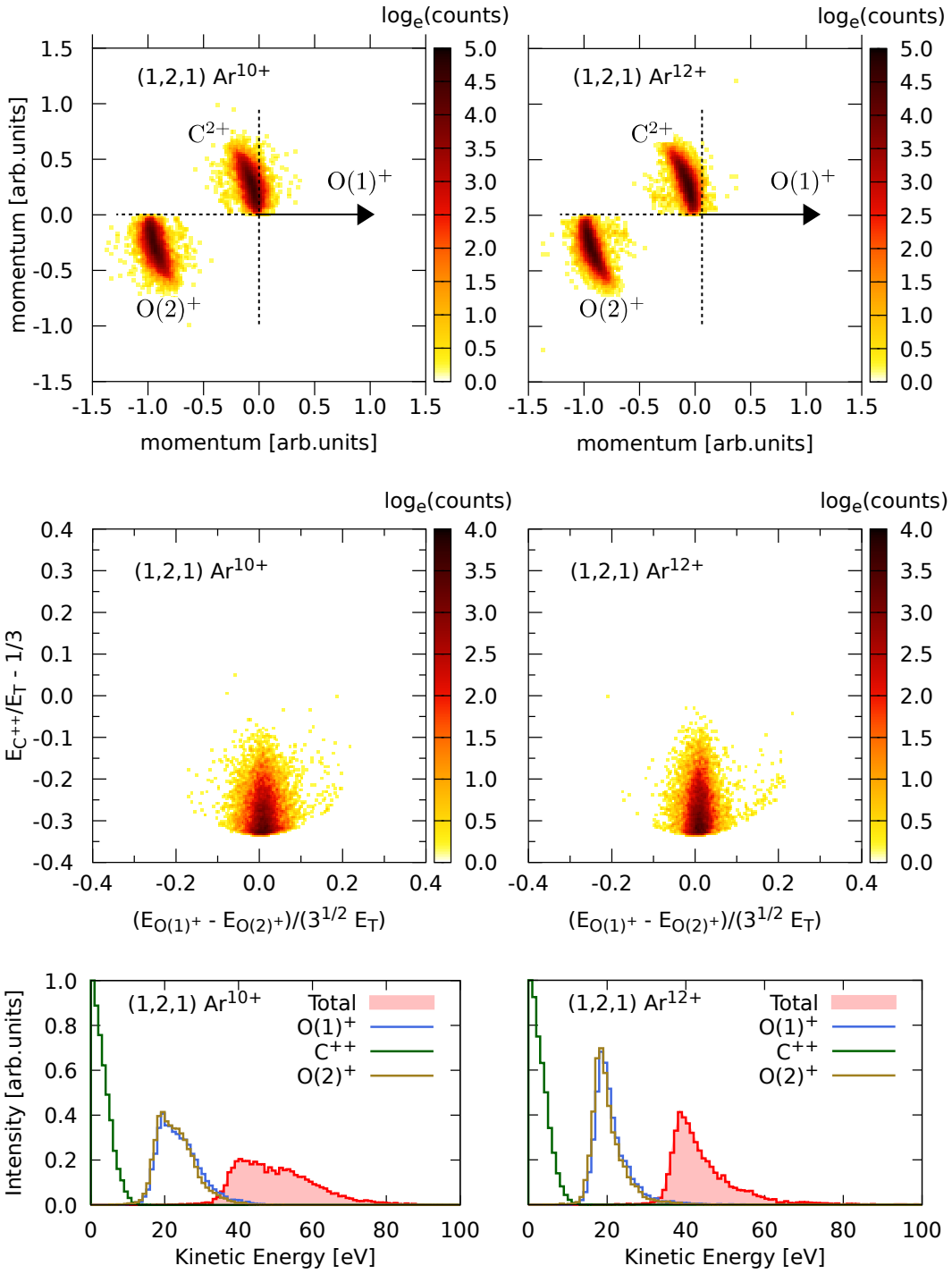


Figure 3.6: Newton diagrams (top), Dalitz plots (mid) and the kinetic energy distributions (bottom) of (1,2,1) channel for $Ar^{10+}$ and $Ar^{12+}$ impact.

and for the (2,1,1) channel $i \equiv O^{2+}, C^+, O^+$.

Fig. 3.6 (mid) shows the Dalitz plots of (1,2,1) channel for both Ar-ions. The intense region at the bottom ($x = 0, y = -0.33$) reveals that the central ion $C^{2+}$ carries very small energy and the two $O^+$ ions are emitted back to back, which is a signature

$CO_2^{4+}$ having a linear geometry. The density distribution in the Dalitz plots is on the whole symmetric about the $x = 0$ axis. This leads to the inference, that the (1,2,1) channel is due to a symmetric concerted process. The density spread above the bottom region, along the $y$-axis represents the bending configuration of $CO_2^{4+}$. In this case, $C^{2+}$ shares some part of total energy $E_T$. There are no significant differences in the Dalitz plots for the $Ar^{10+}$ and $Ar^{12+}$ projectiles, except that the spread along the $x$-axis is greater in the case of $Ar^{10+}$ than that for $Ar^{12+}$.

The energy sharing among ionic fragments ($O^+$, $C^{2+}$, $O^+$) can be understood directly from kinetic energy (KE) distributions of each fragment shown in bottom of Fig. 3.6. It is evident that $C^{2+}$ carries away very little energy, and most of the released energy is equally shared by the two $O^+$ ions, consistent with a linear, concerted dissociation. For $Ar^{12+}$ impact, $E_{O^+}$ distribution has a sharp peak at around 19 eV, however, it has wider distribution for $Ar^{10+}$ impact. This difference is reflected in the slightly wider spread of Newton diagram and Dalitz plot for $Ar^{10+}$ projectile ion.

### (II) $O^{2+} + C^+ + O^+$ dissociation channel

Fig. 3.7 shows Newton diagrams (top), Dalitz plots (mid) and kinetic energy (KE) distribution (bottom) of all fragments for (2,1,1) channel, observed in $Ar^{10+}$ and $Ar^{12+}$ ions impact. Similar to the case of (1,2,1) channel, here, Newton diagram displays the relative momentum of $C^+$ and $O^+$ ions with respect to $O^{2+}$ ion in the upper and lower part of the plot, respectively. In addition to the crescent like island, there is a circular structure in case of (2,1,1) channel for both $Ar^{10+}$ and $Ar^{12+}$ ions. The left-shifted circular structure reveals the two-step sequential dissociation of $CO_2^{4+}$ into (2,1,1) channel. In first step, $CO_2^{4+}$ dissociates into $O^{2+}$ and $CO^{2+}$ fragment ions, and after some time when they hardly interact with each other, the second step of dissociation of $CO^{2+}$ into $C^+$ and $O^+$ occurs. Before dissociation, the intermediate molecular ion $CO^{2+}$, which is moving to the left, rotates which results in a shifted circular structure in the Newton diagram. Previous reports of $CO^{2+}$ molecular ion produced by K-shell photoionization followed by Auger decay have shown that for a kinetic energy release (KER) below 10.95 eV, the $CO^{2+}$ ion decays within 30–100 fsec, which is sufficient for rotation to occur before dissociation [104].

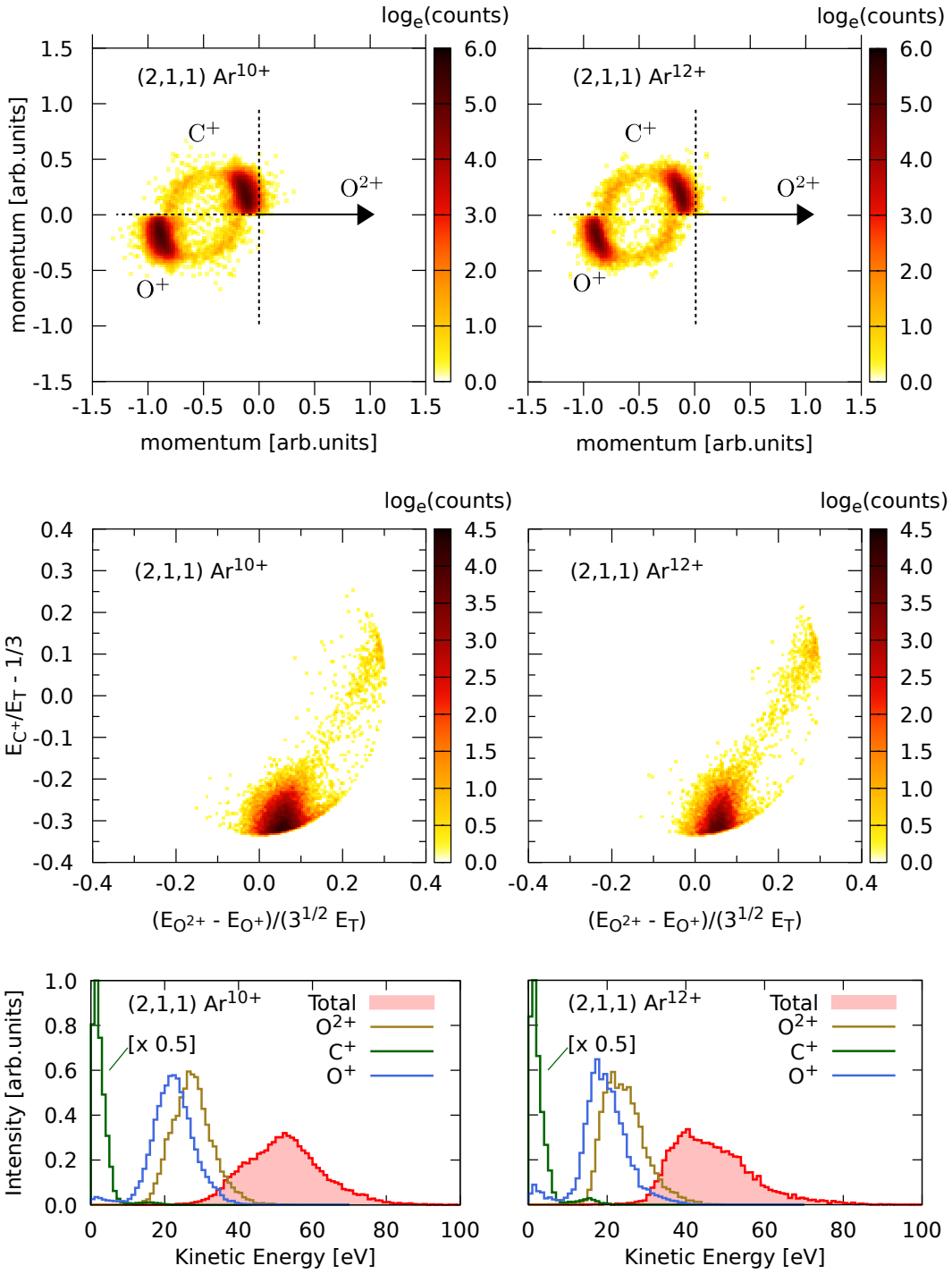


Figure 3.7: Newton diagrams (top), Dalitz plots (mid) and the kinetic energy distributions (bottom) of (2,1,1) channel for $Ar^{10+}$ and $Ar^{12+}$ impact. Note that the intensity scale for the KE distribution of $C^+$ for channel (2,1,1) has been halved.

In Dalitz plot of (2,1,1) channel for both Ar-ions, in addition to the intense region at the bottom, a weak trace is seen extending towards the top right. The bottom region is asymmetric about the $x = 0$ axis. It indicates that although the dissociation

leading to the (2,1,1) channel is concerted, it is asymmetric. The $C^+$−$O^{2+}$ bond stretches more than the $C^+$–$O^+$ bond. The additional asymmetric weak trace away from the intense region arises due to sequential dissociation of $CO_2^{4+}$ with a final sharing of charges as (2,1,1) via the $O^{2+}$ + $CO^{2+}$ intermediate stage. Along this weak trace, the normalized energy of $O^{2+}$ ion is constant, and momentum correlation exists between the $C^+$ ion and $O^+$ ion, coming from the second step of sequential dissociation. It can be understood using the equilateral triangle coordinate system, and its detail can be found here [105]. The Dalitz plot for $Ar^{10+}$ has comparatively broader and intense concerted region as compare to $Ar^{12+}$. By picking up events from regions of the Dalitz plot corresponding to sequential and concerted process, it has been found that the contribution of the sequential process to total events comes out to be around 6% for $Ar^{12+}$ and around 3% for $Ar^{10+}$ ion.

In the lower panels of Fig. 3.7, the KE distributions of fragments ($O^{2+}$, $C^+$, $O^+$) show that for the (2,1,1) channel, the peak of $C^+$ ion energy distribution lies slightly above zero because of the asymmetry of the dissociation. KE distributions of $O^+$ and $O^{2+}$ ions have peaks at higher values around 22.5 eV and around 27.0 eV for $Ar^{10+}$ and lie somewhat lower at around 17.5 eV and around 21.5 eV for $Ar^{12+}$. The small lobe in the KE distributions of $C^+$ at around 15 eV and of $O^+$ at around 3 eV correspond to sequential process, as has been verified by picking up events from the regions of sequential process in Dalitz plot.

## 3.4 Summary

In slow ($v < 1$ a.u.) HCI collisions, the ionization occurs via single or multiple capture of electrons from the target molecule, and the charge state of the projectile mainly governs the cross section of these capture processes. The multiply ionized molecular ions, thus formed, are generally unstable in nature, and subsequently dissociate into their atomic fragment ions. In this chapter, three-body dissociation dynamics of $CO_2^{4+}$, created under the impact of slow HCIs $Ar^{q+}$ ($8 \leq q \leq 14$) on $CO_2$ at an impact energy of 96 keV ($v = 0.3$ a.u.), was presented. Employing momentum spectrometry, the momentum vectors of all fragment ions originating from $O^+$+$C^{2+}$+$O^+$ (1,2,1) and $O^{2+}$+$C^+$+$O^+$ (2,1,1) dissociation channels were de-

termined. With the help of momentum information, the total KER distributions of these two channels were derived for all $Ar^{q+}$ ions. It could be readily realized that the total KER distributions of both channels are influenced by projectile charge $q$. In order to identify the participating electronic states of $CO_2^{4+}$ in its dissociation to (1,2,1) and (2,1,1) channels, *ab initio* quantum chemical calculations were carried out to obtain potential energy curves of $CO_2^{4+}$ under certain symmetry constraints. With the help of computed PECs, the values of the KER for both channels were estimated. Experimental KER distributions were fitted to the sum of multiple Gaussian distributions, and the centroids of the Gaussians were compared with the estimated KER values. The comparison revealed that the (1,2,1) channel arises mainly via excitation to $^1\Sigma^+$, $^3\Delta$, $^1\Pi$ states, while the (2,1,1) channel arises mainly via $^3\Delta$, $^7\Pi$ states. Furthermore, the area under the curve of each fitted Gaussian was approximated to the relative probability of accessing the corresponding electronic state of $CO_2^{4+}$, and the relative probability was found to depend on the charge state of the projectile. For the (1,2,1) channel, the low-lying $^1\Sigma^+$ was found to have the highest probability of being accessed for all projectiles except $Ar^{10+}$, whereas, for the (2,1,1) channel, the $^7\Pi$ state was found to dominate irrespective of the projectile, and especially for $Ar^{10+}$ impact. Taken together, the most striking difference in the relative contributions of different states was seen between $Ar^{10+}$ and $Ar^{12+}$ impact, which is likely to be a reflection of different ionization processes being at play for the two projectiles.

The bond breaking mechanisms of $CO_2^{4+}$ were also studied by visualizing the distribution of the correlated momenta of the fragments using Newton diagrams and Dalitz plots. It was observed that the (1,2,1) dissociation channel appears entirely via a concerted process, with symmetric stretching of the two bonds. The (2,1,1) channel is mostly due to the concerted process, with asymmetric stretching of the bonds, accompanied by a small amount of sequential process, with the doubly charged fragment separating first. The fraction of sequential dissociation process events was found to be higher for $Ar^{12+}$ than for $Ar^{10+}$ impact. For both dissociation channels, $Ar^{10+}$ gives a broader momentum distribution than $Ar^{12+}$ impact.

In conclusion, low energy HCIs are seen to be suitable candidates to influence the dissociation dynamics of polyatomic molecular ions. Depending on the projectile

charge, there are differences in the probabilities of participation of different excited states and these lead to patterns in the dissociation dynamics. Different projectiles can lead to a preponderance of certain ionization processes, which alters the probabilities of populating the excited states that are precursors to dissociation. The present experimental setup employed to perform this experiment has no provision to separate different ionization processes, which may be addressed by involving post collision projectile charge state analysis.

# Chapter 4

# Dissociation dynamics of molecular ion created under slow proton impact

## 4.1 Introduction

The last chapter discusses the dissociation dynamics of multiply ionized molecular ions under the impact of slow HCIs. In the case of slow HCI impact, the ionization of the target occurs dominantly via single or multiple captures of electrons from the target. In the case of a singly charged projectile ion impact, such as the simplest ion, the proton ($H^+$), the multiple ionization of the target can take place via pure direct ionization as well as single capture followed by autoionization of the target. The relative cross section of these two processes mainly depends on the proton's impact velocity ($v$) [106, 107].

In this chapter, we have presented the three-body dissociation of $CO_2^{3+}$ molecular ion, formed under the impact of protons at two impact velocities ($v$ = 0.5 and 0.83 a.u.), into $O^+$+$C^+$+$O^+$ dissociation channel. The proton with $v < 1$ a.u. impact results in ionization of the target molecule via both processes, i.e. direct ionization or capture ionization. On the other hand, for other projectiles, such as slow HCIs, capture ionization is the dominant process, and for electron impact, the direct ionization is the only possibility. A variety of projectiles can induce ionization by different ionization processes, and thereby different kinematics can be expected

in the dissociation of so-formed molecular ions. The motivation of this chapter is to focus on the comprehensive comparison of results obtained in proton impact with the results of collision systems where ionization of target molecule $CO_2$ is taking place dominantly via direct or capture ionization.

## 4.2 Experimental details

The same experimental setup and detection scheme are employed in this work as mentioned in previous chapter. The beam of $H^+$ ion, at velocities of 0.5 and 0.83 a.u., are delivered from EBIS. The low ion beam current, of the order of 10−15 pA, and low gas pressure (2–5$\times 10^{-7}$ mbar) are maintained during experiment. Ion beam overlaps with the effusive jet of target molecule $CO_2$ in collision chamber the IMS, and the momentum vectors of all fragment ions are measured.

## 4.3 Results and discussion

Three-body dissociation channel of $CO_2^{3+}$ into ionic fragments observed in the experiment is

$$CO_2^{3+} \rightarrow O^+ + C^+ + O^+ \tag{4.1}$$

The observed fragments $O^+$+$C^+$+$O^+$ can be formed either via a simultaneous breaking of the two bonds (the concerted mechanism), or a stepwise breaking of the two bonds, involving a briefly lived $CO^{2+}$ intermediate (the sequential mechanism). The two mechanisms are expected to result in not only differing angular correlations between the momentum vectors of the three fragments, but also differing KER distributions. Events corresponding to the two mechanisms can be separated using the Dalitz representation [76]. We analyze the Dalitz plots and the KER distributions of the fragments to understand the dynamics of the breakup of $CO_2^{3+}$ and the participation of different excited states, and we examine how a small variation in the energy of the proton projectiles affects these. Comparing our spectra with those for other HCI and electron impact, we identify the contributions from different intermediate states of $CO_2^{3+}$ to the KER spectra for a variety of projectiles.

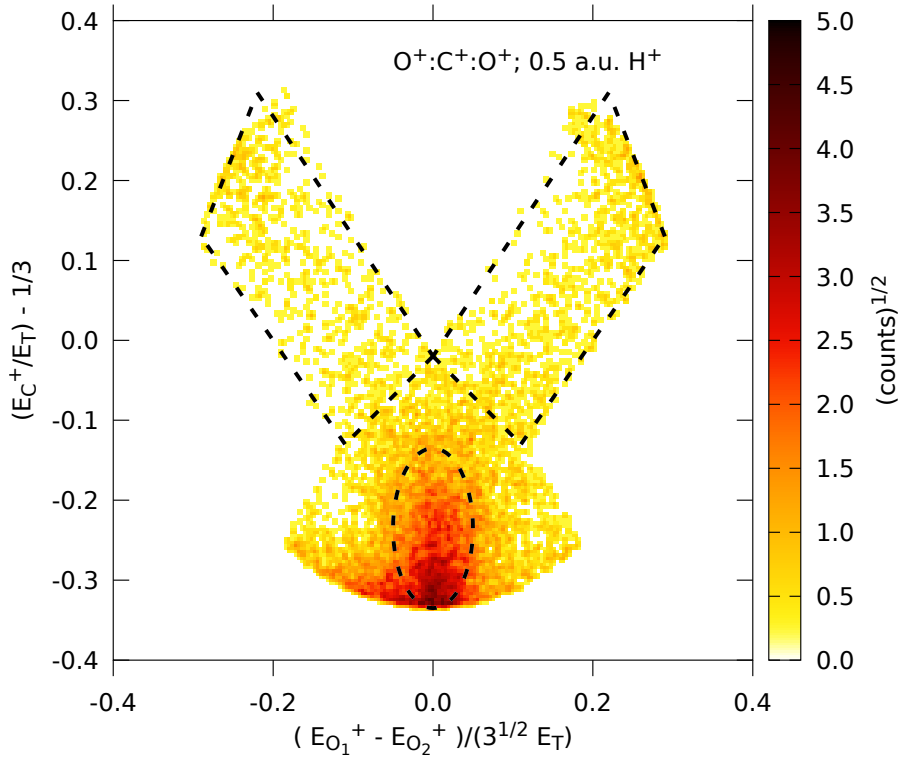


Figure 4.1: Dalitz plot for the $O^+ + C^+ + O^+$ breakup under 0.5 a.u. $H^+$ impact. The ellipse encloses events that are due to concerted breakup, while the quadrilaterals enclose events due to sequential breakup. Sharp boundaries appear due to polygon cuts in ToF coincidence map to avoid false data.

### 4.3.1 Separation of concerted and sequential processes

The correlated momenta of three fragments, in terms of their reduced kinetic energies, is represented using Dalitz plot. The $x$ and $y$ coordinates of a Dalitz plot are given by

$$x = \frac{E_1 - E_3}{3^{1/2} E_T} \qquad y = \frac{E_2}{E_T} - \frac{1}{3} \tag{4.2}$$

where $E_i$ ($i$ = 1, 2, 3) are the kinetic energies of the three fragments, and $E_T$ is the total kinetic energy release, $E_1 + E_2 + E_3$. For the present case, the subscript $i$ corresponds to $O^+_{(1)}$, $C^+$, $O^+_{(2)}$, respectively. Fig. 4.1 shows the Dalitz plot for this breakup due to 0.5 a.u. $H^+$ impact. The bottom oval-shaped area represents a concerted breakup in which both bonds of $CO_2^{3+}$ break simultaneously in a linear or bent configuration, while the area appearing as a V-shaped band corresponds to a sequential breakup with an intermediate $O^+ + CO^{2+}$ stage. Thus, appropriate

boundaries allow selection of events arising from distinct mechanisms. The Dalitz plot for 0.83 a.u. impact is essentially similar and is not shown here. Based on these separations, the KER distributions corresponding to the sequential and concerted processes leading to the same final fragments can be obtained.

### 4.3.2 Kinetic energy release distributions

The total KER distributions under the impact of $H^+$ ions of 0.5 a.u. and 0.83 a.u. velocities are shown in Fig. 4.2. The distributions for the constituent sequential and concerted breakups, separated with the aid of the Dalitz plot, are also shown. The total KER distribution lies higher than the sum of the two contributions, since the separation of two contributions is partial and also excludes some events. The total KER distributions for both impact energies have the main peak at 21 eV and another less prominent feature at 28 eV. However, for 0.83 a.u. impact another feature becomes prominent near 15 eV. Since KER distributions for both impact velocities arise from the same set of excited states of $CO_2^{3+}$, we identify local maxima in the spectra for the two impact energies, and assign the corresponding KER value as a possible peak position for spectra at all impact velocities. This approximation helps us identify features clearly and establish the contrast in the effects at two impact velocities. Three common features of varying intensity can be seen in each of the distributions for sequential and concerted breakup, and these are identified as $S_1, S_2, S_3$ and $C_1, C_2, C_3$, respectively. For both types of breakup, two of the features are strong and the third one is weak.

Further analysis is done by fitting the sequential and concerted components separately to the sum of three Gaussian functions. The centroids $\mu$ of the Gaussians are 14.5, 20, and 26 eV for the sequential components, and 21, 28, and 35 eV for the concerted components. The centroids are determined by a combination of the location of the features seen in the KER distributions and the most probable values expected from the Franck-Condon (FC) overlap of the $CO_2$ ground state with the $CO_2^{3+}$ states. The potential energy curve (PEC) of the latter set of states are taken from Wang *et al.* [108]. The width of the Gaussian function used for fitting to the KER distribution cannot be exactly determined. It is approximately determined based on the slope of the PEC of the upper state and the width of the FC region,

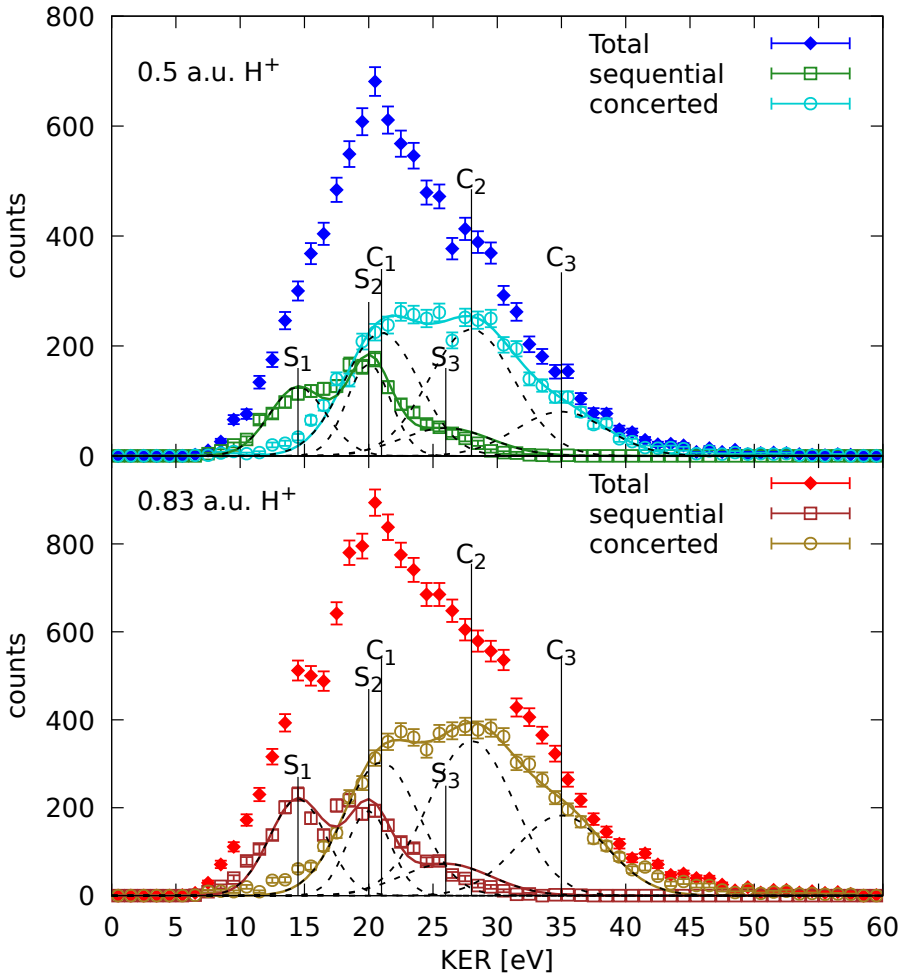


Figure 4.2: KER distributions for the $O^+ + C^+ + O^+$ breakup under $v = 0.5$ and $v = 0.83$ a.u. $H^+$ impact. Error bars on the experimental data show statistical errors. The total KER distribution is separated into contributions from sequential and concerted breakups based on the Dalitz Plot (events enclosed in the quadrilaterals and the ovals which are overlaid on the Dalitz plot in Fig. 4.1). The total KER distribution lies higher than the sum of the two contributions, since the separation is approximate and excludes some events. The sequential and concerted breakup data are separately fitted to the sum of three Gaussian functions each. They are identified as $S_1, S_2, S_3$ and $C_1, C_2, C_3$, and they have centroids at 14.5, 20 and 26 eV and at 21, 28 and 35 eV, respectively.

thus taking care that the width of the function is larger for steeper PECs. The amplitudes of the Gaussian functions are then determined by a least-squares fit to the experimental distribution. It should be noted that the PECs reported by Wang et al. are approximate. They have been computed for a linear symmetric geometry and for large intervals of the internuclear separations. Furthermore, the computations are done keeping the core orbitals inactive, and only valence orbitals

| projectile speed | Feature, centroid and probable contributing states | | | | | |
|---|---|---|---|---|---|---|
| | $S_1(14.5)$ ($^2\Pi$,$^4\Pi$) | $S_2$ (20) ($^2\Sigma^+$,$^4\Sigma^+$) | $S_3$ (26) ($^6\Sigma^+$,$^6\Pi$) | $C_1$ (21) ($^2\Sigma^+$,$^4\Sigma^+$) | $C_2$ (28) ($^6\Sigma^+$,$^6\Pi$) | $C_3$ (35) ($^8\Pi$,$^8\Sigma^+$) |
| 0.5 a.u. | 0.38±0.02 | 0.39±0.01 | 0.24±0.04 | 0.37±0.01 | 0.43±0.01 | 0.16±0.01 |
| 0.83 a.u. | 0.46±0.02 | 0.31±0.02 | 0.24±0.04 | 0.31±0.01 | 0.41±0.01 | 0.23±0.01 |

Table 4.1: Areas under the Gaussian curves fitted to the KER distributions of sequential and concerted breakups under proton impact. KER distributions of the two types of breakups are separately area normalized to unity. $S_1, S_2, S_3$ and $C_1, C_2, C_3$ are the features in KER distributions of sequential and concerted breakups respectively. The centroids of these features are in fair agreement with the estimates from the computed PECs of Wang *et al.* [108]; the identification of the participating states is also based on the same report. Errors shown are fitting errors.

are taken to be active. Hence, the accuracy in the assignment of the states and the KER values is limited.

Areas under the Gaussian curves thus obtained are listed in Table 4.1 for both impact energies. Since the collection efficiency of the spectrometer is less than unity for high-energy fragments, a correction needs to be applied to the high-energy part of the KER distribution. The correction will generally enhance the features at high KER values compared to the low-energy ones. This aspect has been elaborated upon for the case of a two-body breakup [109]. However, for a three-body breakup, which has a combination of sequential and concerted processes, the correction factor is complicated and will also depend on the geometry of the dissociating molecule. No systematic study of this correction appears to have been done so far. Thus, while the areas under the fitted peaks in Table 4.1 can be compared for different projectiles in the same experimental conditions, care should be taken in comparing with other reports.

We see that for $v = 0.5$ a.u., the states corresponding to features $S_1$ and $S_2$ contribute nearly equally in the sequential breakup. On the other hand, for $v = 0.83$ a.u., the $S_1$ feature at 14.5 eV is enhanced by $\approx 8\%$ while the feature $S_2$ at 20 eV is suppressed by a similar amount, indicating that the faster impact results in relatively higher probability of exciting low lying electronic states $^2\Pi$, $^4\Pi$ of $CO_2^{3+}$, as compared to the slower impact. Faster $H^+$ impact has also resulted in enhancement of the feature $C_3$ at 35 eV from a concerted breakup, corresponding to $^8\Pi$, $^8\Sigma^+$ states. We also find that the contribution of sequential breakup to total events at

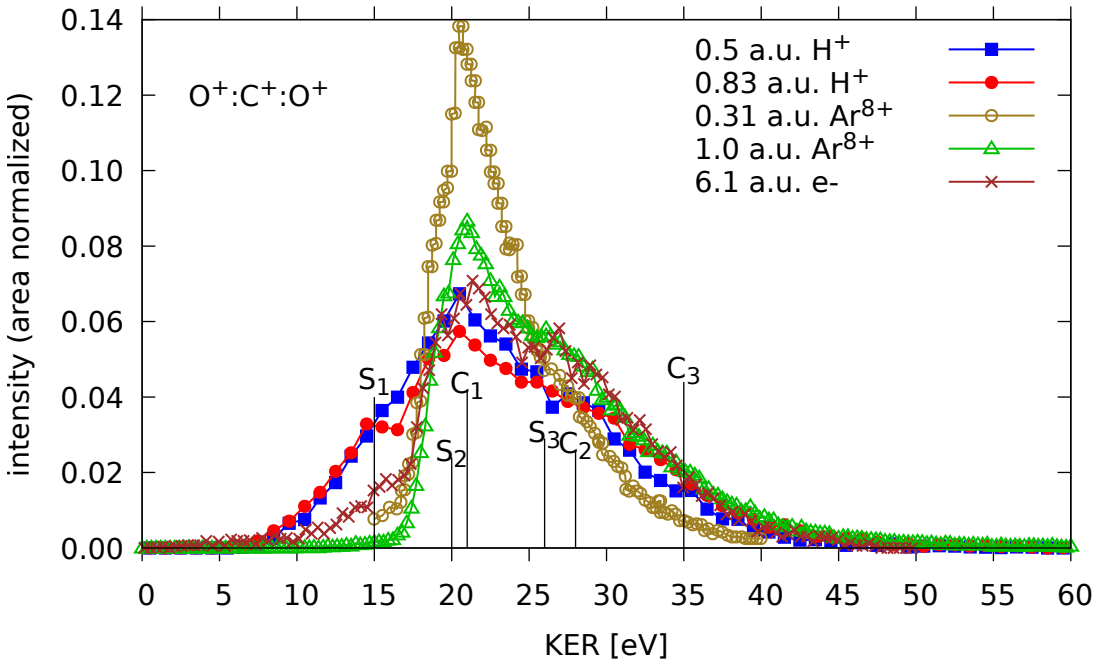


Figure 4.3: KER distributions for the $O^+ + C^+ + O^+$ break-up for the present $v = 0.5$ a.u. and $v = 0.83$ a.u. $H^+$ impact experiment (filled symbols) compared with the results from the literature for HCI impact at different velocities (open symbols, [76, 77]) and electron impact at $v = 6.1$ a.u. (crosses, [108]). The prominent low-energy feature, $S_1$, is common to electron and proton impact, but not seen at all in HCI impact. Feature $C_3$ is seen for all projectiles except 0.31 a.u. $Ar^{8+}$ [76], for which the dominant process is capture ionization. Each distribution is separately area normalized to its total counts.

both impact energies is 18%. This ratio has been reported to be around 20% for $Ar^{8+}$ impact [76, 77] and 12% for electron impact [108]. These observations show that a change of projectile considerably influences the relative contributions of different breakup mechanisms.

### 4.3.3 Comparison with KER for other projectiles

To contrast the excitation by protons with that by other projectiles, we compare the total KER distributions from the present investigation and those reported in the literature. Significant differences can be seen (see Fig. 4.3) between the present data and the data from previous experiments with slow HCIs [76, 77] and electron impact [108]. We find that the total KER distributions are well fitted by the sum of multiple Gaussians with the same values of the centroids and widths as in our proton impact data. Based on the fits, the contribution of different features in these

reports can be identified. However, since the features $S_2, C_1$ and $S_3, C_2$ are very close lying and cannot be separated in the total KER, these pairs of features are taken together while making the comparison.

### HCI impact

In the report by Neumann *et al.* [76] for the $O^+ + C^+ + O^+$ breakup exclusively via capture ionization by 0.31 a.u. $Ar^{8+}$ impact, the total KER distribution is in the range 15–40 eV, and is found to be composed mainly of contributions from features $S_2, C_1$, and from $S_3, C_2$. There is negligible contribution from $S_1$ and $C_3$. In contrast, in the report of Khan *et al.* [77] for $Ar^{8+}$ at $v = 1$ a.u., the KER distribution extends from 15 eV to 50 eV with no contribution from feature $S_1$, significant contributions from $S_2, C_1$ and $S_3, C_2$, and a weaker contribution from $C_3$. The main difference in the KER distribution of fragments for the two impact velocities of the same projectile is that the KER distribution is broader for the faster projectile and has contributions from higher-lying states of $CO_2^{3+}$. This is plausible, since at higher projectile velocities close encounters are more probable, leaving the molecular ion in comparatively higher-lying electronically excited states.

### Electron impact

The only detailed report for electron-impact triple ionization of $CO_2$ is for $v = 6.1$ a.u. (500 eV), by Wang *et al.* [108]. There the KER distribution ranges from 10 to 50 eV with contributions of all features with varying intensities. The main difference from the HCI case is the appearance of the feature $S_1$ , which is also seen in the present proton impact data. The appearance of this feature was attributed to the difference in the ionization processes: slow HCI impact predominantly causes multiple electron capture, and it does not populate the lowest states $^2\Pi$ and $^4\Pi$, whereas under electron impact there is a propensity to populate the lowest-lying states. The rest of the features in their data (viz. $S_3, C_2, C_3$), are comparable in intensity to that for 1 a.u. $Ar^{8+}$ as well as the present proton impact data.

We see in Fig. 4.3 that the KER distribution for slow $H^+$ ion impact shows all of the features of electron impact and also an overall range comparable to that

for slow HCI impact considered here. The noteworthy point is that under electron impact, electron capture is impossible and multiple ionization can occur only by direct ionization. So the $S_1$ feature cannot arise from electron capture. Scully *et al.* [110] have shown that the contribution of inner shell ionization is significant at these electron energies, along with outer shell ionization. It should be noted, that proton impact with $v < 1$ results in ionization only from the outer shell of the target [111]. However, inner shell ionization will, by and large, lead to high lying states of $CO_2^{3+}$, and, thus higher KER values. Consequently, it will not contribute to the $S_1$ feature. Slow protons cause multiple ionization via direct ionization or single capture processes, whereas slow HCIs cause multiple ionization mainly through multiple capture of electrons from a target molecule with negligible direct ionization, generally resulting in a narrower KER range [60, 76, 107]. In particular, as seen in Fig. 4.3, low lying electronic states of $CO_2^{3+}$, corresponding to the $S_1$ feature, which are accessed under proton impact, are not accessed in ionization via electron capture by a multielectron projectile.

Putting together our proton impact results and the results of HCI and electron impact, it can be concluded that the $S_1$ feature must arise due to direct ionization of outer shells, which result in low-lying $CO_2^{3+}$ excited $^2\Pi$, $^4\Pi$ states. The enhanced $S_1$ feature under 0.83 a.u. $H^+$ impact (as opposed to 0.5 a.u. impact) is likely to be due to the increased probability of direct ionization. In this proton energy range, the cross-sections for direct and capture ionization are comparable and show opposite tendencies with increasing impact energy [106]. Further enhancement in the $S_1$ feature can be anticipated with increasing proton energy until inner shell ionization contributes significantly.

## 4.4 Summary

In this chapter, we have shown that the triple ionization of $CO_2$, populating a wide range of transient states, can be achieved by even the simplest of ions — the proton — in the velocity range $v < 1$ a.u. Despite being a structureless projectile, a small variation in the impact velocity of the proton affects the breakup dynamics in this regime. This is because of the changes in the relative contribution of different

ionization processes with a change in impact velocity.

A particularly noteworthy feature in the KER distribution for triple fragmentation of $CO_2^{3+}$ is the one around 15 eV, which has been reported for electron impact but not for HCI impact. The feature is found to be stronger for 0.83 a.u. than 0.5 a.u. proton impact in the present study. It is identified that this feature results from dissociation via low lying $^2\Pi$, $^4\Pi$ electronic states of $CO_2^{3+}$. It is found that, in an energy range where the cross-sections for electron capture and direct ionization compete with each other, a small variation in impact energy results in enhanced access to low-lying electronic states of $CO_2^{3+}$ via direct ionization of the outer shells of $CO_2$. Ionization by protons may involve capture, which is impossible with electron projectiles, but both can induce direct ionization. Especially with fast ($v \gg 1$ a.u.) electrons, inner shell ionization will be significant, while slow ($v < 1$ a.u.) protons will mainly induce direct ionization or capture from outer shells. Despite these differences, we find that the KER distribution for the triple fragmentation with slow protons shows nearly all the features seen with fast electrons.

Separation of ionization process can be addressed by more involved experimental strategies comprising post-collision projectile charge state analysis. By doing so, more direct experimental evidence can be brought regarding the effect of different ionization processes on the breakup dynamics of molecular ion $CO_2^{3+}$. At the time of this experiment, the limitation of our experimental setup did not allow us to separate direct and capture ionization processes under proton impact.

In the near future, it would be interesting to study the breakup dynamics and the changes in the breakup patterns at higher proton impact velocities ($v > 1$) since, in this regime, a competition between processes such as capture and direct ionization from outer and inner shells of the target is expected. Furthermore, accurate potential energy curves of $CO_2^{3+}$, taking into account asymmetric configurations and non-linear geometry, are needed for a proper comparison with experimental KER values and exact identification of the transient states responsible for the observed breakup patterns.

# Chapter 5

# Post collision analyzer for studying charge-exchange processes

## 5.1 Introduction

In last two chapters, I have presented the studies on dissociation dynamics of multiply ionized molecular ions. The investigations have been carried out by the impact of slow ($v < 1$ a.u.) highly charge ions (HCIs) and proton on $CO_2$ molecule. Such collisions can excite the molecule into its various available excited states. If the perturbation is strong enough, the excitation can result in multiple ionization of target. The process through which a charge projectile ionizes the target can be conveniently classified into two: direct ionization and charge-exchange ionization. In direct ionization, the charge state of projectile remains unchanged after the collision with target. However, in charge-exchange processes, the charge state of the projectile gets changed. Both kind of processes may lead to formation of multiply ionized molecular ions in a wide range of excited electronic states.

In chapter 3, we have reported how the probability of accessing different electronic states of molecular ion depends on the projectile charge $q$ in slow HCI projectile impact. It was demonstrated by performing a series of experiments with impact of $Ar^{q+}$ of various charge states. In chapter 4, we have also seen that slow protons, which are one of the simplest projectiles, are able to excite the $CO_2$ molecule to a broad range of triply ionized transient states, spanning those accessed by the impact of slow HCI and also those accessed by electron impact, but with varying probabili-

ties. These observations indicate that the underlying different ionization processes, induced by different charge projectiles, play a vital role in determining the exact nature of the excitation of target to its various excited states. The projectiles of different properties can lead to the different propensities for excitation via different ionization processes. Hence separation of processes is needed for determining the exact excitation. Direct and capture ionization can be separated by analyzing the charge state of the projectile after the collision. By doing so, we would be able to infer more about the pattern observed in dissociation of molecular ions created by different charged projectile ions. However, to accomplish it, coincidence measurements between observed fragment ions with charge changed projectile are required for which a post-collision CSA is built. The fragment ions are measured by the existing recoil ion momentum spectrometer (IMS) [91].

This chapter is divided into two parts. First part includes the discussion of CSA, its working principle, simulations, its assembly and characterization. The second part presents experimental application and results.

## 5.2 Charge-state analyzer

Analyzers based both on electrostatic and magnetostatic fields can be used to analyze the charge state of post-collision projectile ion. However, for keV energy range and for certain types of experiments, it is convenient to use analyzers based on electrostatic rather than magnetic field. Electrostatic analyzers (ESAs) have wide range of designs due to fact that many geometrical configurations are possible which conveniently alter the trajectories of particles. All ESAs work on the principle of discrimination of particles based on their $E/q$ ratio. There are mainly two categories of ESAs: (1) mirror type analyzers (2) deflector type analyzers. In the mirror type, particles are first retarded and, then accelerated back to their original energies. Parallel plate mirror analyzer (PPA) and cylindrical mirror analyzer (CMA) are two common types of mirror analyzers. In deflector type analyzers, the energy of charged particles remains approximately constant along a circular optic axis. A toroidal analyzer is most generalized deflector type analyzer. There are two characteristics radii, major radius ($R$) and minor radius ($r$), and one angle ($\phi$) in a toroidal

analyzer. Spherical deflector (SDA), cylindrical deflector (CDA) and parallel plate (PPA) analyzers are the special cases of toroidal type analyzers. For SDA, both $R$ and $r$ have definite values and $\phi = \pi$. For CDA and PPA, $r = \infty$, $\phi = \pi/\sqrt{2}$ and $R = r = \infty$, $\phi = 0$, respectively. More details about classification can be found in well described article [112]. PPA, just a pair of parallel deflector plates, is a very commonly used analyzer. Suitable potential difference applied on these deflector plates results in bending of ion beam and thereby spatial separation between trajectories of particles having different energy-to-charge ratio $E/q$ can be achieved.

For our application, we find the cylindrical deflector analyzer (CDA) the optimum choice. It is efficient, simple to assemble and relatively inexpensive to machine. Because of its focusing property, when a specific deflection angle is chosen, it also leads to an efficient transmission of ions. Details are discussed in the next subsection.

### 5.2.1 Cylindrical deflector analyzer working principle

CDA consists of two concentric cylindrical sector electrodes of different radii $R_1$ and $R_2$ subtending the same angle $\phi$ at centre. It is found that the cylindrical plates, that results in $r^{-1}$ dependent electrostatic field, provides slit-to-slit focusing at angle $\phi = \pi/\sqrt{2} \approx 127.27°$ [113]. Fig. 5.1 shows a schematic diagram of deflection plane and end view of CDA. Two slits are shown to define the entrance and exit of CDA. Particles are injected along the median arc i.e. in a direction tangent to the circular arc of radius $R_0$. The potential difference $\Delta V$, that is required to pass an ion with energy-to-charge ratio $E/q$, between the plates along the median arc is given by [114]:

$$\Delta V = \left(\frac{E}{q}\right) \times 2\ln(R_2/R_1) \tag{5.1}$$

where $\Delta V$ is in volts, energy $E$ is in eV and $q$ is in units of electron charge. Ions with different $E/q$ ratio are deflected along other arcs. The energy resolution of analyzer is given by,

$$\frac{\Delta E}{E} = \frac{d}{R_0} + \frac{2}{3}(\Delta\alpha)^2 + \frac{1}{2}(\Delta\beta)^2 \tag{5.2}$$

where $d$, $\Delta\alpha$ and $\Delta\beta$ are slit width, and entrance angles in deflection plane and perpendicular to deflection plane, respectively [115, 116]. A CDA in its 127° configuration is rarely used as a analyzer, because of its awkward geometry, in spite of

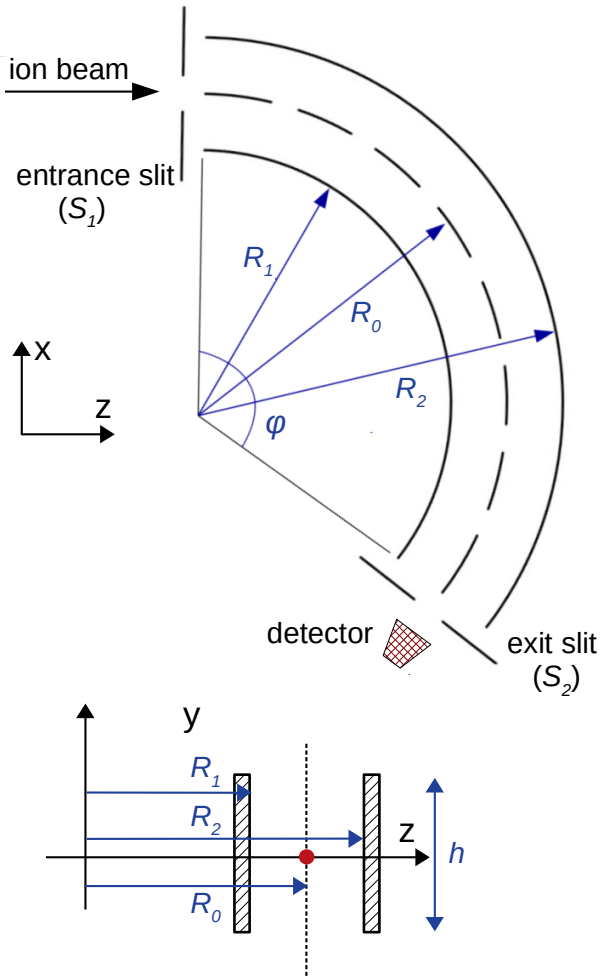


Figure 5.1: (Top) Deflection plane ($xz$) of cylindrical deflector analyzer (CDA). $R_1$ and $R_2$ are radii of inner and outer cylindrical sectors, respectively. $S_1$ and $S_2$ define entrance and exit slits of CDA. (Bottom) Section view in any radial cut of CDA. Circular dot shows the projection of transmitted ion beam at exit slit, and $h$ is height of both sectors.

its superior focusing characteristics. A crucial advantage of CDA in comparison to commonly used parallel plate deflector is that CDA has focusing property resulting in improved transmission [113]. However, the CDA focuses only in deflection plane ($xz$-plane) with no focusing in its normal $y$-direction. It results in an image that is elongated along the $y$-direction and is sharp in the $xz$-plane. The focusing action in $y$-direction can be achieved up to a certain extent by doing slight modification in CDA geometry which is discussed in further section.

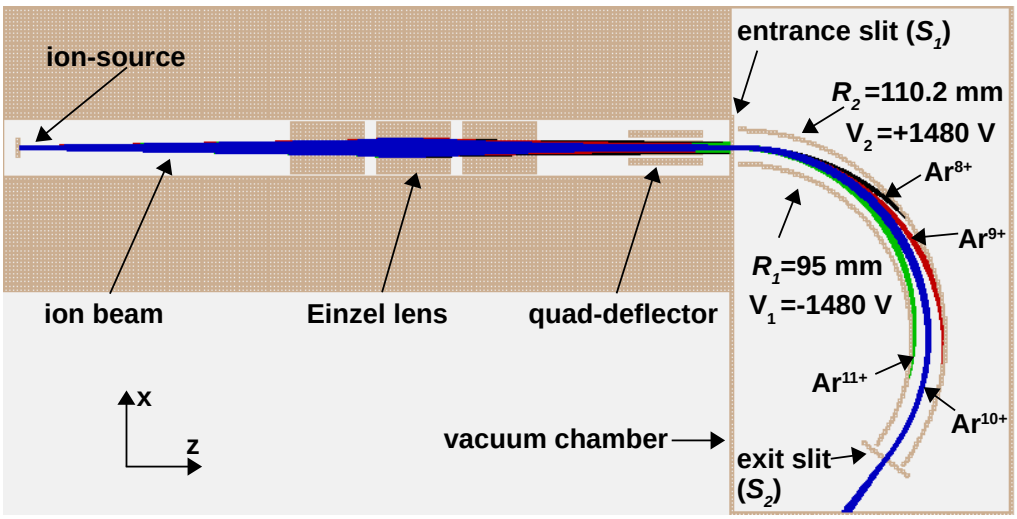


Figure 5.2: SIMION simulation of cylindrical deflector analyzer (CDA). The ion beam consists of a charge distribution $Ar^{q+}$ $(8 \leq q \leq 11)$, each with an energy of 96 keV. The voltages on CDA sectors are applied to pass ions with an energy-to-charge $E/q$ ratio of 9.6 keV/$q$, resulting in $Ar^{10+}$ ions passing through CDA. The diameter of the beam at the source position is 2 mm, and the divergence of the beam in the deflection plane and its perpendicular plane is 1° each. The width of slits $S_1$ and $S_2$ is 2 mm and both are grounded.

### 5.2.2 Simulation results of CDA

All simulations have been done using SIMION suite of programs [117]. We have performed the simulation of $\phi = 127°$ CDA, for particles in the energy class 10 keV/$q$, shown in Fig. 5.2. The CDA consists of two cylindrical sectors of equal heights $h = 60$ mm with radii of $R_1 = 95$ mm and $R_2 = 110.2$ mm. So, the radius of centre arc would be $R_0 = 102.6$ mm. Two slits $S_1$ and $S_2$ of width 2 mm, are used to define the entrance and exit of CDA, respectively. The incoming ion beam consists of a charge distribution, $Ar^{q+}$ $(8 \leq q \leq 11)$ at energy of 96 keV. For practical point of view, the ion-source is located 400 mm upstream of slit $S_1$ of CDA. The diameter of ion-beam at source position is taken to be 2 mm and divergence of beam in the deflection plane $(\Delta\alpha)$ and its perpendicular plane $(\Delta\beta)$ is 1°. In many real cases, the beam could be nearly parallel or have a much smaller divergence, achieving better focusing and reduced loss of flux. However, for a greater tolerance to different beam conditions and flexibility of operation, we have included an Einzel lens and a quadrupole deflector to manipulate the beam as it enters the CDA.

Einzel lens, also known as unipotential lens, is very commonly used types of electrostatic lens. Einzel lens is a combination of three cylindrical symmetric electrodes

held at appropriate potentials. The distinctive property of Einzel lens is that the outer electrodes have same potentials $V_1$ while the central electrode is at different potential $V_2$. This potential arrangement keeps the energy of beam nearly constant while focusing. In simulation, the length, outer diameter and inner diameter of each cylindrical electrode of Einzel lens is 40 mm, 38 mm and 14 mm, respectively. The separation between two consecutive electrodes of lens is 7 mm. Furthermore, a set of two pairs of parallel plates, forming a quadrupole deflector, is used to steer the ion beam in two orthogonal directions. The dimension of each rectangular plate of quadrupole deflector is set as 40 mm $\times$ 8 mm $\times$ 3 mm. The voltages on the four electrodes can be independently controlled.

As Eqn. 5.1 suggests an ion of particular energy-to-charge ratio, $E/q$, value can be transmitted through CDA by applying suitable voltages. Fig. 5.2 shows the simulation results where the $\pm$1480 V on CDA plates are applied to pass ions having $E/q$ value 9.6 keV/$q$. However, other nearby charge states, $q = 8, 9$ and 11, having different $E/q$ values, are deflected inward or outward depending on whether their $E/q$ values are lower or higher than the allowed value. Similarly, the charge states, $q = 8, 9$ and 11, can also be made to pass through CDA individually by applying appropriate voltages.

In cylindrical deflectors, there is an electric field, acting on the ions in the $xz$-deflection plane, which results in focusing of ions in $xz$-plane. If the incoming ion beam in the $xz$-plane has a certain divergence at entrance $S_1$, the acting electric field results in the focusing of the ion beam in the $xz$-plane at exit $S_2$ [113]. However, there is no such field in $y$-direction, perpendicular to deflection plane, so a divergent beam will continue to spread as it propagates through the CDA which results in an image that is elongated along the $y$-direction and is sharp in the $xz$-plane. It can be understood by simulation, shown in Fig. 5.3 (top). Initially, the width of beam is 2 mm with divergence of 1° at source position, and after passing through CDA, it grows to 16 mm in $y$-direction at the exit. However, the focusing action in $xz$-deflection plane can be observed clearly in Fig. 5.2, and beam remains nearly 2 mm in the $xz$-plane.

In order to achieve focusing action in $y$-direction as well, CDA with cylindrical sectors of differing heights are exploited. The cylindrical sectors of different heights

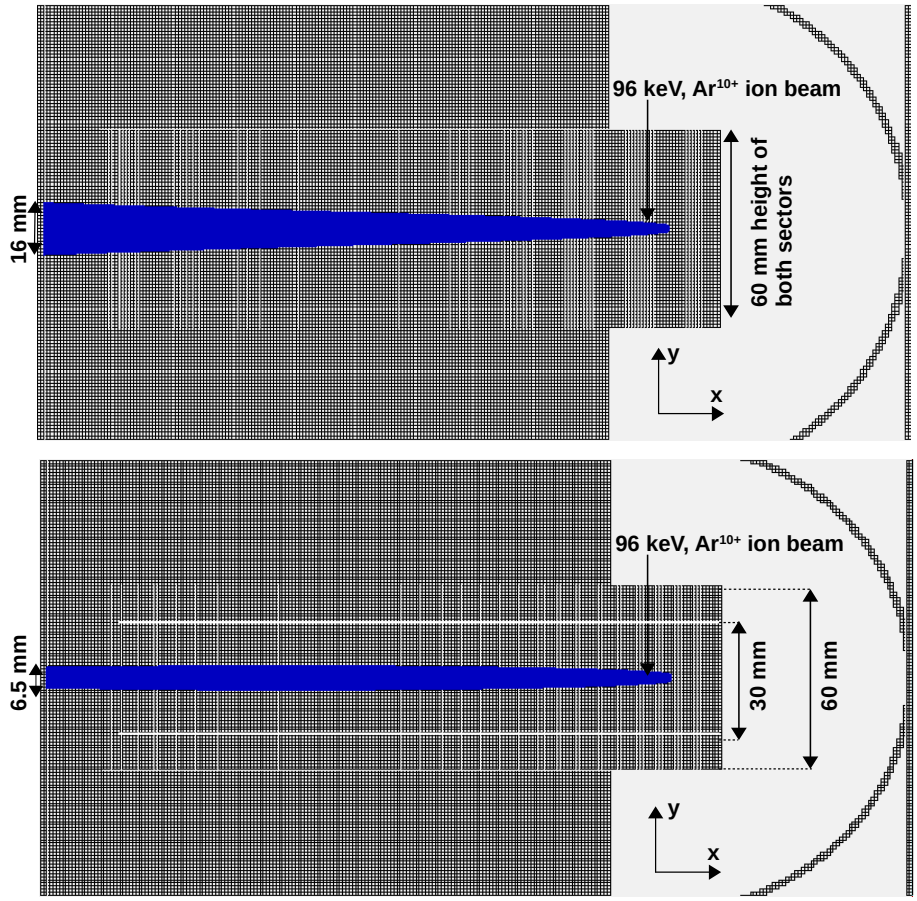


Figure 5.3: SIMION simulation of CDA (top) with cylindrical sectors of equal height $h_1$=$h_2$=60 mm and (bottom) with cylindrical sectors of unequal heights $h_1$=30 mm (inner sector) and $h_2$= 60 mm (outer sector). The beam properties and applied voltages are the same as in the simulation shown in Fig. 5.2. In case of equal heights (top), the beam trajectories in the $y$-direction, normal to the $xz$-deflection plane, diverge as the beam propagates. The width of the beam grows to $\approx$ 16 mm in the $y$-direction at the exit. In case of unequal heights (bottom), the focusing in the $y$-direction is achieved up to a certain extent resulting in a comparatively narrower beam $\approx$ 6.5 mm at the exit.

result in curvature of equipotential lines between the electrodes in the region above and below the nominal deflection plane. The curvature of equipotential lines causes an electric field component out of deflection plane which leads to focusing action in $y$-direction. It was first introduced by Kreckel *et al.* in a 90° deflector [118]. Fig. 5.3 (bottom) shows the simulation of CDA of cylindrical sectors with different heights 60 mm and 30 mm, keeping all other parameters (plate radii 95 mm,110.2 mm, voltages and beam properties) unchanged as used in simulations Fig. 5.2. Comparison with Fig. 5.2, it clearly shows that ion beam is now focused, up to a certain extent, in the $y$-direction as well. The width of the beam is reduced to 6.5 mm from 16 mm.

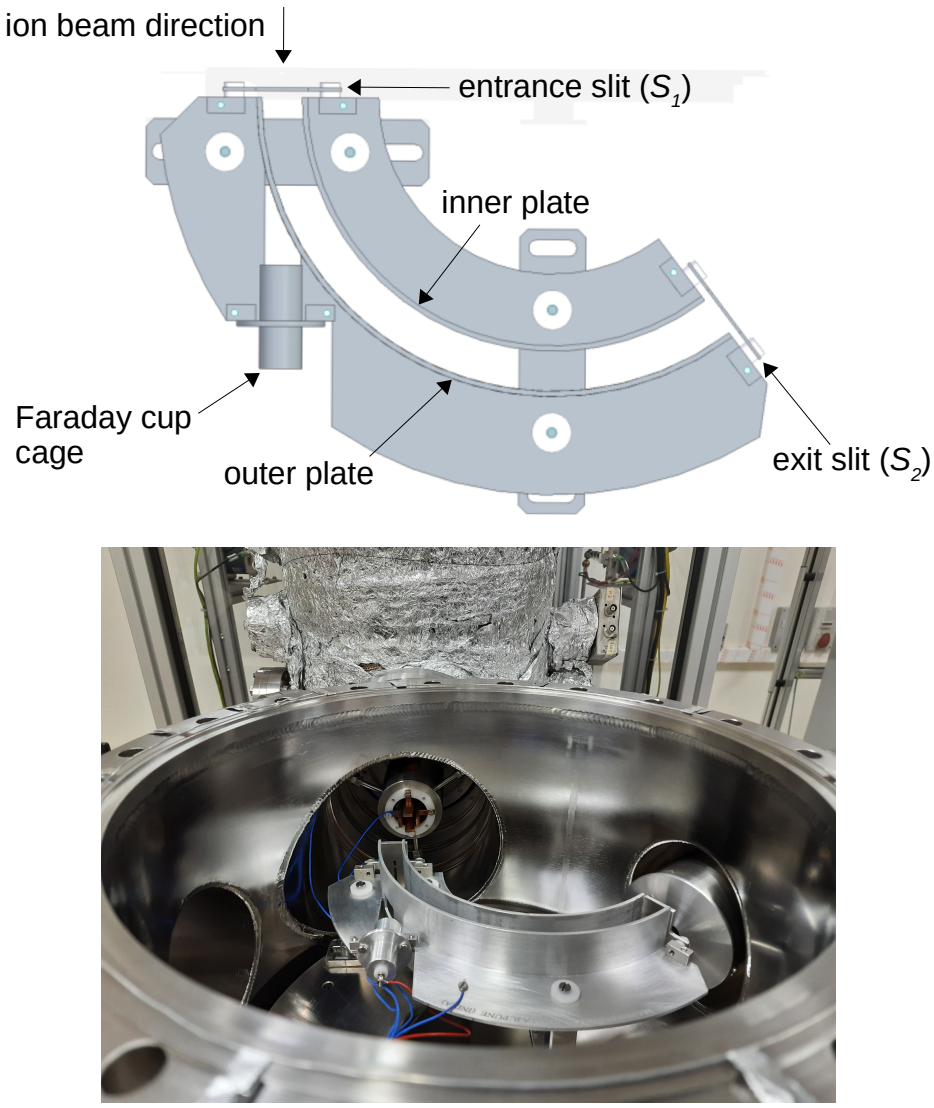


Figure 5.4: (Top) CDA Drawing made in solid edge 3D software suit, (bottom) picture of CDA assembly. CDA chamber diameter is 300 mm.

Thus, higher transmission can be achieved by introducing a slight modification in the plate geometry of CDA. The CDA has been fabricated with both options (equal and unequal heights). The results reported here are for equal heights.

### 5.2.3 Assembly of CDA

The mechanical designing of CDA is done using Solid Edge 3D software suite [119]. Fig. 5.4 shows the drawing of CDA with marking of various components (top) and the picture of CDA assembly in experimental setup (bottom). The designed CDA is built with non-magnetic components and housed in a non-magnetic stainless steel chamber (the CDA chamber) of 300 mm diameter and 250 mm height. The CDA

chamber is maintained at vacuum condition of the order of $\approx 2 \times 10^{-9}$ mbar. All dimensional details of CDA are same as discussed in the simulation section and shown in Fig. 5.2. A shielded Faraday cup is mounted downstream of $S_1$, collinear with the incoming ion beam, after a slit on the outer sector plate, to detect the incident beam when the CDA voltages are zero.A channel electron multiplier (CEM) of 10 mm diameter is mounted at the exit of CDA to detect the ions transmitted when suitable voltages are applied to its plates. The CEM is operated in two modes: in the linear mode for measuring the transmitted beam current (during calibration) and in the saturation mode (counting mode) for coincidence measurements with the collision products. In the present CDA assembly, cylindrical sectors of equal heights $h = 60$ mm are employed.

## 5.3 Characterization of the CDA

In this section, characterization of the CDA including its calibration and transmission function is presented. It is accomplished using ion beam delivered from EBIS (its detail is discussed in chapter 2).

### 5.3.1 Calibration

The calibration of CDA is done using an ion beam of known $E/q$ value and known current delivered by an EBIS. Here, the CDA with sectors of equal height $h = 60$ mm is employed. With no voltage applied on CDA sectors, the incoming ion beam current is measured on a Faraday cup. By focusing and steering the ion beam, we ensure that 95% or more fraction of current is recorded on the Faraday cup, which ensures negligible or no loss of incoming ion beam occurring at CDA entrance $S_1$. Once the beam alignment is achieved, suitable voltages, approximated from simulations, are applied to CDA sectors to pass the ions of different $E/q$ values through it. Fig. 5.5 shows the simulated and experimentally observed voltages needed to pass $Ar^{q+}$ ions of different $E/q$ values. Symmetric voltages of opposite polarities $+V$ and $-V$ are applied on the outer and inner sectors of CDA, respectively.

According to Eqn. 5.1, to pass the ion through CDA, there would be a linear relationship between applied voltages and $E/q$ values of ion, which can be clearly

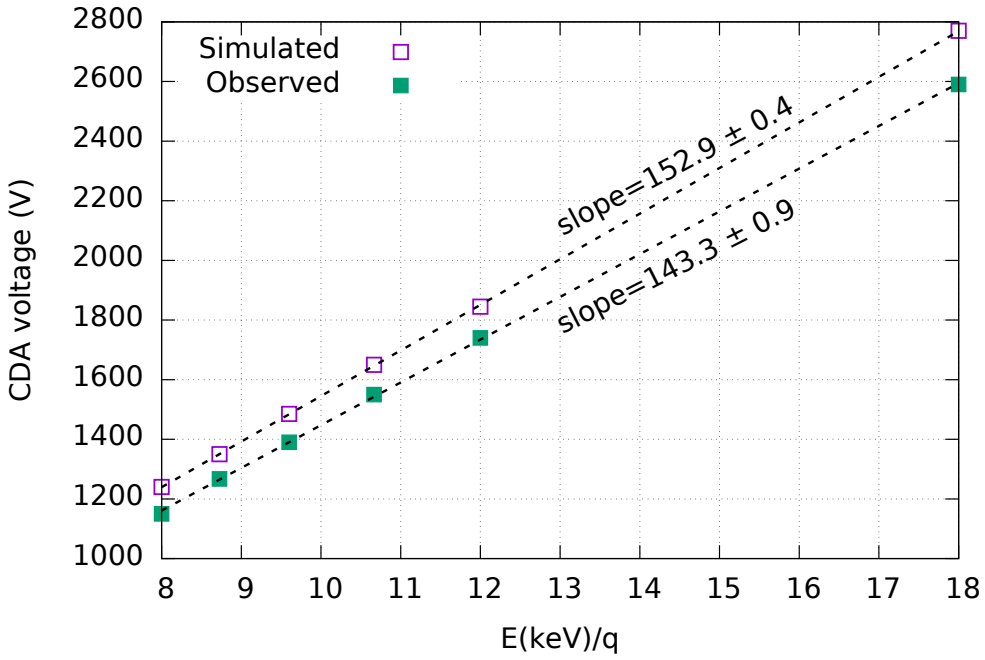


Figure 5.5: A calibration curve of CDA. Projectiles of different $E/q$ values are transmitted when the suitable voltages on the CDA sectors are applied. There is slight difference between the simulated and experimentally observed voltages which is more or less consistent, and this can be explained by a small difference in the designed gap between the sectors and the actual gap. Symmetric CDA voltages ($V$) of opposite polarities $+V$ and $-V$ are applied on outer and inner plates of CDA, respectively. The uncertainty in CDA voltage is around 1.5%, based on the width of a Gaussian fit to the transmission function, and is smaller than the symbol size.

seen in experimentally observed values in Fig. 5.5. However, there is more or less a consistent difference between simulated and experimentally observed voltages. The slope of simulated values and experimental data points are 152.9±0.4 and 143.3±0.9, respectively. By using Eqn. 5.1, the corresponding values of ratio $R_2/R_1$ can be calculated which are found to be 1.165 and 1.154, respectively. The smaller value of $R_2/R_1$ for experimentally observed data points indicates that the actual gap between CDA sectors is slightly smaller than the designed gap. This difference could be because of machining tolerance or in assembling of the CDA, which results in such a difference in the gap between the sectors.

### 5.3.2 Transmission function

Fig. 5.6 displays the graphs of experimentally observed transmission function, with Gaussian fits, of the CDA for $Ar^{10+}$ and $Ar^{16+}$ ions at 9.6 keV/$q$ and 18 keV/$q$,

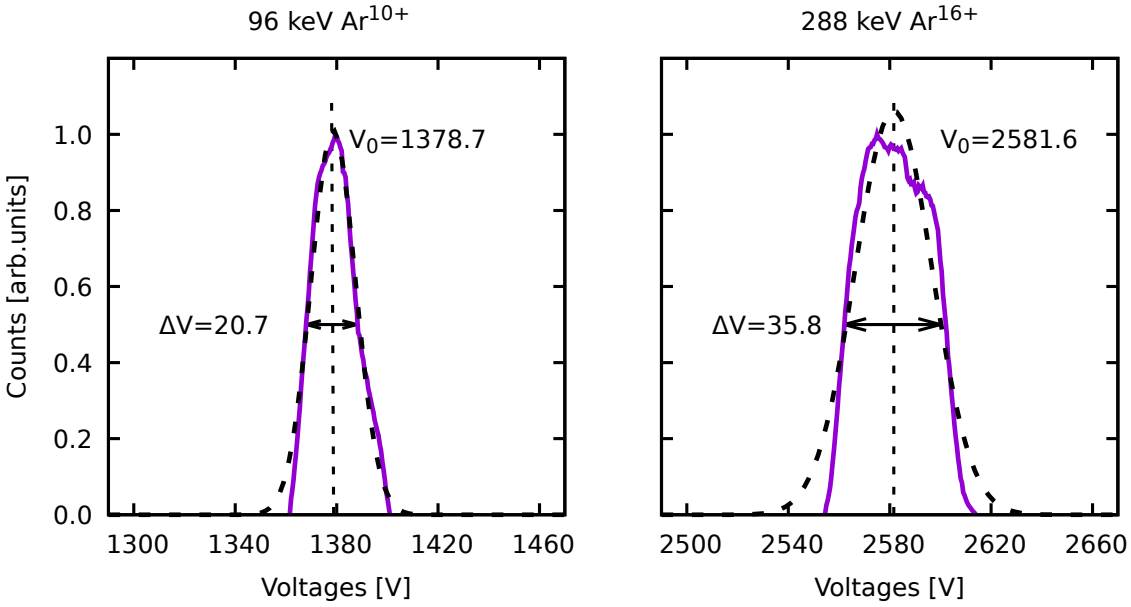


Figure 5.6: Experimentally observed transmission function of the CDA and Gaussian fits to the experimental data for two projectiles, [Left] 9.6 keV/$q$ $Ar^{10+}$ [Right] 18 keV/$q$ $Ar^{16+}$.

respectively. In order to obtain the transmission function, an ion beam of particular $E/q$ value is allowed to pass through the CDA and the transmitted current is recorded. Firstly, the suitable voltages ($\pm V_0$) on sectors are applied such that the recorded transmitted current on CEM is maximized. Later on, the voltages of both sectors are varied symmetrically around $V_0$ in both directions in step of 0.5 V and the corresponding current is recorded. For $Ar^{10+}$, the mean value $V_0$ and FWHM are 1378.7 V and 20.7 V, respectively. For $Ar^{16+}$, the corresponding values are 2581.6 V and 35.8 V. For both impacts, the value of FWHM is $\approx$1.5% of its mean value, showing a narrow transmission function. It should be noted, that variation either in $E$ or $q$, keeping the other quantity fixed, can in principle be analyzed with this device. However, the primary aim of this experimental setup is to separate charge changes in nearly monoenergetic projectiles as a result of the collisions, and not to carry out projectile energy-differential measurements. Taking together Fig. 5.5 and Fig. 5.6, it can be realized that with the help of present CDA assembly, the separation of ions of different $E/q$ values can be achieved efficiently in the range of energies employed for our experiments.

So far we have discussed the CDA working principle, its simulation, assembly and finally its characterization. We have seen its capability to separate highly charged

ions of different $E/q$ values. From simulations we know that the focusing property of CDA further also ensures the efficient transmission with negligible loss. We now turn our attention to implementation of the CDA for post-collision analysis of ion-molecule collisions.

## 5.4 Implementation and results

In introduction of this chapter, we discussed the necessity of separating different ionization processes in ion-molecule collision experiments. Depending on the ionization process, the $E/q$ value of the projectile will either remain unchanged, or change in a discrete manner, due to the change in $q$. There is usually only a minor change in the value of $E$. In both cases, projectile ion after the collision will have some definite value of $E/q$ ratio. The capability of CDA to analyze ions of different $E/q$ values is useful for separating these processes in ion-molecule collisions. This is achieved by installing the CDA downstream of the existing collision chamber.

### 5.4.1 Coupling of CDA to IMS

Fig. 5.7 shows the schematic diagram of complete experimental setup to investigate different ionization processes in ion-molecule collision. A projectile ion beam overlaps with effusive beam of target gas molecule at the centre of IMS. It can be seen that the post-collision projectile-ion travels a finite distance from collision centre to CDA entrance. Then, it becomes necessary to maintain its smooth transport to CDA entrance slit so as to avoid transmission loss. In order to achieve this, the actions of Einzel lens and quadrupole deflector are employed to ensure focusing and alignment of post-collision projectile ion. The CDA is housed in one vacuum chamber (the CDA chamber), while the momentum spectrometer is housed in another chamber (collision chamber) of 300 mm diameter and 570 mm height. The two chambers are coupled via CF150 ports and a CF150 bellow. The CDA chamber and the collision chamber are together pumped using a 500 l/s turbo-molecular pump backed by a dry scroll pump. The chambers are maintained at a vacuum of order $2 \times 10^{-9}$ mbar, which is crucial for ensuring that ionization and charge transfer via collisions with the residual gas is negligible. The large diameter coupling port ensures sufficient

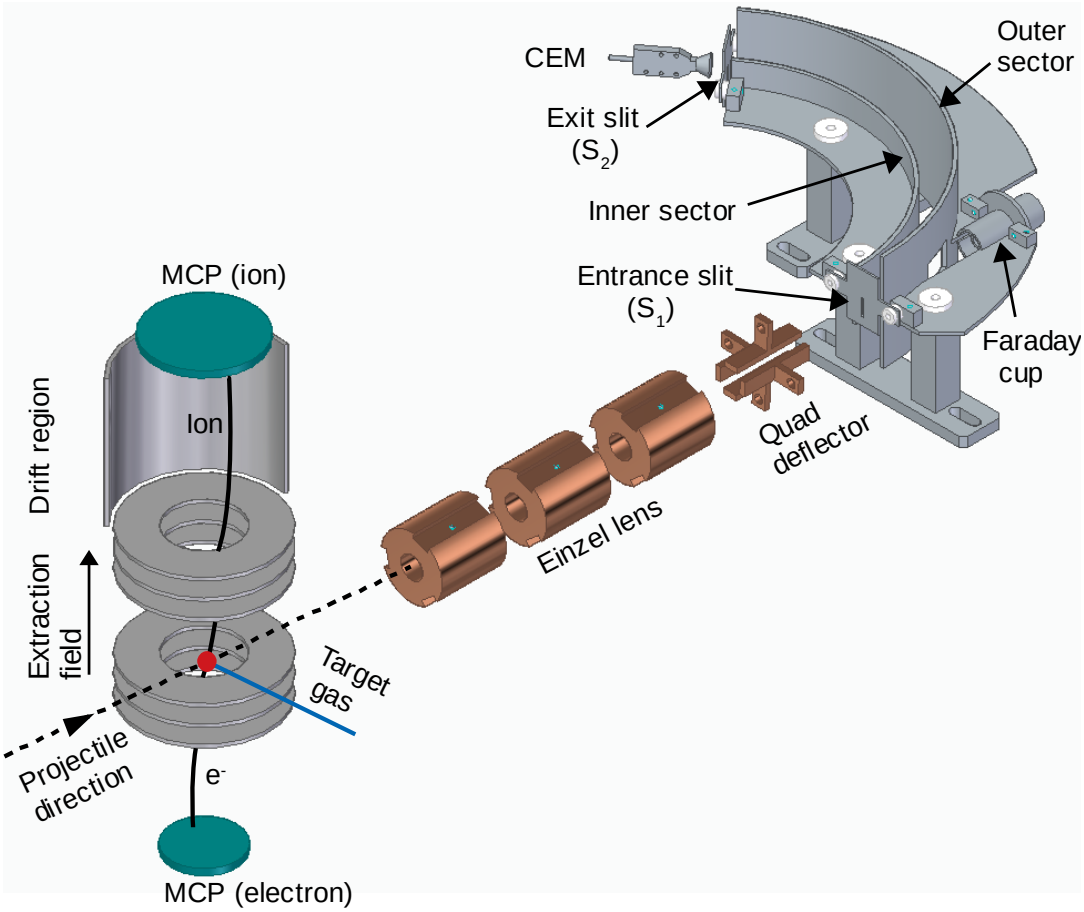


Figure 5.7: Schematic diagram of the apparatus, not drawn to scale. The momentum spectrometer (left half of the diagram) and the CDA (right half of the diagram) are housed in two separate vacuum chambers, which are not shown for simplicity. The central portion shows the beam transport optics. The circle at the intersection of the target gas jet and the projectile indicates the interaction volume.

vacuum conductance between the two chambers and results in a negligible pressure gradient across the two chambers. Complete details of the momentum spectrometer and the collision chamber were presented in chapter 2.

In order to separate the underlying ionization process, the various fragment ions are detected in coincidence with the charge analyzed post-collision projectile ion. For this, the electronics of data acquisition system is reconfigured to take time start trigger from post collision projectile ion (CDA-start).

However, it should be pointed out that the ToF ($t$) value of a given ion in case of CDA-starts would be shifted to lower value in comparison to electron-start. It is because the electron detection is almost instantaneous, but the projectile takes some

time, that is not negligible compared to the ion flight time, before it gets detected after passing through the post collision analyzer. It results in delayed time-start and thereby the observed ToF spectra in case of CDA-start will be shifted to lower values. From equation 2.13, it is evident that the derivation of the correct values of $p_x$ and $p_y$ crucially depends on accurate determination of $t$, and in case of CDA-start, the values of $p_x$ and $p_y$ would be incorrect, if the delay is not accounted for. If $t_d$ is ToF of an ion observed with CDA-start, the following equation can be used to calculate correctly the $p_x$ and $p_y$ momentum components,

$$p_x = \frac{m(x - x_0)}{t_d + \Delta t}, \; p_y = \frac{m(y - y_0)}{t_d + \Delta t} \tag{5.3}$$

where $\Delta t$ represents the difference in the apparent time of flight obtained by CDA-start and the actual flight time. The magnitude of $\Delta t$ can be obtained by comparing the peak positions of the molecular ion in the ToF spectra obtained with CDA-start and electron start whenever such peaks are observed in both spectra. Furthermore, an absolute calibration of the ToF is possible by taking the known molecular ion peak (or atomic ion) positions. Eqn. 2.13 shows that $p_z$ depends on the difference of the two $(t - t_0)$, so $p_z$ component will be unaffected by delayed time-start.

### 5.4.2 Separation of capture processes

Once the momentum components $(p_x, p_y, p_z)$ of fragment ions are determined, various informations about the dissociation of created molecular ions via different ionization processes can be investigated. In order to test the function of CDA setup, an experiment with 18 keV/$q$ $Ar^{16+}$ ion impact on $CO_2$ molecule was performed, and multiple capture processes were studied. Ion and electron detectors arrangement is unchanged from the runs in which there is no post collision analyzer (see Fig. 5.7). The extraction electric field applied in the IMS affects the projectile beam to a small extent but this effect is nearly nullified by the action of a compensation ring within the extraction assembly (details can be found in [91]). Aided by the Einzel lens and the quadrupole deflector, the outgoing projectile after the interaction with the target molecule is directed to the CDA for charge state analysis.

Ionization of the target creates multiply ionized molecular ions $CO_2^{n+}$. If the

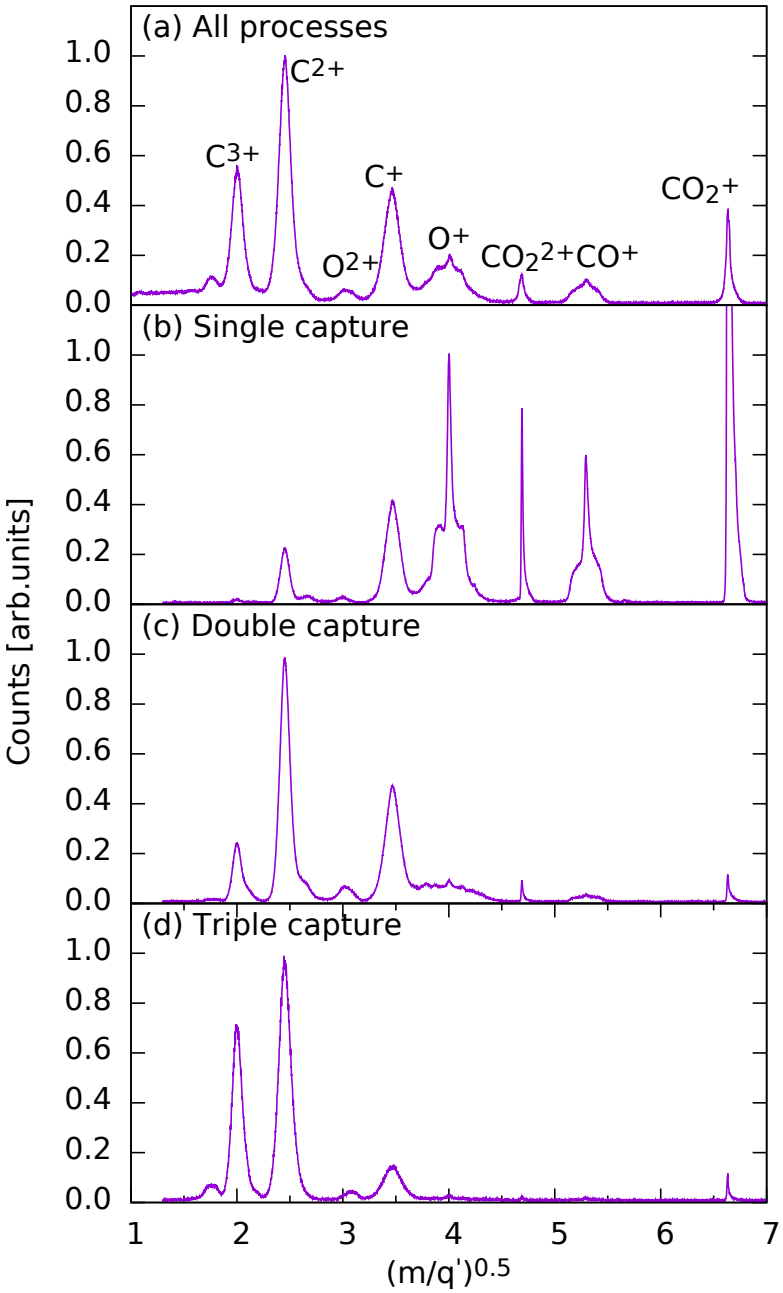


Figure 5.8: ToF mass spectra of various fragments shown on the $\sqrt{m/q'}$ scale (a) electron-start (all processes) (b) CDA start for single capture (c) CDA start for double capture, and (d) CDA start for triple capture in $Ar^{16+}$ impact on $CO_2$ at an energy of 18 keV/$q$. In each spectrum the strongest fragment peak is normalized to unity for convenience of presentation. The weak, but persistent $CO_2^+$ peak, which should not appear in coincidence with a double or triple capture projectile, appears due to capture from the background gas.

molecular ion is in an excited state, it is generally unstable and undergoes dissociation. Multiple ionization involving different capture processes would result in a change in the charge state of the projectile. As a result, the outgoing projectiles will

have a mix $E/q$ values. In order to identify the underlying ionization process, the charge change is detected by analyzing the outgoing projectile via the CDA. Here, we present a set of results pertaining to different capture processes, which have been separated using the CDA, as follows,

$$Ar^{q+} + CO_2 \rightarrow Ar^{(q-1)} + {CO_2}^{n+} + (n-1)e^- \quad (5.4)$$

$$Ar^{q+} + CO_2 \rightarrow Ar^{(q-2)} + {CO_2}^{n+} + (n-2)e^- \quad (5.5)$$

$$Ar^{q+} + CO_2 \rightarrow Ar^{(q-3)} + {CO_2}^{n+} + (n-3)e^- \quad (5.6)$$

The above equations represent multiple ionization of $CO_2$ via single capture, double capture, and triple capture, respectively. Here we present only the basic ToF spectra that amply demonstrate the difference in the collision outcomes in different ionization processes. Details of the kinematics will be presented in the next chapter. Fig. 5.8 shows the fragment mass spectra observed in different ionization processes for 18 keV/$q$ $Ar^{16+}$ projectile ion impact. To eliminate the dependence of the apparent flight time on the type of the start trigger, distributions of the fragments are shown as a function of their $\sqrt{m/q'}$ values, which is derived from the measured ToF values, where $m$ and $q'$ are the mass and charge of fragment, respectively.

Fig. 5.8 shows the distribution of fragments with the ToF-start trigger taken from the ejected electron and from the CDA signal for single capture, double capture and triple capture processes. The spectrum with electron starts reflects a mix of ionization processes, while the other three are a reflection of only one ionization process each. Several fragment ion mass peaks, resulting from the dissociation of various multiply ionized $CO_2$ molecular ion, are clearly seen, and the differences in the relative intensities of the fragments under different capture processes are evident. The appearance of small $CO_2^+$ ion peak in coincidence with the double and triple capture signal is due to capture from background gas. It can be further suppressed by reducing the pressure of the target gas jet.

For single capture process, lower charged $CO^+$, $O^+$ and $C^+$ fragment ions are the most prominent along with dominating singly charged recoil molecular ion $CO_2^+$. However, for the double capture process, the intensities of low charged fragment ions are suppressed and those of highly charged $C^{2+}$, $C^{3+}$ fragment ions is enhanced,

and finally, in the triple capture process, lower charged fragments ions have nearly disappeared. Thus, the relative probabilities of the formation of various multiply ionized molecular ions are strongly influenced by different ionization processes. A closer inspection shows that the shape of the ToF distributions of fragment ions, such as $CO^+$, $O^+$ and $O^{2+}$ is also significantly affected by different ionization processes. The $CO^+$ ion has one sharp feature at the center with two shoulder structures around it in single capture process. The central sharp peak is attributed to $CO^+$ ions with low kinetic energy. The broad shoulder corresponds to energetic $CO^+$ fragments coming from different Coulomb explosion events. It can be seen that the ratio of these two features changes in different processes. In the case of the double capture process, the central feature almost disappears. Similar effects are also observed for $O^+$ and $O^{2+}$ fragments. The change in the shape of ToF distribution indicates the involvement of different kinematics in the dissociation of molecular ions created in different processes. The effect of different capture processes on the kinematics of dissociating molecular ions will be discussed in the next chapter.

## 5.5 Summary

In this chapter, we have presented the $\phi = 127°$ cylindrical deflector analyzer (CDA), including its working principle, simulations, assembly, characterization and its implementation. The capability of CDA to separate highly charged ions of different $E/q$ values is first realized through detailed simulations using the SIMION suite of programs. Its focusing property and transmission are also discussed. Further, it has been verified experimentally by sending ion beams of different $E/q$ values through CDA. With suitable voltages applied on its cylindrical plates, the separations of ions have been achieved efficiently. In the present CDA assembly, the cylindrical sectors of equal height $h$ =60 mm has been employed. However, simulation results have shown that the cylindrical sectors of different heights, 60 mm and 30 mm, lead to an additional focusing action in a direction perpendicular to the deflection plane. Further improvement in ion transmission can be achieved, whenever needed, by merely replacing one of the sectors.

The CDA is primarily designed to investigate different ionization processes re-

sponsible for multiple ionization of targets in ion-molecule collisions. For a given collision system, the different ionization processes result in a change in energy-to-charge $E/q$ value of projectile ion. The capability of CDA to separate highly charged ions of different $E/q$ values, with nearly the same value of $E$ but different values of $q$, is utilized. To employ it experimentally, CDA assembly is added downstream of the IMS chamber, and charge changed projectiles are detected.

Experimental results of $Ar^{16+}$ projectile impact, at an energy of 18 keV/$q$, on $CO_2$ molecule have been discussed. The processes, including single, double and triple capture, that result in a change in the charge state of the projectile ion, have been separated from each other successfully by analyzing the charge state of post collision projectile ion in coincidence with formed fragment ions. The inbuilt time-of-flight (ToF) spectrometer in IMS has enabled us to identify various fragment ions observed in different processes. Considerably different fragment ion distributions have been observed corresponding to various capture processes. The relative intensities of mass peaks as well as the shapes of their ToF distributions are significantly influenced. The change in relative intensities of mass peaks reveals that the ionization of the target via different order of capture process creates various multiply ionized molecular ions with varying probabilities. Secondly, the change in the shape of ToF distributions indicates that different capture processes also influence the kinematics involved in dissociating molecular ions.

# Chapter 6

# Study of charge-exchange processes in ion-molecule collisions

## 6.1 Introduction

In chapters 3 and 4, we discussed the kinematics involved in dissociating molecular ions created under the impact of HCIs of various charge states and a simplest projectile ion, the proton. In those experiments no distinction could be made between charge-exchange (CX) and direct ionization processes. Apart from the point of view of a fundamental understanding, CX induced ionization processes are of great significance in astrophysical environments, where the collisions energies are such that CX processes dominate over direct ionization. They are considered one of the prominent reasons responsible for soft x-ray emissions from comets as they transit our solar system [66, 67]. Slow HCIs in the solar wind capture electron(s) from the gases surrounding the comets and subsequently results in x-ray emissions.

This chapter presents the results of dissociation dynamics of multiply ionized molecular ions formed via the capture induced CX processes. The aim is to investigate the effect of capture processes on the fragment ions distribution, and the kinetic energy release (KER) distribution observed in the dissociation of molecular ions. For this, the projectile ions $Ar^{10+}$ and $Ar^{12+}$, which have shown contrasting effects in the dissociation dynamics of $CO_2^{4+}$ (discussed in chapter 3) are considered.

The experimental setup used in this work is shown in Fig. 5.7. The experimental and detection schemes are the same as discussed in previous chapters. Beams of

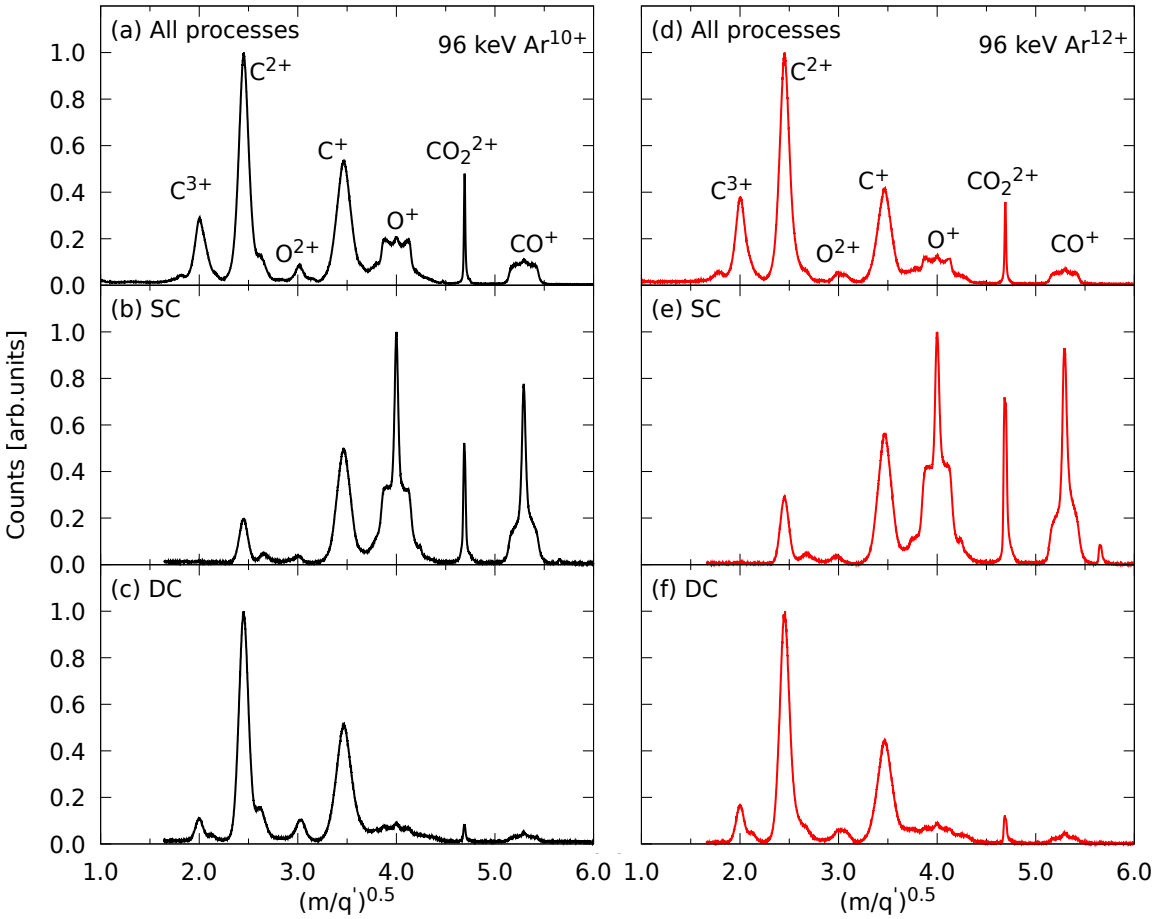


Figure 6.1: Fragment ion distributions shown on the $\sqrt{m/q'}$ scale for a mix of processes (all processes), single capture (SC) and double capture (DC) observed in impact of $Ar^{10+}$ (left panel) and $Ar^{12+}$ (right panel) on $CO_2$ at an equal energy of 96 keV. In each spectrum the strongest fragment peak is normalized to unity for convenience of presentation. The tiny peak at $m/q = 5.6$ in Fig. (e) is for $O_2^+$, arising due to air contamination.

$Ar^{10+}$ and $Ar^{12+}$ ions of equal energy, 96 keV ($v = 0.3$ a.u.), are delivered from EBIS. In order to separate the CX process, the projectile ion is made to pass through CDA after the collision with the target for charge state analysis. The dissociation dynamics of various molecular ions formed in the CX process is investigated by coincident measurement of charge analyzed projectile ion with formed fragments.

## 6.2 Fragment ion distributions

Fig. 6.1 shows the distributions of fragment ions observed in the collision of 96 keV $Ar^{10+}$ and $Ar^{12+}$ projectiles on $CO_2$ molecule via various ionization processes. The distribution of fragments is shown as a function of their $\sqrt{m/q'}$ values, where $m$

and $q'$ are the mass and charge of the fragment ion, respectively. In each spectrum, the strongest fragment peak is normalized to unity for convenience of presentation. The spectra shown in Fig. 6.1(a) and 6.1(d) are obtained in a mix of ionization processes (all processes), i.e. the ionization processes are not separated. When all processes are included, for both projectiles, $C^{2+}$ is the dominant fragment ion mass peak. For $Ar^{10+}$, the relative intensities of $C^+$, $O^+$, $CO_2^{2+}$ and $CO^+$ relative to strongest fragment peak ($C^{2+}$) are slightly higher than the relative intensities of these fragments, in comparison with the impact of $Ar^{12+}$.

Spectra Fig. 6.1(b),(e) and 6.1(c),(f) correspond to SC and DC ionization processes, respectively. For both ions, SC results in fragments of lower charge state dominantly, while for DC, higher charged fragment $C^{2+}$ dominates. In case of DC, a small peak of $C^{3+}$ also appears for both Ar-ions. Thus, for a given projectile ion, change in the order of capture process significantly influences the branching ratio of various fragments. However, across the projectiles $Ar^{10+}$ and $Ar^{12+}$, the branching ratio of fragments in SC and DC are nearly unaltered.

## 6.3 Kinetic energy release distributions

Fig. 6.2 shows the coincidence map observed under the impact of 96 keV $Ar^{12+}$ via different order of capture processes. It can be seen that for DC, the islands formed through dissociation of molecular ions of higher degree of ionization are more prominent compared to SC process. However, islands obtained due to dissociation of triply ($CO_2^{3+}$) and quadruply ionized ($CO_2^{4+}$) molecular ions appear in SC process as well. In SC process, the molecular ions of more than singly ionized state are generally formed via single capture followed by autoionization or shake-off process of the molecule.

We focus on KER distributions of three-body dissociation channels

$$CO_2^{3+} \rightarrow O^+ + C^+ + O^+ \qquad (1,1,1), \tag{6.1}$$

$$CO_2^{4+} \rightarrow O^+ + C^{2+} + O^+ \qquad (1,2,1), \tag{6.2}$$

$$CO_2^{4+} \rightarrow O^{2+} + C^+ + O^+ \qquad (2,1,1). \tag{6.3}$$

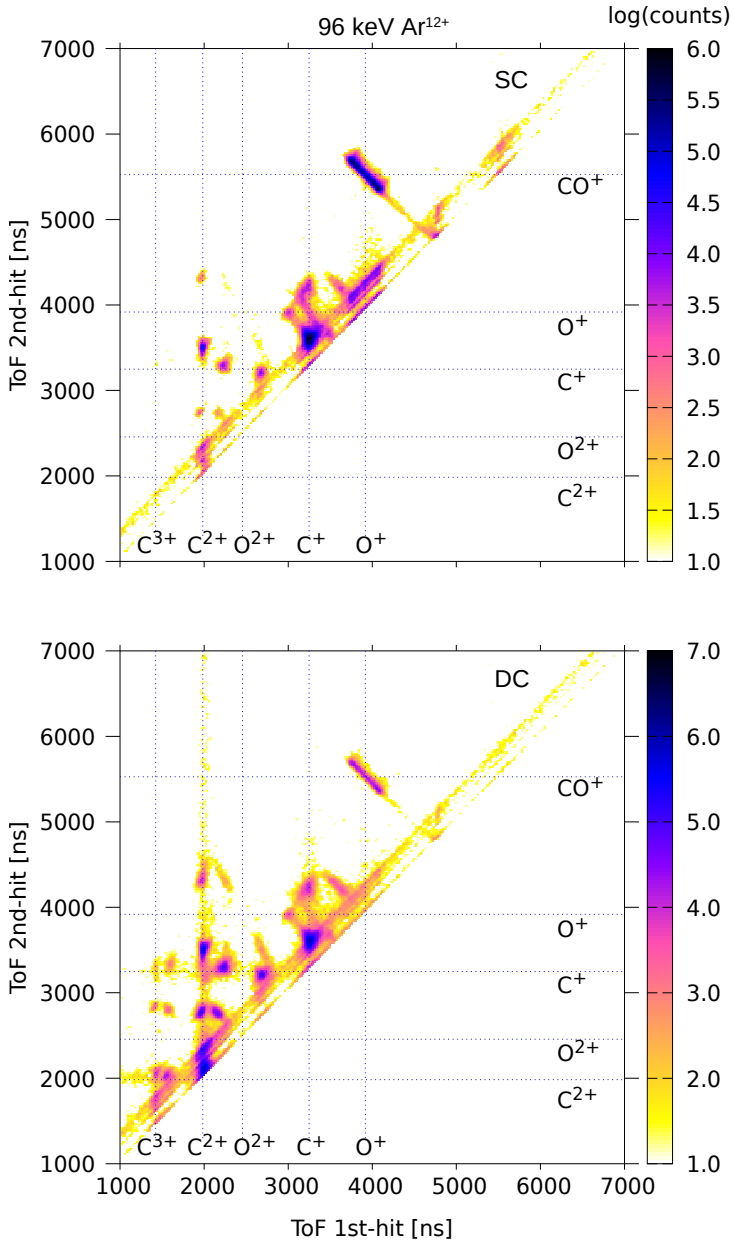


Figure 6.2: Time-of-flight coincidence map observed under the impact of 96 keV $Ar^{12+}$ ion on $CO_2$ via different order of capture processes [Top] single capture (SC) and [Bottom] double capture (DC).

formed via SC and DC processes under the impact of 96 keV, $Ar^{10+}$ and $Ar^{12+}$ ions.

### (A) Dissociation channel (1,1,1)

Fig. 6.3 shows KER distributions of dissociation channel (1,1,1) obtained via SC and DC processes induced by 96 keV, $Ar^{10+}$ and $Ar^{12+}$ impacts. For both Ar-ions, KER distributions range from 10 eV to 50 eV. There are mainly two features around 21 eV and 32 eV that can be broadly recognized in all KER distributions for both ions. It

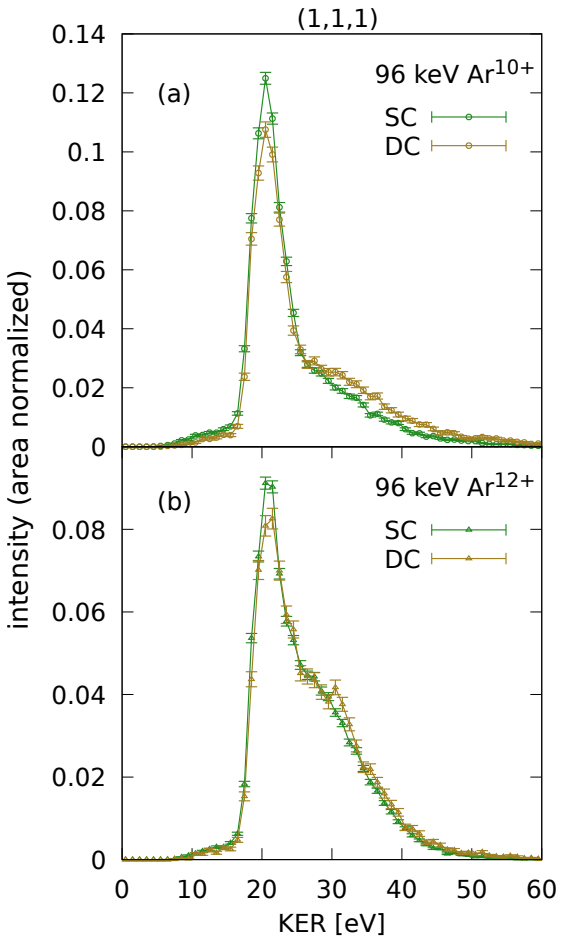


Figure 6.3: Kinetic energy release distributions of dissociation channel $O^+$:$C^+$:$O^+$ (1,1,1) resulting from collisions with projectiles (a) $Ar^{10+}$ and (b) $Ar^{12+}$ ions at the same energy of 96 keV, via single capture (SC) and double capture (DC) processes. Error bars on the experimental data show statistical errors. Areas under the curves are normalized to unity.

can be seen that for $Ar^{10+}$, KER distribution is slightly narrower. For $Ar^{12+}$, the relative intensity of the feature at 32 eV is enhanced compared to $Ar^{10+}$. However, we find that for a given projectile, different capture processes do not affect KER distribution very significantly. Nevertheless, a common contrast is visible in KER distributions of SC and DC processes for both Ar-ions. In contrast to SC, for DC process, the relative intensity of feature at higher KER 32 eV is slightly enhanced, and the feature at lower KER 21 eV is slightly suppressed for both Ar-ions.

### (B) Dissociation channels (1,2,1) and (2,1,1)

Fig. 6.4(a) and 6.4(b) show KER distributions of dissociation channel (1,2,1) obtained via SC and DC processes induced by 96 keV, $Ar^{10+}$ and $Ar^{12+}$ impacts,

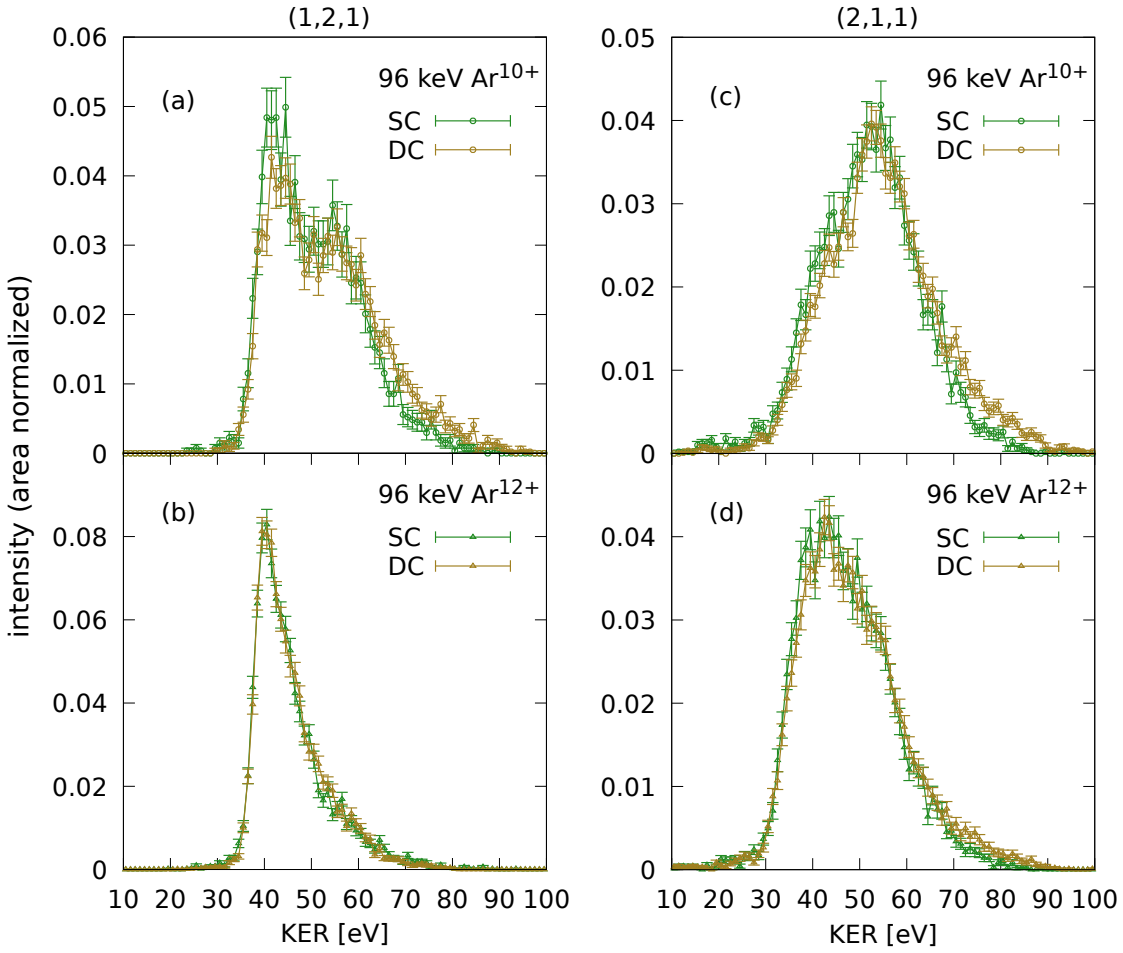


Figure 6.4: Kinetic energy release distributions of dissociation channels [Left panel] $O^+$:$C^{2+}$:$O^+$ (1,2,1) [Right panel] $O^{2+}$:$C^+$:$O^+$ (2,1,1) resulting from collisions with different projectiles $Ar^{10+}$ and $Ar^{12+}$ at an equal energy of 96 keV, via single capture (SC) and double capture (DC) processes. Error bars on the experimental data show statistical errors. Areas under the curves are normalized to unity.

respectively. KER dissociations extend from 30 eV to 80 eV and 30 eV to 70 eV for $Ar^{10+}$ and $Ar^{12+}$, respectively. For (1,2,1), there are mainly two features around 41 eV and 52 eV that can be identified in KER distributions of both projectile ions. However, for $Ar^{12+}$, KER distributions are narrower, and the feature at 52 eV is significantly suppressed. Like (1,1,1) channel, no substantial effect of capture processes on KER distributions is observed for (1,2,1) channel. However, in the case of $Ar^{10+}$, the KER is slightly broadened on the higher tail side of distribution and the feature at low KER 41 eV is slightly suppressed for the DC process. For $Ar^{12+}$, KER distributions are nearly identical for both processes.

Fig. 6.4(c) and 6.4(d) show KER distributions of dissociation channel (2,1,1) obtained via SC and DC processes induced by $Ar^{10+}$ and $Ar^{12+}$ impacts, respectively.

KER distributions range from 25 eV to 90 eV and 25 eV to 80 eV for $Ar^{10+}$ and $Ar^{12+}$, respectively. Here, there are mainly two features around 41 eV and 53 eV that can be identified in KER distributions. Similar to the earlier observations, no significant influence of capture processes on KER distributions is found. However, in the case of both Ar-ions, a slight broadening and shift in KER distributions are observed in the DC process compared to SC process.

## 6.4 Discussion

An experimental study of the effect of different capture processes on dissociation dynamics of multiply ionized molecular ions reveals that for a given slow HCI projectile, SC and DC significantly influence the relative yields of various fragment ions. We also find that SC and DC processes do not substantially affect the KER distributions of three-body dissociation channels of $CO_2^{3+}$ and $CO_2^{4+}$. Nevertheless, for a given projectile, a small but consistent contrast is noticed in KER distributions obtained in SC and DC processes. Compared to SC, DC results in a slight enhancement of high KER features and suppression of low KER features. It indicates that the ionization of the target via DC process tends to excite the comparatively higher lying electronic states of molecular ions.

The quantitative explanation of these observations requires a dedicated theoretical approach for a collision system comprising a slow, highly charged ion and molecular target. However, a plausible explanation can be given based on theoretical results for the ion-atom collision system available in the literature. A theoretical model, namely 'classical over barrier' (COB), has been adopted to explain capture processes in ion-atom collisions. According to the COB model, electron transfer from the target to the ionic projectile takes place when the potential barrier between the ionic attractive wells is so low that the Stark-shifted binding energy of electron equals the top of the barrier. This condition gives characteristic internuclear distance or effective radius at which the transfer of electron occurs. Barany *et al.* [120] and Ali *et al.* [121] have generalized COB model for many electron processes including multiple capture processes for slow ($v < 1$ a.u.) $Ar^{q+}$ (with $5 \leq q \leq 17$) ions and Ar atom collision system. This system closely resembles our collision system. It

was found that the effective radius for DC to occur is smaller than for SC process. It means that for a given projectile ion $Ar^{q+}$, DC process occurs at smaller impact parameter, resulting in comparatively strong perturbation on the target. Stronger perturbation in DC process explains the formation of higher charged fragment ions and enhanced probability to access higher lying electronic states of multiply ionized molecular ions, which causes slightly broader KER in DC process. Variations in probabilities to access various electronic states via different capture processes may also depend on the properties of potential energy curves/surfaces of a molecular ion. It is possible that SC and DC processes may excite quite a different set of excited states of some other molecular ions of $CO_2$, resulting in their more contrasting dissociation dynamics observed via two processes.

The small variation in KER distributions for different capture processes is explained for a given projectile ion based on the COB model. However, the significant differences in KER distributions of particularly $CO_2^{4+}$ dissociation channels for two different projectile ions $Ar^{10+}$ and $Ar^{12+}$ is a puzzling observation. The exact cause behind the narrower and lower side shifted KER distributions of (1,2,1) and (2,1,1) channels for $Ar^{12+}$ is still to be ascertained. The experimental observation of Ali *et al.* shows that for slow $Ar^{q+}$ and Ar atom collision system, SC is nearly four times more probable as compared to DC process for both $Ar^{10+}$ and $Ar^{12+}$ ions [121]. As the charge state of the projectile goes from $Ar^{10+}$ to $Ar^{12+}$, the rate of increment of SC cross section is greater than that of DC cross section. It indicates that the dominance of SC process in $Ar^{12+}$ impact could be a possible reason behind the contrasting observation in experimental KER distributions of $CO_2^{4+}$.

It is observed that the higher degree of ionized molecular ions such as $CO_2^{3+}$ and $CO_2^{4+}$ are formed in SC process, and for DC process, dissociation channels of even upto $CO_2^{6+}$ can be found (see coincidence map in Fig. 6.2). It means there would be some mechanisms through which the subsequent emission of electrons occurs from the target molecule in SC and DC processes forming the multiply ionized molecular ions. Such mechanisms generally include the autoionization or shake-off process of the molecule. In the current experimental setup, we do not analyze the emitted electrons in coincidence measurements; therefore, we are not able to comment on the effect of these processes, taking place along with the capture process, on the

KER distributions of dissociating molecular ions.

## 6.5 Summary

In this chapter, we have discussed the dissociation dynamics of molecular ions observed via single capture (SC) and double capture (DC) charge-exchange processes under the impact of slow ($v < 1$ a.u.) $Ar^{10+}$ and $Ar^{12+}$ ions on $CO_2$ molecule. For a given projectile, we find that different capture processes significantly influence the relative yield of various fragment ions. SC process results in the formation of lower charged fragment ions ($CO^+$, $C^+$, $O^+$), while higher charged fragment ions ($C^{2+}$, $C^{3+}$) are comparatively more prominent for DC process.

Although the fragment ion distributions are influenced significantly, SC and DC processes do not substantially affect KER distributions of $CO_2^{3+}$ and $CO_2^{4+}$ dissociation. However, for a given projectile, a small but consistent contrast is noticed in KER distributions obtained in SC and DC processes. In comparison to SC, DC results in a slight enhancement of features observed at higher KER values in KER distributions. It indicates that the ionization of the target via DC process tends to excite comparatively higher lying electronic states of molecular ions.

Plausible explanations of these observations are discussed, using COB model for ion-atom collision systems available in the literature. For a given projectile ion, DC process occurs at comparatively smaller impact parameter, which causes a stronger perturbation on target. Therefore DC tends to access higher lying excited states of the molecular ions.

In present investigation, so far, we have not been able to do cross section measurements of different capture processes for a given projectile ion. This limits us to do only relative comparison of fragment ions yields in a given capture process but not across the different capture processes.

# Chapter 7

# Summary and outlook

## 7.1 Summary of the current work

Electronic excitation can cause the multiple ionization of molecules, resulting in the formation of multiply ionized molecular ions. The so-formed multiply ionized molecular ions are generally unstable and subsequently dissociate into various fragments. During this dissociation process, the fragments move apart in a continuum, and constitute a dynamical system of a correlated many-body system. The dynamical quantities, such as the angular and kinetic energy distributions, of these fragments are governed by the participating excited states of dissociating molecular ions. By studying the kinematics of fragments, the properties of participating states of excited molecular ions can be investigated. In this thesis, we have investigated the kinematics of dissociating molecular ions into various ionic fragments created under the impacts of slow, ($v < 1$ a.u.) highly charged ions (HCIs) and the simplest projectile ion, the proton ($H^+$). The type of interactions between the projectile ion and target and ionization processes, such as direct and charge-exchange ionization, play a crucial role in deciding the exact nature of the excitation of the molecule.

The first point we have addressed is: how the projectile charge state $q$ influences the kinematics of dissociating multiply ionized molecular ion. For this, a series of experiments under the impact of $Ar^{q+}$ (with 96 keV, $8 \leq q \leq 14$) ions on $CO_2$ molecule is performed. The kinetic energy release distributions (KER) of two dissociation channels, $O^+$:$C^{2+}$:$O^+$ (1,2,1) and $O^{2+}$:$C^+$:$O^+$ (2,1,1), of $CO_2^{4+}$ molecular ion are derived for all $Ar^{q+}$. We find that the projectile charge $q$ significantly influences

the KER distributions of both dissociation channels. With the help of computed potential energy curves (PEC) of $CO_2^{4+}$, based on *ab initio* quantum chemical calculation, and experimental KER distributions, we estimate the relative probabilities of accessing various electronic states of $CO_2^{4+}$. We show that these probabilities are substantially affected by the projectile charge $q$. In particular, $Ar^{10+}$ and $Ar^{12+}$ are found to show more stark differences in excitation of $CO_2^{4+}$. Furthermore, by studying the angular distribution (Newton diagram) and normalized kinetic energy of fragments (Dalitz plot), the bond breaking mechanisms of $CO_2^{4+}$ are identified. We find that the (1,2,1) channel emanates via a concerted process in which both bonds of $CO_2^{4+}$ breaks simultaneously. On the other hand, $CO_2^{4+}$ dissociates into (2,1,1) channel dominantly via the concerted process along with a small contribution of the sequential process as well. The relative contribution of the sequential process to total events is also found to depend on the charge state of projectile $q$. It comes out to be 6% for $Ar^{12+}$ and around 3% for $Ar^{10+}$.

The second point we have addressed is: how the excitation of a dissociating molecular ion created by the simplest projectile ion, the proton ($H^+$), is different from the excitation observed under the impact of other charged projectiles such as slow HCI and electron. Under slow HCIs impact, ionization of the target occurs via capture process dominantly, and with electron impact, direct ionization is the only possibility. However, at $v < 1$ a.u. impact, the proton ionizes the target via both processes, direct and capture ionization processes. We have also looked at the effect of proton impact velocity ($v$) on dissociation dynamics of the molecular ion. For this, dissociation of $CO_2^{3+}$ into $O^+$:$C^+$:$O^+$ (1,1,1) channel under impact of $H^+$ at two impact velocities 0.5 a.u. and 0.83 a.u. is investigated. With the help of experimental KER distribution of (1,1,1) channel and PEC of $CO_2^{3+}$, we identify the participating electronic states of $CO_2^{3+}$ populated under protons impact. Putting together our proton impact results with the results of HCI and electron impact (available in the literature), we find that the simplest of projectile ion $H^+$, at a slow impact regime, populates a wide range of transient states of $CO_2^{3+}$, spanning those accessed by the impact of slow HCI and also those accessed by electron impact. We also find that despite being a structureless projectile, a small variation in the impact velocity of the proton affects the breakup dynamics in the slow impact regime. This is because

a change in the impact velocity affects the relative contribution of direct and capture ionization processes.

In these two investigations, experimental limitations did not allow us to separate different ionization processes. In order to investigate the effect of ionization processes on the excitation of molecular ions and their dissociation dynamics, we designed a post collision charge state analyzer, which is a cylindrical deflector analyzer (CDA). The CDA has charge state resolving power ($q/\Delta q$) of 17 in the energy range 5–20 keV/$q$, thereby capable of separating highly charged ions. Coupling the CDA to the ion-momentum spectrometer (IMS) enables us to separate various capture processes in ion-molecule collisions. A couple of experiments are performed with the impact of $Ar^{10+}$ and $Ar^{12+}$ ions on $CO_2$ at 0.3 a.u. velocity in which single capture (SC) and double capture (DC) processes are separated. We find that the capture processes significantly affect the relative yields of observed fragment ions. For SC, singly charged fragments are dominantly formed, while DC results in the formation of doubly and triply charged fragments. However, for a given projectile, the order of the capture processes are found to show a very small effect on the KER distributions of (1,1,1) and (1,2,1), (2,1,1) dissociation channels of $CO_2^{3+}$ and $CO_2^{4+}$, respectively. Compared to SC, KER distributions observed in DC is slightly shifter or broader on the higher side of the distribution, indicating the excitation of higher lying excited states of molecular ions in DC process. To cement such conclusions, however, requires more experimental efforts investigating several different dissociation channels.

It is found that the higher degree of ionized molecular ions such as $CO_2^{3+}$ and $CO_2^{4+}$ are observed in SC process, and for DC process, dissociation channels of even upto $CO_2^{6+}$ are observed. It indicates there exists some mechanisms through which the subsequent emission of electrons occurs from the target molecule in SC and DC processes. Such mechanisms generally include the autoionization or shake-off process of the molecule. Limitation of current experimental setup does not allow us to analyze the emitted electrons in coincidence measurements; therefore, we are not able to comment on the effect of these processes, taking place along with the capture process, on the dissociation dynamics of molecular ions.

## 7.2 Future outlook

In our first report, we have seen how the projectile charge $q$ affects the probabilities of accessing various electronic states in the experiments with slow, HCIs impact on $CO_2$. In HCIs impact, the cross sections of various capture processes also depend on the projectile velocity $v$, which can result in the excitation of molecular ions in their different electronic states. For a given projectile ion, a capture process, single or multiple, is resonantly enhanced when the velocity of projectile matches with the orbital velocity of target electron. A series of systematic experiments with projectiles of varying velocities with separation of capture processes will further increase our understanding of projectile's properties role ion-molecule collision physics.

It is understood that for a given projectile ion, direct and capture ionization occur dominantly at different impact parameters. For a given collision system, the energy deposition by projectile ion to the target depends on the impact parameter. Therefore, separating the direct ionization process unambiguously and understanding its effect on the excitation of a molecular ion and its dissociation dynamics becomes crucial in ion-molecule collisions. However, separating the direct ionization process is not very straight forward for HCIs impact. But, in singly charged ion impact, such as proton impact, separation of direct ionization is feasible in our current setup. It just requires a small change, replacing Faraday cup (mounted in downstream of ion beam, shown in Fig. 5.7) by a channel electron multiplier so that the neutralized protons can be efficiently detected.

Another important aspect that need to be explored is the effect of shell configuration of projectile ions on the excitation of created molecular ions and its dissociation dynamics. In slow HCIs impact, where ionization of the target occur via capture of electron(s) from target to the electronic shell of projectile, electronic shell configuration of projectile can play a crucial role. For example: a set of systematic experiments can be performed with the projectile ions such as $C^{q+}$, $N^{q+}$ and $O^{q+}$ of same charge state $q$, but having slightly different electronic shell configurations. In the same context, the collisions with completely striped projectile ions such as $C^{6+}$, $N^{7+}$ and $O^{8+}$, all having $1s^0$ configuration, would be intriguing to investigate their effect on dissociation dynamics. Such experiments are underway in our lab.

# Bibliography


[1] J. J. Thomson M.A. F.R.S. *The London, Edinburgh, and Dublin Philosophical Magazine and Journal of Science*, 44(269):293–316, 1897. doi: 10.1080/14786449708621070. URL https://doi.org/10.1080/14786449708621070.

[2] R. A. Millikan. *Phys. Rev.*, 2:109–143, Aug 1913. doi: 10.1103/PhysRev.2.109. URL https://link.aps.org/doi/10.1103/PhysRev.2.109.

[3] Professor E. Rutherford F.R.S. *The London, Edinburgh, and Dublin Philosophical Magazine and Journal of Science*, 21(125):669–688, 1911. doi: 10.1080/14786440508637080. URL https://doi.org/10.1080/14786440508637080.

[4] James Chadwick. *Proceedings of the Royal Society of London. Series A, Containing Papers of a Mathematical and Physical Character*, 136(830):692–708, 1932. doi: 10.1098/rspa.1932.0112. URL https://royalsocietypublishing.org/doi/abs/10.1098/rspa.1932.0112.

[5] N. Bohr Dr. phil. *The London, Edinburgh, and Dublin Philosophical Magazine and Journal of Science*, 26(151):1–25, 1913. doi: 10.1080/14786441308634955. URL https://doi.org/10.1080/14786441308634955.

[6] Max Planck. *Annalen der Physik*, 309(3):553–563, 1901. doi: https://doi.org/10.1002/andp.19013090310. URL https://onlinelibrary.wiley.com/doi/abs/10.1002/andp.19013090310.

[7] A. Einstein. *Annalen der Physik*, 322(6):132–148, 1905. doi: https://doi.org/10.1002/andp.19053220607. URL https://onlinelibrary.wiley.com/doi/abs/10.1002/andp.19053220607.

[8] E. Schrödinger. *Annalen der Physik*, 384(4):361–376, 1926. doi: https://doi.org/10.1002/andp.19263840404. URL https://onlinelibrary.wiley.com/doi/abs/10.1002/andp.19263840404.

[9] E. Schrödinger. *Annalen der Physik*, 384(6):489–527, 1926. doi: https://doi.org/10.1002/andp.19263840602. URL https://onlinelibrary.wiley.com/doi/abs/10.1002/andp.19263840602.

[10] W. Heisenberg. *Zeitschrift für Physik*, 33(1):879–893, Dec 1925. ISSN 0044-3328. doi: 10.1007/BF01328377. URL https://doi.org/10.1007/BF01328377.

[11] Egil A. Hylleraas. *Zeitschrift für Physik*, 48(7):469–494, Jul 1928. ISSN 0044-3328. doi: 10.1007/BF01340013. URL https://doi.org/10.1007/BF01340013.

[12] Egil A. Hylleraas. *Zeitschrift für Physik*, 54(5):347–366, May 1929. ISSN 0044-3328. doi: 10.1007/BF01375457. URL https://doi.org/10.1007/BF01375457.

[13] NIST data. URL https://www.nist.gov/pml/atomic-spectra-database.

[14] M. Born and R. Oppenheimer. *Annalen der Physik*, 389(20):457–484, 1927. doi: https://doi.org/10.1002/andp.19273892002. URL https://onlinelibrary.wiley.com/doi/abs/10.1002/andp.19273892002.

[15] W. Heitler and F. London. *Zeitschrift für Physik*, 44(6):455–472, Jun 1927. ISSN 0044-3328. doi: 10.1007/BF01397394. URL https://doi.org/10.1007/BF01397394.

[16] J. C. Slater. *Phys. Rev.*, 38:1109–1144, Sep 1931. doi: 10.1103/PhysRev.38.1109. URL https://link.aps.org/doi/10.1103/PhysRev.38.1109.

[17] Linus Pauling. *Journal of the American Chemical Society*, 53(9):3225–3237, 1931. URL https://pubs.acs.org/doi/pdf/10.1021/ja01360a004.

[18] Robert S. Mulliken. The assignment of quantum numbers for electrons in molecules. i. *Phys. Rev.*, 32:186–222, Aug 1928. doi: 10.1103/PhysRev.32.186. URL https://link.aps.org/doi/10.1103/PhysRev.32.186.

[19] Robert S. Mulliken. Electronic structures of polyatomic molecules and valence. ii. general considerations. *Phys. Rev.*, 41:49–71, Jul 1932. doi: 10.1103/PhysRev.41.49. URL https://link.aps.org/doi/10.1103/PhysRev.41.49.

[20] F. Hund. For the interpretation of the molecular spectra. iv. *Zeitschrift für Physik*, 51(11):759–795, Nov 1928. ISSN 0044-3328. doi: 10.1007/BF01400239. URL https://doi.org/10.1007/BF01400239.

[21] F. Hund. On the question of chemical bonding. *Zeitschrift für Physik*, 73(1): 1–30, Jan 1932. ISSN 1434-601X. doi: 10.1007/BF01337751. URL https://doi.org/10.1007/BF01337751.

[22] J. E. Lennard-Jones. The electronic structure of some diatomic molecules. *Trans. Faraday Soc.*, 25:668–686, 1929. doi: 10.1039/TF9292500668. URL http://dx.doi.org/10.1039/TF9292500668.

[23] Erich Hückel. Quantum theoretical contributions to the problem of aromatic and unsaturated compounds. iii. *Zeitschrift für Physik*, 76(9):628–648, Sep 1932. ISSN 0044-3328. doi: 10.1007/BF01341936. URL https://doi.org/10.1007/BF01341936.

[24] W. Pauli. *Zeitschrift für Physik*, 31(1):765–783, Feb 1925. ISSN 0044-3328. doi: 10.1007/BF02980631. URL https://doi.org/10.1007/BF02980631.

[25] E. Hille and T. D. Märk. *The Journal of Chemical Physics*, 69(10):4600–4605, 1978. doi: 10.1063/1.436411. URL https://doi.org/10.1063/1.436411.

[26] H. Ehrhardt, K. Jung, G. Knoth, and P. Schlemmer. *Zeitschrift für Physik D Atoms, Molecules and Clusters*, 1(1):3–32, Mar 1986. ISSN 1431-5866. doi: 10.1007/BF01384654. URL https://doi.org/10.1007/BF01384654.

[27] O J Orient and S K Strivastava. *Journal of Physics B: Atomic and Molecular Physics*, 20(15):3923, aug 1987. doi: 10.1088/0022-3700/20/15/036. URL https://dx.doi.org/10.1088/0022-3700/20/15/036.

[28] A. Lahmam-Bennani, C. Dupré, and A. Duguet. *Phys. Rev. Lett.*, 63:1582–1585, Oct 1989. doi: 10.1103/PhysRevLett.63.1582. URL https://link.aps.org/doi/10.1103/PhysRevLett.63.1582.

[29] I. Taouil, A. Lahmam-Bennani, A. Duguet, and L. Avaldi. *Phys. Rev. Lett.*, 81:4600–4603, Nov 1998. doi: 10.1103/PhysRevLett.81.4600. URL https://link.aps.org/doi/10.1103/PhysRevLett.81.4600.

[30] D. S. Milne-Brownlie, S. J. Cavanagh, Birgit Lohmann, C. Champion, P. A. Hervieux, and J. Hanssen. *Phys. Rev. A*, 69:032701, Mar 2004. doi: 10.1103/PhysRevA.69.032701. URL https://link.aps.org/doi/10.1103/PhysRevA.69.032701.

[31] E M Staicu Casagrande, A Naja, F Mezdari, A Lahmam-Bennani, P Bolognesi, B Joulakian, O Chuluunbaatar, O Al-Hagan, D H Madison, D V Fursa, and I Bray. *Journal of Physics B: Atomic, Molecular and Optical Physics*, 41 (2):025204, jan 2008. doi: 10.1088/0953-4075/41/2/025204. URL https://dx.doi.org/10.1088/0953-4075/41/2/025204.

[32] E. Krishnakumar, Vaibhav S. Prabhudesai, and Nigel J. Mason. *Nature Physics*, 14(2):149–153, Feb 2018. ISSN 1745-2481. doi: 10.1038/nphys4289. URL https://doi.org/10.1038/nphys4289.

[33] Enliang Wang, Xu Shan, Zhenjie Shen, Xingyu Li, Maomao Gong, Yaguo Tang, and Xiangjun Chen. *Phys. Rev. A*, 92:062713, Dec 2015. doi: 10.1103/PhysRevA.92.062713. URL https://link.aps.org/doi/10.1103/PhysRevA.92.062713.

[34] Zhenjie Shen, Enliang Wang, Maomao Gong, Xu Shan, and Xiangjun Chen. *The Journal of Chemical Physics*, 145(23):234303, 2016. doi: 10.1063/1.4972064. URL https://doi.org/10.1063/1.4972064.

[35] Xing Wang, Hongjing Yang, Khokon Hossen, Alexander Dorn, and Xueguang Ren. *Journal of Physics B: Atomic, Molecular and Optical Physics*, 54(7): 075201, apr 2021. doi: 10.1088/1361-6455/abef50. URL https://dx.doi.org/10.1088/1361-6455/abef50.

[36] L. J. KIEFFER and GORDON H. DUNN. *Rev. Mod. Phys.*, 38:1–35, Jan 1966. doi: 10.1103/RevModPhys.38.1. URL https://link.aps.org/doi/10.1103/RevModPhys.38.1.

[37] N Ardelyan, V Bychkov, A Belousov, and K Kosmachevskii. *Journal of Physics: Conference Series*, 927(1):012012, nov 2017. doi: 10.1088/1742-6596/927/1/012012. URL https://dx.doi.org/10.1088/1742-6596/927/1/012012.

[38] A Salin. Ionization of atomic hydrogen by proton impact. *Journal of Physics B: Atomic and Molecular Physics*, 2(6):631, jun 1969. doi: 10.1088/0022-3700/2/6/301. URL https://dx.doi.org/10.1088/0022-3700/2/6/301.

[39] L. K. Johnson, R. S. Gao, C. L. Hakes, K. A. Smith, and R. F. Stebbings. Direct and charge-transfer scattering of kev-energy $h^+$ and $he^+$ projectiles from rare-gas atoms to obtain small-angle absolute differential cross sections. *Phys. Rev. A*, 40:4920–4925, Nov 1989. doi: 10.1103/PhysRevA.40.4920. URL https://link.aps.org/doi/10.1103/PhysRevA.40.4920.

[40] I. Ben-Itzhak, K. D. Carnes, S. G. Ginther, D. T. Johnson, P. J. Norris, and O. L. Weaver. Fragmentation of $ch_4$ caused by fast-proton impact. *Phys. Rev. A*, 47:3748–3757, May 1993. doi: 10.1103/PhysRevA.47.3748. URL https://link.aps.org/doi/10.1103/PhysRevA.47.3748.

[41] Xuhai Hong, Feng Wang, Yong Wu, Bingcong Gou, and Jianguo Wang. $h^+ - h_2O$ collisions studied by time-dependent density-functional theory combined with the molecular dynamics method. *Phys. Rev. A*, 93:062706, Jun 2016. doi: 10.1103/PhysRevA.93.062706. URL https://link.aps.org/doi/10.1103/PhysRevA.93.062706.

[42] B. N. Roy, D. N. Tripathi, and D. K. Rai. Proton impact double ionization of noble gas atoms. *The Journal of Chemical Physics*, 57(9):3904–3909, 1972. doi: 10.1063/1.1678861. URL https://doi.org/10.1063/1.1678861.

[43] A. Amaya-Tapia, H. Martínez, R. Hernández-Lamoneda, and C. D. Lin. Charge transfer in $h^+$ + Ar collisions from 10 to 150 kev. *Phys. Rev. A*, 62:052718, Oct 2000. doi: 10.1103/PhysRevA.62.052718. URL https://link.aps.org/doi/10.1103/PhysRevA.62.052718.

[44] Hans Jürgen Lüdde, Marko Horbatsch, and Tom Kirchner. Electron capture and ionization cross-section calculations for proton collisions with methane

and the dna and rna nucleobases. *The European Physical Journal D*, 73(12): 249, Dec 2019. ISSN 1434-6079. doi: 10.1140/epjd/e2019-100344-2. URL https://doi.org/10.1140/epjd/e2019-100344-2.

[45] W. Wolff, H. Luna, E. C. Montenegro, and L. C. Rodrigues Junior. Multiple fragmentation mechanisms in ammonia: Collisions with protons in the intermediate velocity regime. *Phys. Rev. A*, 102:052821, Nov 2020. doi: 10.1103/PhysRevA.102.052821. URL https://link.aps.org/doi/10.1103/PhysRevA.102.052821.

[46] J. D. Garcia. Inner-shell ionizations by proton impact. *Phys. Rev. A*, 1:280–285, Feb 1970. doi: 10.1103/PhysRevA.1.280. URL https://link.aps.org/doi/10.1103/PhysRevA.1.280.

[47] Konrad Dennerl. Charge transfer reactions. *Space Science Reviews*, 157(1): 57–91, Dec 2010. ISSN 1572-9672. doi: 10.1007/s11214-010-9720-5. URL https://doi.org/10.1007/s11214-010-9720-5.

[48] V. Shevelko and J. Ullrich. Many-particle quantum dynamics in atomic and molecular fragmentation. 35:XXVIII, 515, 2003. doi: 10.1007/978-3-662-08492-2. URL https://doi.org/10.1007/978-3-662-08492-2.

[49] Igor D Kaganovich, Edward Startsev, and Ronald C Davidson. *New Journal of Physics*, 8(11):278, nov 2006. doi: 10.1088/1367-2630/8/11/278. URL https://dx.doi.org/10.1088/1367-2630/8/11/278.

[50] D. Mathur. *Physics Reports*, 225(4):193–272, 1993. ISSN 0370-1573. doi: https://doi.org/10.1016/0370-1573(93)90006-Y. URL https://www.sciencedirect.com/science/article/pii/037015739390006Y.

[51] S. S. Prasad and D. R. Furman. *Journal of Geophysical Research (1896-1977)*, 80(10):1360–1362, 1975. doi: https://doi.org/10.1029/JA080i010p01360. URL https://agupubs.onlinelibrary.wiley.com/doi/abs/10.1029/JA080i010p01360.

[52] Geerd HF Diercksen, Walter F Huebner, and Peter W Langhoff. Molecular astrophysics: state of the art and future directions. 2012.

[53] T. E. Cravens. *Science*, 296(5570):1042–1045, 2002. doi: 10.1126/science.1070001. URL https://www.science.org/doi/abs/10.1126/science.1070001.

[54] D. Schardt. Tumor therapy with high-energy carbon ion beams. *Nuclear Physics A*, 787(1):633–641, 2007. ISSN 0375-9474. doi: https://doi.org/10.1016/j.nuclphysa.2006.12.097. URL https://www.sciencedirect.com/science/article/pii/S0375947406010530. Proceedings of the Ninth International Conference on Nucleus-Nucleus Collisions.

[55] M Tarisien, L Adoui, F Frémont, D Lelièvre, L Guillaume, J-Y Chesnel, H Zhang, A Dubois, D Mathur, Sanjay Kumar, M Krishnamurthy, and A Cassimi. *Journal of Physics B: Atomic, Molecular and Optical Physics*, 33(1):L11, jan 2000. doi: 10.1088/0953-4075/33/1/102. URL https://dx.doi.org/10.1088/0953-4075/33/1/102.

[56] Yingying Wang, Xiaohua Shi, Jiaqi Zhou, Shenyue Xu, Dalong Guo, Shuncheng Yan, Xiaolong Zhu, and Xinwen Ma. *Phys. Rev. A*, 101:042706, Apr 2020. doi: 10.1103/PhysRevA.101.042706. URL https://link.aps.org/doi/10.1103/PhysRevA.101.042706.

[57] A M P Mendez, C C Montanari, and J E Miraglia. *Journal of Physics B: Atomic, Molecular and Optical Physics*, 53(17):175202, jul 2020. doi: 10.1088/1361-6455/ab9c36. URL https://dx.doi.org/10.1088/1361-6455/ab9c36.

[58] B. Siegmann, U. Werner, and H. O. Lutz. *Australian Journal of Physics*, 52 (3):545–554, 1999. doi: 10.1071/PH98089. URL https://doi.org/10.1071/PH98089.

[59] Deepak Sharma, Bhas Bapat, Pragya Bhatt, and C P Safvan. *Journal of Physics B: Atomic, Molecular and Optical Physics*, 52(11):115201, may 2019. doi: 10.1088/1361-6455/ab17ee. URL https://dx.doi.org/10.1088/1361-6455/ab17ee.

[60] H. O. Folkerts, R. Hoekstra, and R. Morgenstern. *Phys. Rev. Lett.*, 77:3339–3342, Oct 1996. doi: 10.1103/PhysRevLett.77.3339. URL https://link.aps.org/doi/10.1103/PhysRevLett.77.3339.

[61] B. Siegmann, U. Werner, R. Mann, N. M. Kabachnik, and H. O. Lutz. *Phys. Rev. A*, 62:022718, Jul 2000. doi: 10.1103/PhysRevA.62.022718. URL https://link.aps.org/doi/10.1103/PhysRevA.62.022718.

[62] B Siegmann, U Werner, H O Lutz, and R Mann. *Journal of Physics B: Atomic, Molecular and Optical Physics*, 35(17):3755–3765, aug 2002. doi: 10.1088/0953-4075/35/17/311. URL https://doi.org/10.1088%2F0953-4075%2F35%2F17%2F311.

[63] M. R. Jana, P. N. Ghosh, B. Bapat, R. K. Kushawaha, K. Saha, I. A. Prajapati, and C. P. Safvan. *Phys. Rev. A*, 84:062715, Dec 2011. doi: 10.1103/PhysRevA.84.062715. URL https://link.aps.org/doi/10.1103/PhysRevA.84.062715.

[64] M. Ehrich, B. Siegmann, U. Werner, and H. Lebius. *Radiation Physics and Chemistry*, 68(1):127–131, 2003. ISSN 0969-806X. doi: https://doi.org/10.1016/S0969-806X(03)00267-6. URL https://www.sciencedirect.com/science/article/pii/S0969806X03002676.

[65] A C F Santos, W Wolff, M M Sant'Anna, G M Sigaud, and R D DuBois. *Journal of Physics B: Atomic, Molecular and Optical Physics*, 46(7):075202, mar 2013. doi: 10.1088/0953-4075/46/7/075202. URL https://dx.doi.org/10.1088/0953-4075/46/7/075202.

[66] C. M. Lisse, K. Dennerl, J. Englhauser, M. Harden, F. E. Marshall, M. J. Mumma, R. Petre, J. P. Pye, M. J. Ricketts, J. Schmitt, J. Trümper, and R. G. West. *Science*, 274(5285):205–209, 1996. doi: 10.1126/science.274.5285.205. URL https://www.science.org/doi/abs/10.1126/science.274.5285.205.

[67] T. E. Cravens. Comet hyakutake x-ray source: Charge transfer of solar wind heavy ions. *Geophysical Research Letters*, 24(1):105–108, 1997. doi: https://doi.org/10.1029/96GL03780. URL https://agupubs.onlinelibrary.wiley.com/doi/abs/10.1029/96GL03780.

[68] J.H.D. Eland. *Molecular Physics*, 61(3):725–745, 1987. doi: 10.1080/00268978700101421. URL https://doi.org/10.1080/00268978700101421.

[69] D. A. Hagan and J. H. D. Eland. *Rapid Communications in Mass Spectrometry*, 3(6):186–189, 1989. doi: https://doi.org/10.1002/rcm.1290030606. URL https://analyticalsciencejournals.onlinelibrary.wiley.com/doi/abs/10.1002/rcm.1290030606.

[70] D. Mathur and J.H.D. Eland. *International Journal of Mass Spectrometry and Ion Processes*, 114(1):123–136, 1992. ISSN 0168-1176. doi: https://doi.org/10.1016/0168-1176(92)85026-V. URL https://www.sciencedirect.com/science/article/pii/016811769285026V.

[71] Vidhya Krishnamurthi, K. Nagesha, V. R. Marathe, and D. Mathur. *Phys. Rev. A*, 44:5460–5467, Nov 1991. doi: 10.1103/PhysRevA.44.5460. URL https://link.aps.org/doi/10.1103/PhysRevA.44.5460.

[72] U Alkemper, R Hörnig, and F von Busch. *Journal of Physics B: Atomic, Molecular and Optical Physics*, 29(1):35, jan 1996. doi: 10.1088/0953-4075/29/1/009. URL https://dx.doi.org/10.1088/0953-4075/29/1/009.

[73] C. Miron, M. Simon, N. Leclercq, D. L. Hansen, and P. Morin. *Phys. Rev. Lett.*, 81:4104–4107, Nov 1998. doi: 10.1103/PhysRevLett.81.4104. URL https://link.aps.org/doi/10.1103/PhysRevLett.81.4104.

[74] K. Saha, S.B. Banerjee, and B. Bapat. *Chemical Physics Letters*, 607:85–91, 2014. ISSN 0009-2614. doi: https://doi.org/10.1016/j.cplett.2014.05.037. URL https://www.sciencedirect.com/science/article/pii/S0009261414004126.

[75] L Adoui, M Tarisien, J Rangama, P Sobocinsky, A Cassimi, J-Y Chesnel, F Frémont, B Gervais, A Dubois, M Krishnamurthy, Sanjay Kumar, and D Mathur. *Physica Scripta*, 2001(T92):89, jan 2001. doi: 10.1238/Physica.Topical.092a00089. URL https://dx.doi.org/10.1238/Physica.Topical.092a00089.

[76] N. Neumann, D. Hant, L. Ph. H. Schmidt, J. Titze, T. Jahnke, A. Czasch, M. S. Schöffler, K. Kreidi, O. Jagutzki, H. Schmidt-Böcking, and R. Dörner. *Phys. Rev. Lett.*, 104:103201, Mar 2010. doi: 10.1103/PhysRevLett.

104.103201. URL https://link.aps.org/doi/10.1103/PhysRevLett.104.103201.

[77] Arnab Khan, Lokesh C. Tribedi, and Deepankar Misra. *Phys. Rev. A*, 92: 030701, Sep 2015. doi: 10.1103/PhysRevA.92.030701. URL https://link.aps.org/doi/10.1103/PhysRevA.92.030701.

[78] H Tezuka, K Takahashi, J Matsumoto, R Karimi, J H Sanderson, and H Shiromaru. *Journal of Physics B: Atomic, Molecular and Optical Physics*, 51(3): 035202, jan 2018. doi: 10.1088/1361-6455/aaa059. URL https://dx.doi.org/10.1088/1361-6455/aaa059.

[79] Lei Chen, Xu Shan, Xi Zhao, Xiaolong Zhu, Xiaoqing Hu, Yong Wu, Wentian Feng, Dalong Guo, Ruitian Zhang, Yong Gao, Zhongkui Huang, Jianguo Wang, Xinwen Ma, and Xiangjun Chen. *Phys. Rev. A*, 99:012710, Jan 2019. doi: 10.1103/PhysRevA.99.012710. URL https://link.aps.org/doi/10.1103/PhysRevA.99.012710.

[80] Bo Wang, Jie Han, Xiaolong Zhu, Long Wei, Baihui Ren, Yu Zhang, Wandong Yu, Shuncheng Yan, Xinwen Ma, Yaming Zou, Li Chen, and Baoren Wei. *Phys. Rev. A*, 103:042810, Apr 2021. doi: 10.1103/PhysRevA.103.042810. URL https://link.aps.org/doi/10.1103/PhysRevA.103.042810.

[81] D R Bates and A Dalgarno. *Proceedings of the Physical Society. Section A*, 65(11):919, nov 1952. doi: 10.1088/0370-1298/65/11/307. URL https://dx.doi.org/10.1088/0370-1298/65/11/307.

[82] D R Bates and G Griffing. *Proceedings of the Physical Society. Section A*, 66 (11):961, nov 1953. doi: 10.1088/0370-1298/66/11/301. URL https://dx.doi.org/10.1088/0370-1298/66/11/301.

[83] D R Bates and R J Tweed. Impact parameter treatment of h+-h collisions. *Journal of Physics B: Atomic and Molecular Physics*, 7(1):117, jan 1974. doi: 10.1088/0022-3700/7/1/020. URL https://dx.doi.org/10.1088/0022-3700/7/1/020.

[84] R. E. Olson and A. Salop. *Phys. Rev. A*, 16:531–541, Aug 1977. doi: 10.1103/PhysRevA.16.531. URL https://link.aps.org/doi/10.1103/PhysRevA.16.531.

[85] Hiroshi Ryufuku, Ken Sasaki, and Tsutomu Watanabe. *Phys. Rev. A*, 21:745–750, Mar 1980. doi: 10.1103/PhysRevA.21.745. URL https://link.aps.org/doi/10.1103/PhysRevA.21.745.

[86] J Burgdofer, R Morgenstern, and A Niehaus. *Journal of Physics B: Atomic and Molecular Physics*, 19(14):L507, jul 1986. doi: 10.1088/0022-3700/19/14/001. URL https://dx.doi.org/10.1088/0022-3700/19/14/001.

[87] B Bapat, D Sharma, and S Srivastav. *Journal of Physics: Conference Series*, 1412:152070, jan 2020. doi: 10.1088/1742-6596/1412/15/152070. URL https://doi.org/10.1088%2F1742-6596%2F1412%2F15%2F152070.

[88] M. Schmidt, G. Zschornack, U. Kentsch, and E. Ritter. *Review of Scientific Instruments*, 85(2):02B704, 2014. doi: 10.1063/1.4828723. URL https://doi.org/10.1063/1.4828723.

[89] W. C. Wiley and I. H. McLaren. *Review of Scientific Instruments*, 26(12):1150–1157, 1955. doi: 10.1063/1.1715212. URL https://doi.org/10.1063/1.1715212.

[90] Michael Guilhaus. *Journal of Mass Spectrometry*, 30(11):1519–1532, 1995. doi: https://doi.org/10.1002/jms.1190301102. URL https://analyticalsciencejournals.onlinelibrary.wiley.com/doi/abs/10.1002/jms.1190301102.

[91] V. Sharma and B. Bapat. *The European Physical Journal D - Atomic, Molecular, Optical and Plasma Physics*, 37(2):223–229, Feb 2006. ISSN 1434-6079. doi: 10.1140/epjd/e2005-00267-5. URL https://doi.org/10.1140/epjd/e2005-00267-5.

[92] A. Czasch, J. Milnes, N. Hay, W. Wicking, and O. Jagutzki. *Nuclear Instruments and Methods in Physics Research Section A: Accelerators, Spectrometers, Detectors and Associated Equipment*, 580(2):1066–1070, 2007. ISSN 0168-

9002. doi: https://doi.org/10.1016/j.nima.2007.06.063. URL https://www.sciencedirect.com/science/article/pii/S0168900207013241. Imaging 2006.

[93] I. Ali, R. Dörner, O. Jagutzki, S. Nüttgens, V. Mergel, L. Spielberger, Kh. Khayyat, T. Vogt, H. Bräuning, K. Ullmann, R. Moshammer, J. Ullrich, S. Hagmann, K.-O. Groeneveld, C.L. Cocke, and H. Schmidt-Böcking. *Nuclear Instruments and Methods in Physics Research Section B: Beam Interactions with Materials and Atoms*, 149(4):490–500, 1999. ISSN 0168-583X. doi: https://doi.org/10.1016/S0168-583X(98)00916-1. URL https://www.sciencedirect.com/science/article/pii/S0168583X98009161.

[94] RoentDek. URL http://www.roentdek.com.

[95] ROOT. URL https://root.cern.

[96] J. H. D. Eland. *Laser Chemistry*, 11:717149, Jan 1900. ISSN 0278-6273. doi: 10.1155/LC.11.259. URL https://doi.org/10.1155/LC.11.259.

[97] B Bapat and Vandana Sharma. *Journal of Physics B: Atomic, Molecular and Optical Physics*, 40(1):13–19, dec 2006. doi: 10.1088/0953-4075/40/1/002. URL https://doi.org/10.1088/0953-4075/40/1/002.

[98] Per Jensen, M. Spanner, and P.R. Bunker. *Journal of Molecular Structure*, 1212:128087, 2020. ISSN 0022-2860. doi: https://doi.org/10.1016/j.molstruc.2020.128087. URL https://www.sciencedirect.com/science/article/pii/S0022286020304129.

[99] R.H. Dalitz. *The London, Edinburgh, and Dublin Philosophical Magazine and Journal of Science*, 44(357):1068–1080, 1953. doi: 10.1080/14786441008520365. URL https://doi.org/10.1080/14786441008520365.

[100] L. Lammich, Doctoral Dissertation, University of Heidelberg, 2004.

[101] J. Simcic, D. R. Schultz, R. J. Mawhorter, I. Čadež, J. B. Greenwood, A. Chutjian, C. M. Lisse, and S. J. Smith. *Phys. Rev. A*, 81:062715, Jun 2010. doi: 10.1103/PhysRevA.81.062715. URL https://link.aps.org/doi/10.1103/PhysRevA.81.062715.

[102] Michael W. Schmidt, Kim K. Baldridge, Jerry A. Boatz, Steven T. Elbert, Mark S. Gordon, Jan H. Jensen, Shiro Koseki, Nikita Matsunaga, Kiet A. Nguyen, Shujun Su, Theresa L. Windus, Michel Dupuis, and John A. Montgomery. November 1993. doi: 10.1002/jcc.540141112. URL https://doi.org/10.1002/jcc.540141112.

[103] Péter G. Szalay, Thomas Müller, Gergely Gidofalvi, Hans Lischka, and Ron Shepard. *Chemical Reviews*, 112(1):108–181, Jan 2012. ISSN 0009-2665. doi: 10.1021/cr200137a. URL https://doi.org/10.1021/cr200137a.

[104] Th Weber, O Jagutzki, M Hattass, A Staudte, A Nauert, L Schmidt, M H Prior, A L Landers, A Bräuning-Demian, H Bräuning, C L Cocke, T Osipov, I Ali, R Díez Muiño, D Rolles, F J García de Abajo, C S Fadley, M A Van Hove, A Cassimi, H Schmidt-Böcking, and R Dörner. *Journal of Physics B: Atomic, Molecular and Optical Physics*, 34(18):3669–3678, sep 2001. doi: 10.1088/0953-4075/34/18/305. URL https://doi.org/10.1088/0953-4075/34/18/305.

[105] D. Babikov, E. A. Gislason, M. Sizun, F. Aguillon, V. Sidis, M. Barat, J. C. Brenot, J. A. Fayeton, and Y. J. Picard. *The Journal of Chemical Physics*, 116(12):4871–4876, 2002. doi: 10.1063/1.1455623. URL https://aip.scitation.org/doi/abs/10.1063/1.1455623.

[106] F. Gobet, S. Eden, B. Coupier, J. Tabet, B. Farizon, M. Farizon, M. J. Gaillard, M. Carré, S. Ouaskit, T. D. Märk, and P. Scheier. *Phys. Rev. A*, 70:062716, Dec 2004. doi: 10.1103/PhysRevA.70.062716. URL https://link.aps.org/doi/10.1103/PhysRevA.70.062716.

[107] E. Wells, Vidhya Krishnamurthi, K. D. Carnes, Nora G. Johnson, Heather D. Baxter, David Moore, Kristana M. Bloom, B. M. Barnes, H. Tawara, and I. Ben-Itzhak. *Phys. Rev. A*, 72:022726, Aug 2005. doi: 10.1103/PhysRevA.72.022726. URL https://link.aps.org/doi/10.1103/PhysRevA.72.022726.

[108] Enliang Wang, Xu Shan, Zhenjie Shen, Maomao Gong, Yaguo Tang, Yi Pan, Kai-Chung Lau, and Xiangjun Chen. *Phys. Rev. A*, 91:052711, May 2015.

doi: 10.1103/PhysRevA.91.052711. URL https://link.aps.org/doi/10.1103/PhysRevA.91.052711.

[109] Amrendra Pandey and B. Bapat. *International Journal of Mass Spectrometry*, 361:23–27, 2014. ISSN 1387-3806. doi: https://doi.org/10.1016/j.ijms.2014.01.022. URL https://www.sciencedirect.com/science/article/pii/S1387380614000360.

[110] S. W. J. Scully, J. A. Wyer, V. Senthil, M. B. Shah, and E. C. Montenegro. *Phys. Rev. A*, 73:040701, Apr 2006. doi: 10.1103/PhysRevA.73.040701. URL https://link.aps.org/doi/10.1103/PhysRevA.73.040701.

[111] V. V. Afrosimov, A. A. Basalaev, G. N. Ogurtsov, and M. N. Panov. *Technical Physics*, 59(5):642–648, May 2014. ISSN 1090-6525. doi: 10.1134/S106378421405003X. URL https://doi.org/10.1134/S106378421405003X.

[112] D. T. Young, A. G. Ghielmetti, E. G. Shelley, J. A. Marshall, J. L. Burch, and T. L. Booker. *Review of Scientific Instruments*, 58(4):501–508, 1987. doi: 10.1063/1.1139260. URL https://doi.org/10.1063/1.1139260.

[113] A. Ll. Hughes and V. Rojansky. *Phys. Rev.*, 34:284–290, Jul 1929. doi: 10.1103/PhysRev.34.284. URL https://link.aps.org/doi/10.1103/PhysRev.34.284.

[114] A. Ll. Hughes and J. H. McMillen. *Phys. Rev.*, 34:291–295, Jul 1929. doi: 10.1103/PhysRev.34.291. URL https://link.aps.org/doi/10.1103/PhysRev.34.291.

[115] D. Dube and D. Roy. *Nuclear Instruments and Methods in Physics Research*, 201(2):291–301, 1982. ISSN 0167-5087. doi: https://doi.org/10.1016/0167-5087(82)90555-5. URL https://www.sciencedirect.com/science/article/pii/0167508782905555.

[116] D. Roy and J.D. Carette. *Edited by H. Ibach, Springer*, 1977. ISSN 0342-6793. doi: https://doi.org/10.1007/978-3-642-81099-2. URL https://link.springer.com/book/10.1007/978-3-642-81099-2#bibliographic-information.

[117] SIMION. URL https://simion.com/.

[118] H. Kreckel, H. Bruhns, K. A. Miller, E. Wåhlin, A. Davis, S. Höckh, and D. W. Savin. *Review of Scientific Instruments*, 81(6):063304, 2010. doi: 10.1063/1.3433485. URL https://doi.org/10.1063/1.3433485.

[119] Solid Edge. URL https://solidedge.siemens.com/en/.

[120] A. Bárány, G. Astner, H. Cederquist, H. Danared, S. Huldt, P. Hvelplund, A. Johnson, H. Knudsen, L. Liljeby, and K.-G. Rensfelt. *Nuclear Instruments and Methods in Physics Research Section B: Beam Interactions with Materials and Atoms*, 9(4):397–399, 1985. ISSN 0168-583X. doi: https://doi.org/10.1016/0168-583X(85)90332-5. URL https://www.sciencedirect.com/science/article/pii/0168583X85903325.

[121] R. Ali, C. L. Cocke, M. L. A. Raphaelian, and M. Stockli. *Phys. Rev. A*, 49:3586–3596, May 1994. doi: 10.1103/PhysRevA.49.3586. URL https://link.aps.org/doi/10.1103/PhysRevA.49.3586.